

UNIVERSITY OF NAPLES FEDERICO II



# **Biodegradability and structure of natural fibre composites**

Libera Vitiello

**PhD in *Industrial Product and Process Engineering* (XXXV Cycle)**

Department of Chemical, Materials and Industrial Production Engineering

---

*PhD Supervisor:*  
Prof. Giovanni Filippone

*Scientific Committee:*  
Ing. Pietro Russo  
Prof.ssa Martina Salzano de Luna

*PhD Coordinator:*  
Prof. Andrea D'Anna

March 2023





# Abstract

## Biodegradability and structure of natural fibre composites

Libera Vitiello

To mitigate the plastic pollution problem, biopolymers represent one of the most interesting solutions. These “green” polymers have the inherent advantage of being produced from renewable resources and, more important, they can be biodegradable or compostable. Contrary to common perception, biodegradation of such materials in the natural environment can be a very slow process, with obvious consequences in terms of their actual environmental sustainability. In the present dissertation, the pro-degradative effects of natural fibres on a host biodegradable polymer matrix are investigated to speed up biodegradation while preserving both the eco-friendliness of materials and the excellent properties featuring plastics. For such a purpose, the degradation process and environmental footprint of hygroscopic vegetal fibre-filled hydrolysable biopolymers have been deeply studied, and the design of innovative mechanical structures has been performed.

From a chemical point of view, the biodegradation of polymer matrices is the result of the combined effect of water and microorganisms: the former induces hydrolysis of the polymer, while the latter digest the shortened chains and mineralizes the material. Natural fibres play a crucial role in this process, as they favour the access of water and microorganisms from the external environment, hence triggering the phenomenon. The best conditions to promote biodegradation are still debated. After the first part in which the optimal material-related parameters to speed up biodegradation have been investigated, the degradation process of the green composites has been assessed under different environmental conditions. The investigation thus focuses on the study of the degradation phenomena in the melt state, the hydrolytic degradation in water, and the biodegradation in compost. A cradle-to-gate life cycle assessment study of green composites has then been performed to evaluate their environmental footprint. The analysis was carried out by splitting the contributions of matrix and reinforcement to enable a conscious selection of the materials for realizing truly sustainable composites. In the end, the possibility of realizing mechanical metamaterials, i.e., systems whose mechanical properties are derived from their structure, has been investigated to obtain biodegradable materials with innovative mechanical behaviour.





# Contents

<b>1</b>	<b>Introduction</b>	<b>1</b>
1.1	Motivation	1
1.2	Thesis organization	2
<b><u>PART I</u></b>		
<b><u>Effect of natural fibres on degradation of hydrolysable polymeric matrices</u></b>		
<b>2</b>	<b>Background: the green composites and their biodegradation process</b>	<b>7</b>
2.1	What is a composite material?	7
2.2	A class of eco-friendly composites: the green composites	8
2.3	The natural fibres	10
2.4	Biodegradable polymers	11
2.5	Environmental degradability of polylactic acid (PLA)	14
2.6	Natural fibre effect on biodegradability of green composites - Literature review	16
<b>3</b>	<b>From raw materials to green composites</b>	<b>19</b>
3.1	Selection and characterization of raw materials	19
3.2	Manufacturing of the PLA-based composites filled with natural fibres	25
<b>4</b>	<b>Identification of the percolation threshold in natural fibre-based composites</b>	<b>27</b>
4.1	Relevance of the percolation threshold in green composites	27
4.2	Excluded volume percolation theory	28

4.3	Estimating $\Phi_c$ through linear viscoelastic analysis: the two-phase model	33
4.4	Estimate of $\Phi_c$ through dielectric spectroscopy	44
<b>5</b>	<b>Degradation process study of green composites</b>	<b>54</b>
5.1	Purpose and structure of the study	54
5.2	Processing effect on green composites	55
5.3	Degradation phenomena in the molten state	64
5.4	Hydrolytic degradation of PLA-based composites in water environment	69
5.5	Characterization of degradation in compost of hemp shive-based composites	82

## **PART II**

### **Life cycle assessment of green composites**

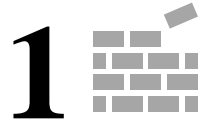
<b>6</b>	<b>Background: environmental impact analysis of green composites</b>	<b>97</b>
6.1	The concept of Life Cycle Assessment (LCA)	97
6.2	LCA of green composites	99
<b>7</b>	<b>Goal and methodology of LCA</b>	<b>101</b>
7.1	Selection of the raw materials	101
7.2	LCA methodology	103
7.3	Declared unit and system boundaries	103
7.4	Life cycle inventory and data quality	104
<b>8</b>	<b>LCA result interpretation of the PLA-based composites filled with pine needles and kenaf fibres</b>	<b>110</b>
8.1	Environmental impact of microfibers – Naturally grown vs. cultivated feedstocks	110
8.2	Environmental impact of PLA	112
8.3	Environmental impact of bio-pellets at different fibre content	114
8.4	Functionality-based LCA – Preliminary investigation of the mechanical performance of the green composites	116

## **PART III**

### **Design of biodegradable polymer-based auxetic mechanical metamaterials**

<b>9</b>	<b>Background: geometries, characteristics, and manufacturing of auxetic mechanical metamaterials</b>	<b>122</b>
9.1	What is an auxetic mechanical metamaterials?	122
9.2	General properties of negative Poisson's ratio materials	124
9.3	Additive manufacturing: the optimal manufacturing method for auxetic structures	126
<b>10</b>	<b>Design of rotating rigid structures: flat vs. curved surfaces</b>	<b>128</b>
10.1	Concept and design	128
10.2	Methodology	130
10.3	Linear FE analysis	131
10.4	Nonlinear FE analysis	135
10.5	Manufacturing of rotating rigid structures	137
10.6	Experimental validation of the theoretical results	138
	<b>Conclusions</b>	<b>141</b>
	<b>Appendix</b>	<b>145</b>
	<i>References</i>	<b>149</b>





# Introduction

## 1.1 Motivation

Although the use and consumption of plastics have significantly improved human quality of life, their massive use is having a huge environmental impact and it is now urgent to switch to sustainable alternatives. Biobased polymers are increasingly attracting the attention of industry and academia as one of the ways of reducing the dependence on petroleum-based resources. These “green” plastics have the inherent advantage of being produced from renewable resources and, more important, they can be biodegradable or compostable. The latter point is highly desirable to reduce the environmental footprint. Many plastics are biodegradable, which means that they will break down into carbon dioxide, water, and a few other elements (mineralization), but the time needed to complete the process can be very long. The challenge is shortening this time as much as possible while preserving both the environmentally friendly nature of the materials and the excellent properties featuring plastics. In the present study, this ambitious goal was pursued through a double approach: on one hand, the inherent pro-degradation ability of natural fibres was exploited; on the other hand, the potential of mechanical metamaterials was explored to generate biodegradable materials with innovative mechanical characteristics. To reach these goals, biopolymeric matrices susceptible to hydrolysis and hygroscopic vegetal fibres were combined into green composites evaluating their degradation process and environmental impact (objective 1), while innovative mechanical structures were designed, modelled, and realized by 3d-printing techniques (objective 2). Regarding the first objective, the hemicellulosic fraction of fibres acts as a water vehicle that triggers matrix hydrolysis. The shortened polymer chains can be hence mineralized by microorganisms. It is known from the literature that natural fibres promote the biodegradation of bio-polyesters or bio-polyamides. Due to the presence of many hydroxyl groups in their chemical structure, natural fibres are strongly hydrophilic, while biopolymers are generally hydrophobic. This results in a very poor interfacial adhesion that promotes access from the external environment of water and

microorganisms into the bulk of the polymeric matrix. To exploit the full potential of the pro-degradative effect of the short fibres, the formation of three-dimensional networks of fibres throughout the composite represents an important requirement. Therefore, attention was paid to the content, size, and composition of the fibres. To study biodegradation, field and laboratory tests were performed. The former mimic environmental conditions experienced in real applications; the latter are useful because of their short duration and the possibility of monitoring the progress of biodegradation. Then, the life cycle assessment (LCA) was performed to estimate the environmental footprint of green composites realized with biopolymeric matrices and hygroscopic vegetal fibres. The analysis was carried out by splitting the contributions of matrix and reinforcement to enable a conscious selection of the materials for realizing truly sustainable green composites. The second objective of the present project consists in design biodegradable materials with innovative mechanical characteristics. This goal was pursued by designing mechanical metamaterials, i.e., artificial structures with mechanical properties defined by their structure rather than their composition. The attention was placed on a specific class of mechanical metamaterials, the auxetic structures. Due to a negative Poisson's ratio, such structures undergo lateral expansion when stretched longitudinally, and become thinner when compressed. This unusual mechanical response can be exploited to expand the application field of biodegradable materials. Nevertheless, auxetic structures have complex geometries that are difficult to be manufactured. For this reason, innovative additive manufacturing technologies were adopted.

## **1.2 Thesis organization**

The present dissertation is divided into three parts, which reflect the tracks on which the research activity has been carried out. Part I encloses the soul of the work in which the study of the degradation mechanism of green composites was widely addressed. Part II and Part III complete the work by addressing two important aspects: the environmental footprint evaluation of green composites through a life cycle assessment study (Part II) and the possibility of creating biodegradable materials with innovative mechanical characteristics (Part III). Each section is basically self-consistent: in the first Chapter each part, a preliminary introduction to the central topic of the section is provided together with a brief overview of the state-of-the-art, then the results of the investigations are presented and discussed.

Part I is focused on the degradation study of PLA-based composites loaded with short natural fibres at high hemicellulose contents. A brief overview of the general understanding of the biodegradation process is provided in Chapter 2, while Chapter 3 reports information on the raw materials and production processes of the analysed systems. In the following chapters, the main results of the research activity are then described. The critical fibre concentration above which a three-dimensional network is formed inside the polymeric phase was evaluated in Chapter 4. This parameter, defined as percolation threshold ( $\Phi_c$ ), influences the biodegradation kinetics of composites filled with short natural fibres. An original rheological method for a rapid and accurate estimate of  $\Phi_c$  was proposed and validated through dielectric spectroscopy analysis. The degradation study of PLA-based composites filled with natural fibres was widely addressed in Chapter 5. First, the effects of hot working processes on the degradation of materials were evaluated to learn about the initial state of the analysed systems. Then the degradation process of the green composites was estimated under different conditions: (i) degradation phenomena in melt state, (ii) hydrolytic degradation in water, and (iii) biodegradation in compost. A cradle-to-gate life cycle assessment study of green composites made of PLA reinforced with natural fibres derived from naturally grown pine needles or cultivated kenaf feedstocks was performed in Part II. The impact of raw material production/harvesting, (ii) transportation, (iii) fibre production, (iv) melt compounding, and (v) granulation to obtain the bio-pellets was assessed. A brief overview of the basic concepts of the life cycle assessment was provided in Chapter 6. Chapter 7 reports the goal and scope identification, and the life cycle inventory compilation, while the analysis results were assessed in Chapter 8. Part III explores the possibility of realizing mechanical metamaterials, i.e., systems whose mechanical properties derived from their structure rather than from the intrinsic composition of the materials. The goal is therefore to create biodegradable materials with innovative mechanical characteristics. After the mechanical metamaterials overview reported in Chapter 9, a class of mechanical metamaterials designed by the introduction of diamond shaped perforations were investigated in Chapter 10.









**PART**

**I**

**Effect of natural fibres on  
degradation of hydrolysable  
polymeric matrices**









# **Background: the green composites and their biodegradation process**

## **2.1 What is a composite material?**

A composite material is the macroscopic combination of two or more different phases separated by a distinct interface. A judicious combination of two or more distinct materials produces a material with better properties than those of the constituent phases. Although the term composites can be applied to many different combinations of materials, it is generally used to indicate materials consisting of a continuous phase, the matrix, which holds together the dispersed phase, the reinforcement, in the form of fibres or particles [1]. According to the norm ASTM D3878, the fibres are elongated materials, with a ratio between the maximum transverse size and the minimum length of 1/10 and with the maximum transverse size less than one millimetre. The denomination of fibre is attributed to one or more filaments united in a single way [2]. On the contrary, the particles are characterized by two or three geometric axes with a similar order of magnitude [3]. Composites materials can be classified in different ways according to matrix type, fibres length, and other characteristics. A first classification is generally made according to the material used for the matrix which can be polymeric, ceramic, or metallic. For the technological and market maturity, the composite materials with a polymer matrix are the most important, while the use of metal and ceramic matrices is limited to a few applications mainly due to the high cost and complexity of the transformation technologies [4]. Both thermosetting and thermoplastic resins can be used as the polymer matrix. The former are characterized by low viscosity which makes their processability easy, while the latter are more environmentally friendly as potentially recyclable and reusable [5]. Another classification can be made considering the shape of the reinforcement and three categories can be individuated: continuous fibres composites, discontinuous fibres composites, and particle-reinforced composites. Continuous fibres composites consist of long continuous fibres that are the most efficient reinforcement as of stiffness and strength. Fibres

can be placed all parallel (unidirectional fibres), can be oriented at right angles to each other (crossply or woven fabric) or can be disposed along several directions (multidirectional fibres). Discontinuous fibres composites are reinforced by short fibres which can be oriented random or aligned. In the first case the material tends to be markedly anisotropic, whereas, in the second, it can be regarded as quasi-isotropic. Fibres can be made of different material, and they are primarily categorized as natural or synthetic fibres. Particle-reinforced composites (PRC) consist of particles randomly dispersed within the matrix and they can be generally regarded as quasi-homogeneous and quasi-isotropic materials on a macroscopic scale [3]. Compared to fibre-reinforced composites, PRCs are not high-strength materials as the particles included, mostly of ceramic, metallic or inorganic nature, can limit the deformation and, usually, guarantee only good stiffness [6]. The performances of composites materials depend on the proprieties of the single constituents, their geometry, and the distribution of the phases. Greater homogeneity or uniformity of the system means less dispersion of propriety and probability of failure in weaker areas [3]. Another important parameter is the good interfacial adhesion between matrix and reinforcement which is necessary for improving the final proprieties of the materials, such as hygrometric stability, thermal stability, and mechanical and rheological proprieties.

## **2.2 A class of eco-friendly composites: the green composites**

Composite materials reached commodity status in the 1940s with the unsaturated polyesters reinforced with glass fibres. Even today, the most common composites are made of thermosetting matrices reinforced with synthetic fibres [7]. Polymer – matrix composites have many advantages over conventional materials from the point of view of environmental sustainability. They allow the creation of strong and light products generating a low environmental impact when they are transported or used in transport applications. Polymeric composites are also very durable due to their high resistance to corrosion. This property produces a low environmental impact during production and use. Their principal disadvantage is the greater difficulty in disposing at the end-of-life of the material since their components are closely interconnected, relatively stable and difficult to separate. Therefore, reuse and recycling are quite difficult and the direct disposal in a dump or incineration is often preferred. Furthermore, their environmental impact is further worsened by the fact that the conventional polymers are produced by fossil-based resources

notoriously non-renewable [8]. However, in the last decades, research has also shown a growing interest in so-called green composites, introduced to meet the environmental concerns more and more faithfully (Figure 2.1).

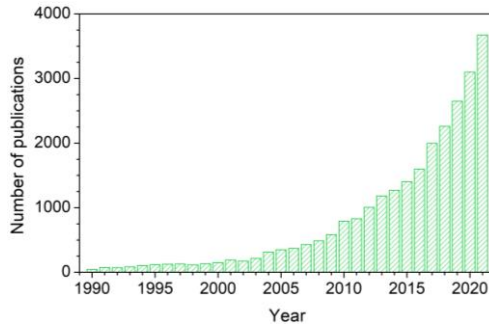


**Figure 2.1** Number of publications per year under the category "green composites" and "biocomposites" since 1990. Data from Scopus Database.

These materials are not defined by a specific norm as emerged from the literature. The most generic definition considers the green composites (often called biocomposites) as "*materials having eco-friendly attributes that are technically and economically feasible while minimizing the generation of pollution*" [9]. From here on out, the green composites that will be considered are those based on biopolymers reinforced with natural fibres. More specifically, this work will only look at the subset of biopolymers that are commonly considered as being bio-based and biodegradable (Figure 2.2).

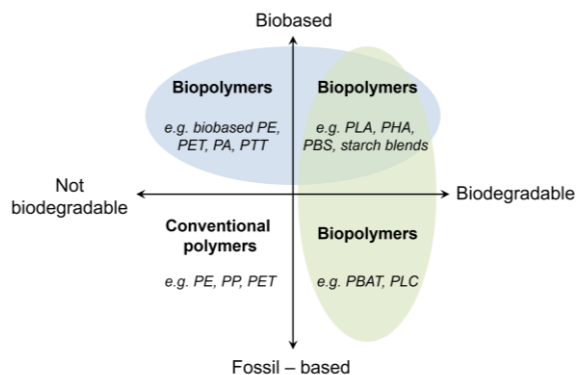


**Figure 2.2** Material classification system based on their biodegradability and bio-based content [10].

These green composites allow the realization of full biodegradable products without the use of fossil resources. Further advantages derive from the use of natural fibres characterized by lower density than conventional ones (glass, carbon, Kevlar), low cost, good mechanical properties, and intrinsic biodegradability. One of the most studied bio-based and biodegradable polymers is polylactic acid (PLA) [11]. Its good mechanical properties, easy production, and eco-compatibility make it one of the main candidates for the creation of green composites reinforced with natural fibres. Unfortunately, there are some limitations to the development and use of these materials. The considerable price and high density of biopolymers compared to traditional polymers limit their expansion on the market. Their cost can decrease only by increasing their utilization. Another important problem regards the incompatibility between natural fibres and polymer matrices. Due to the presence of many hydroxyl groups in their chemical structure, the natural fibres are strongly hydrophilic and so incompatible with the hydrophobic polymer matrices. The result is poor interface adhesion between the two phases influencing the overall properties of the product. Good adhesion can be obtained with chemical modification of fibres, but these treatments are not usable in industrial applications because usually neither convenient nor cheap [8]. Other limitations regard the use of natural fibres characterized by poor moisture resistance, low fire resistance, limited processing temperatures, and variation in quality and price [12].

## **2.3 The natural fibres**

Natural fibres are classified according to their origin which can be mineral, animal or vegetable. The firsts are generally of a length limited, except some types as the asbestos fibres whose dangerousness is known. The animal fibres are composed of proteins taken either from hair, silk, or wool and are mainly intended for the textile sector. The vegetable fibres can be obtained not only from different plants but also from different parts of the plant. In numerous applications, they are used as reinforcement for polymeric composites [13]. The major constituents of natural fibres from plants are cellulose, hemicellulose, and lignin which contain hydroxyl groups making them hydrophilic (Figure 2.3). The principal structural component of the natural fibres is the cellulose which is formed by crystalline microfibrils aligned along the length of the fibre. Cellulose is a natural semicrystalline polymer containing many hydroxyl groups (-OH). Due to the crystalline organization, the -OH groups in the amorphous part are more accessible by external moisture than those in the crystalline

regions. Hemicellulose is a polysaccharide that functions as a matrix for cellulose microfibrils. Being mostly amorphous, its hydroxyl groups are highly accessible to water molecules. The constituent that gives rigidity to the plant and assists in the transport of water is the lignin, a complex hydrocarbon polymer organized in amorphous cross-linked regions. Lignin plays a less role in moisture absorption since more hydrophobic. Other components of the natural fibres include pectin, that gives flexibility to the plant, oil and waxes, that protect the fibre [12] [14]. The structural components of the natural fibres are responsible for the properties of the material. The crystalline cellulose gives strength to the fibre; hemicellulose is the element responsible for thermal degradation, biological degradation, moisture absorption, and flammability; lignin is responsible for ultraviolet degradation and char formation [12].

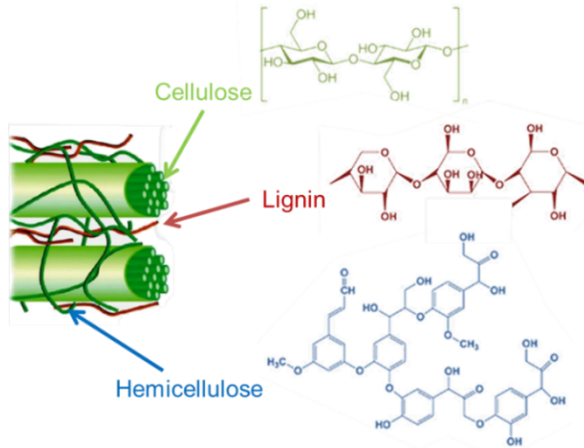


**Figure 2.3** Schematic representation of natural fibre and its components: cellulose (green), lignin (red), and hemicellulose (blue).

## 2.4 Biodegradable polymers

The International Union of Pure and Applied Chemistry (IUPAC) defines the biodegradable polymers as “*polymers susceptible to degradation by biological activity with the degradation accompanied by a lowering of its mass*” [15]. On the other hand, according to the definition given by CEN/TR 15351:2006, a biodegradable material needs to be mineralized into carbon dioxide, water, and biomass during biodegradation [16]. The biodegradation process of the polymers can be divided into four phases: biodeterioration,

depolymerization, bioassimilation, and mineralization (Figure 2.4). The biodeterioration is a superficial degradation that modifies mechanical, physical and chemical properties of a given material. In this first step, the combined action of microbial communities, decomposer organisms or/and abiotic factors fragment the biodegradable polymer into smaller particles. A polymer is a molecule with a high molecular weight, unable to cross the cell wall. Agents catalytic secreted by microorganisms and /or abiotic factors can catalyze the depolymerization of the polymer chain into oligomers, dimers, or monomers. The small molecules produced in this way are uptake into the microbial cells and primary and secondary metabolites are produced. This process is called bioassimilation. The last step is the mineralization in which the metabolites are mineralized and end products like CO<sub>2</sub>, H<sub>2</sub>O, biomass are released into the environment [17]. If oxygen is not present (anaerobic degradation) methane is also produced in this step [18].

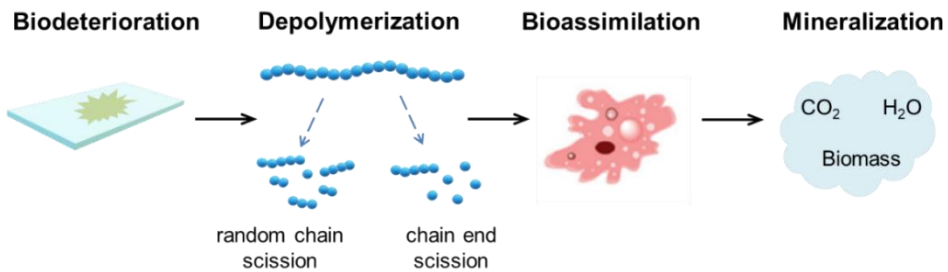


**Figure 2.4** Schematic representation of the different steps involved in biodegradation.

The biodegradation process leads to irreversible changes of the polymer until it gradually fails due to the loss of various properties. In nature, abiotic and biotic factors act synergistically to decompose organic matter [19]. Light, temperature, mechanical stress, humidity, etc. are abiotic factors, while fungi, bacteria, algae, plants, etc. are biotic factors. A polymer can undergo important transformations when exposed to weathering conditions which can change its ability to be biodegradable. According to the literature, the abiotic degradation (mechanical, light, thermal and chemical) precedes microbial assimilation for many biopolymers [20] [21]. Therefore, a study of the effect of the abiotic factors on the biodegradation process of polymers is necessary. Mechanical degradation can occur when the material is

subjected to mechanical stress which usually generates damages not visible at the macroscopic level. This factor is not predominant during biodegradation, but damages can activate it or accelerate it [22]. The polymers photosensitive can undergo transformations for the action of light radiation, one of the most important parameters in abiotic degradation. In some cases, photosensitive molecules can be added intentionally into the polymer framework to promote degradation [23]. When a thermoplastic polymer is exposed to high temperature, the long polymer chains are subject to molecular scission and the components begin to react with one another by changing the properties of the polymer. This process is called thermal degradation [24]. Generally, the environmental temperature is low, but it can influence the organization of the macromolecular framework. At glass transition temperature ( $T_g$ ) the polymer chains in the amorphous regions become flexible by facilitating the accessibility to chemical and biological degradation. Chemical transformation is the other most important parameter in abiotic degradation. The chemical reactions that take place during biodegradation can be classified into two groups: those based on oxidation and those based on hydrolysis. The decomposition of the polymers containing heteroatoms (esters, anhydrides, amides, or urethanes) occurs by hydrolysis, while the decomposition of the polymers in which the main chain contains only carbon atoms (polyolefins) occurs by oxidation which can be followed by hydrolysis of the oxidation products [17]. The hydrolysis of the materials depends on parameters as water activity, temperature, pH and time. An increase in the temperature promotes the reaction rate and a change in pH value by one unit can increase the hydrolysis rate by a factor of ten [25]. Extreme pH values are often used to prove a general (bio)degradability since the hydrolysis reactions are catalysed by the presence of hydronium and hydroxide ions, but natural highly acidic or basic conditions rarely exist. The hydrolysis can proceed through two different mechanisms: surface and bulk erosion (Figure 2.5).

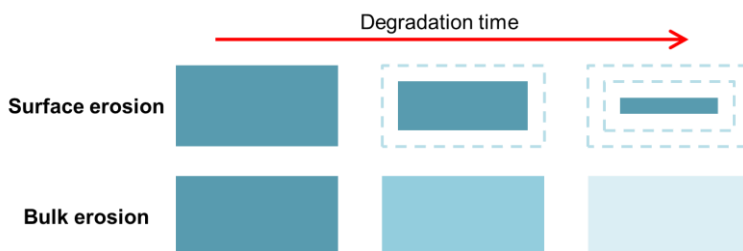


**Figure 2.5** Different mechanisms of hydrolysis: surface and bulk erosion.

Surface erosion describes a degrades from the exterior surface and occurs when the rate of hydrolysis exceeds the rate diffusion of water or when a catalyst can't penetrate the bulk polymer. Bulk erosion describes degradation that occurs uniformly throughout the whole of the sample and takes place when the rate of diffusion of water exceeds the rate of the hydrolysis reaction. Generally, the first mechanism is predominant but when the sample thickness reaches a critical value  $L_{crit}$ , the material can change from superficial to bulk erosion [26].

## 2.5 Environmental degradability of polylactic acid (PLA)

One of the most promising biodegradable polymers currently available in the market is the polylactic acid (PLA). The PLA is a bio-based aliphatic polyester derived from starch feedstock such as corn starch (in the United States), tapioca roots, chips or starch (mostly in Asia), or sugarcane (in the rest of the world). The monomer of PLA is lactic acid (LA) which is produced by bacterial fermentation of carbohydrates or by chemical synthesis. Lactic acid is the simplest carboxylic acid and exists in nature as two optically active stereoisomers, L-lactic acid, and D-lactic acid [27]. Being a biopolymer, the use of PLA could help to lower greenhouse gas emissions and reduce fossil energy consumption compared to fossil-based polymers and the municipal solid waste disposal problem. However, his production also brings pressures on land use and agriculture [28].

The environmental degradation of PLA usually involves first abiotic factors and then biotic factors. The abiotic process, in which polylactic acid is subjected to hydrolytic degradation in presence of water at high temperatures, is followed by biotic degradation, in which microorganisms decompose the break-down products, and elements like CO<sub>2</sub>, H<sub>2</sub>O, biomass are released into the environment [28]. As reported in the literature, the microorganisms can degrade PLA only after its molecular weight reaches 10000 Da or less [28]. Polylactic acid is susceptible to hydrolysis due to the hydrolysable functional groups in its backbone. In the presence of moisture, the ester groups are cleaved causing a decrease in molecular weight and the release of soluble oligomers and monomers. The products of the hydrolysis self-catalyse the reaction [29]. The hydrolysis rate of the materials depends not only on environmental factors such as humidity, temperature, and pH but also on materials proprieties. As water diffuses more readily into the less organized areas, the reaction rate is much faster in the amorphous regions compared to crystalline regions [30] [31]. The consequence is an increase in the polymer's global crystallinity during the hydrolytic reaction. Thus,

determining the crystallinity of a sample before and after degradation can also be used as a supplementary tool to assess the progress of degradation [32]. Polylactic acid can come into contact with different environments at the end-of-life. Therefore, the study of the biodegradation rate of the polymer in the different natural conditions (compost, soil, and water) is important (Figure 2.6).

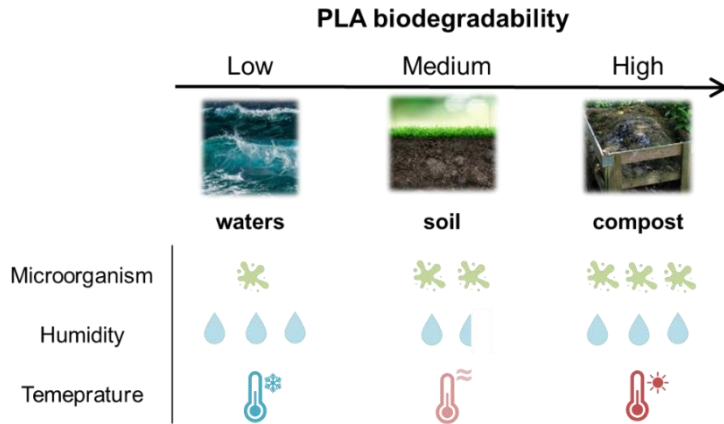


**Figure 2.6** Influence of temperature, humidity, and concentration of microorganisms on the PLA biodegradability in different natural environments.

Composting is a process where organic materials are decomposed into a humus-like substance called compost by specific microorganisms in aerobic conditions and is a versatile system for processing biodegradable solid wastes [33]. PLA can be degraded in a composting environment at 50 – 60°C by specific microorganisms after 45 – 60 days [34]. A temperature higher than room temperature is necessary to facilitate industrial composting. Above the glass transition temperature ( $T_g$ ) the chains in the amorphous regions of the polymer become flexible promoting the accessibility of chemical and biological degradation. Moreover, PLA degradation is also furthered by humidity relatively high in compost [26]. Regarding the degradation of PLA in the soil, the process is much slower than compost because the temperature and moisture content are generally lower than those found at industrial composting sites where instead PLA hydrolysis and assimilation of PLA by thermophilic microorganisms are favoured [35]. Moreover, geographical location and soil temperature may have a significant impact on degradation. A degradability of PLA very low

is instead observed in aquatic environments as marine microbes have a limited ability to degrade PLA and the temperature is generally low [28].

Composting is the optimal end-of-life option for polylactic acid since allows reducing the biodegradation times without the release of fragments in the environment. However, there are only a few existing composting facilities that accept biodegradable plastic materials since most are concerned that biodegradable plastics are not easily distinguishable from conventional plastics and that quality control is difficult [27].

## **2.6 Natural fibres effect on biodegradability of green composites – Literature review**

The timeframe that a biodegradable polymer takes to degrade is an important parameter to study the environmental impact of the end-of-life of the material. The degradation time must be such as to guarantee the correct functioning of the material during the use phase and a high rate of degradation under specific conditions. As reported in the literature, the natural fibres promote biodegradation processes of biodegradable polymers as the polylactic acid [36] [37] [38]. Therefore, the natural fibres could be considered as potential pro-degradative agents for green composites which could be employed for the aim to reduce the degradation times.

Biodegradation of a composite occurs with the degradation of its individual constituents, as well as with the loss of interfacial strength between them. Due to the presence of many hydroxyl groups in their chemical structure, the natural fibres are strongly hydrophilic, unlike the biopolymer which is generally hydrophobic. This results in a very poor interfacial adhesion that promotes the access of biological (microorganisms) or chemical (oxygen/moisture) destroying agents into the polymeric matrix [39]. Natural fibre/polymer composites are sensitive to moisture in a humid environment. The water absorbed by a green composite is typically 0.7 - 2% after 24h, 1 - 5% after week, and up to 18 - 22% after several months. This behaviour is mainly attributed to the hemicellulose, the constituent of natural fibre responsible for moisture absorption. The moisture absorption mechanism of natural fibre/polymer composite can be divided into different phases. Water penetrates and attaches to hydroxyl groups of the fibres establishing intermolecular hydrogen bonding until saturation is reached. This process generates a reduction of the interfacial adhesion. Natural fibres swell and develop stress at interface regions which generate microcracking mechanisms in the matrix around swollen fibres. This process favours

capillarity and transports water via microcracks. If water is absorbed excessively, free water in the polymers decreases and bound water increases. This second aliquot is very important as it promotes degradation in hydrolysis sensitive polymers. Water-soluble substances start leaching from fibres developing osmotic pressure pockets at the surface which cause the debonding between fibre and matrix. Therefore, the tendency of green composites to absorb moisture generates a further reduction of the interfacial adhesion fibre/matrix favouring the access of biological or chemical destroying agents (Figure 2.7) [12].

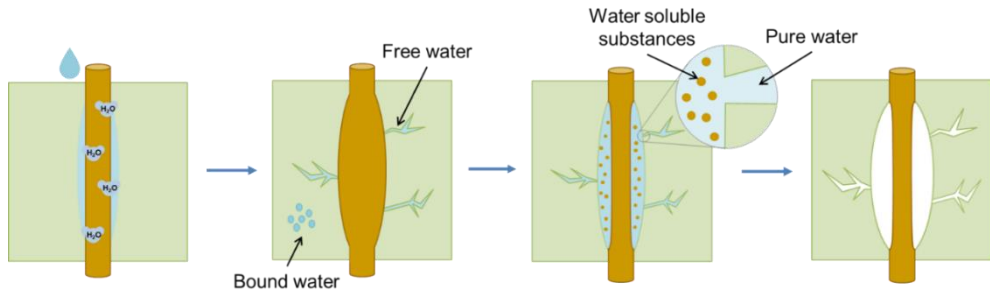


**Figure 2.7** Moisture absorption mechanism in natural fibre/polymer composites.

The biodegradation of green composites depends upon several factors such as fibre volume fraction, shape of reinforcement, temperature, area of exposed surfaces, diffusivity and reaction between water and matrix. As reported in the literature, in the case of PLA composites water absorbed by the natural fibres increases the hydrolytic reaction of the matrix near the interface with the natural fibres [36]. An important parameter is the shape of the natural fibres. The continuous fibres allow for both water and microorganisms to be easily transported through the full interior of the materials. On the contrary discontinuous fibres need to be able to form networks inside de the sample, in order for water and microorganisms from the outside to be conveyed to the interior of the materials [40]. Moreover, the increase in fibre volume fraction increases the rate of moisture absorption [41]. The area and proprieties of the exposed surface are other important parameters in the study of biodegradation as the biological contact occurs at the material - environmental interface. A rough surface with a high number of polar hydrophilic functional groups is much more prone to biodegradation than a smooth hydrophobic and inert one. Natural fibres being hydrophilic and more biodegradable, increase the adhesion of

microorganisms to the composite materials and favour biofouling. Moreover, deterioration is strongly influenced by the aspect ratio and composition of fillers. The fibres with a high length-to-diameter ratio increase biodegradation by heightening the surface area accessible to biological or chemical agents, while the presence of soluble or easy hydrolysable fractions in natural fibres enhances biodegradation, providing an easily available source of carbon for micromycetes [42].

In this work, the focus is on green composites based on polylactic acid. In the literature, the biodegradation of flax/PLA composites in compost has been addressed. The process starts with the swelling of the material after the first contact with the moist environment. The interface fibre-matrix is enlarged, cracks appear and grow due to enzymatic degradation of the natural fibre and by hydrolytic degradation of the matrix. Eventually, the material becomes brittle and begins to lose debris (Figure 2.8) [32]. As already mentioned, the simple physical disintegration/fragmentation of a polymer is not regarded as biodegradation, but the process must end with the mineralization of the material.

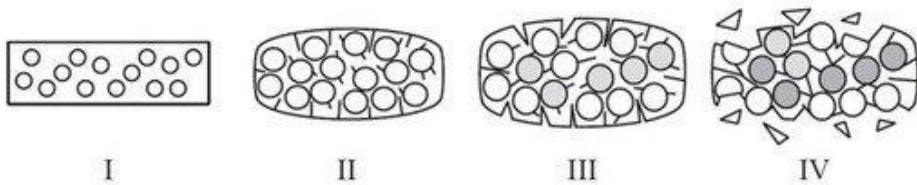


**Figure 2.8** Degradation states in PLA/natural fibres green composites [42].

# From raw materials to green composites

## 3.1 Selection and characterization of raw materials

The biodegradation study of green composites starts with the identification of a limited set of raw materials on which performing the experimental campaign necessary to draw solid and general conclusions. The selected biopolymeric matrix is the PLA, a bio-based and biodegradable polyester. The presence of hydrolysis phenomena in the first step of the PLA biodegradation process (see Chapter 2 to Section 2.5) makes it an excellent candidate to evaluate the effect of the water absorbed by the natural fibres on its degradation rate. The PLA granules were supplied by Corbion (Luminy® LX175). It has density  $\rho = 1.24 \text{ g/cm}^3$  and melt flow index MFI = 6 g/10min (at  $T = 210 \text{ }^\circ\text{C}$  with 2.16 kg weight).

Regarding the reinforcement phase, to evaluate the effect of the natural fibre type on the biodegradation process of the green composites, two different fibres are selected: hemp shives and kenaf bast. Their chemical composition is shown in Table 3.1.

**Table 3.1** - Chemical composition of selected natural fibres.

Materials	Cellulose [%]	Hemicellulose [%]	Lignin [%]	Others [%]	References
Kenaf bast	31 - 39	21.5	15 - 19	-	[43]
Hemp shives	44.3	27.2	22.0	6.2	[44]

Hemp shives (HS) and kenaf bast (KB) fibres were provided by Equilibrium Srl (Nibionno, Italy) and Kenaf Eco Fibers Italia (Guastalla, Italy) respectively. The raw materials were milled to obtain short fibres using a Retsch cutting mill (Retsch, Haan, Germany) with a grid of 0.25 mm. The density of the milled natural fibres was obtained by using a helium

pycnometer (AccuPyc II 1340, Micromeritics-Alfatest, Italy). The measurement results are reported in Table 3.2.

**Table 3.2** - Density of milled natural fibres.

Materials	Density [g/cm <sup>3</sup> ]
Kenaf bast	1.57
Hemp shives	1.51

*Natural fibres characterization*

Thermogravimetric analyses were performed on the milled natural fibres to estimate the water contents and the thermal stability using a Q500 TGA apparatus (TA Instruments). To obtain accurate and comparable water loss measurement data, the natural fibres were immersed in water at room temperature up to reaching saturated conditions. The samples were heated under nitrogen flow from room temperature up to T=110°C (heating rate of 10°C/min), then the temperature was kept constant at T=110°C for 30 minutes for monitoring the weight loss over time. The weight losses recorded by isothermal analysis are shown in Figure 3.1.

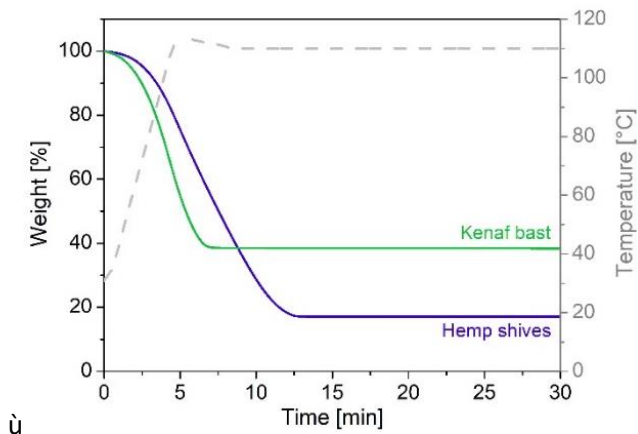


**Figure 3.1** Weight losses of the water-saturated natural fibers as collected through TGA. Dashed line shows the raise of the temperature (right axis).

The recorded mass changes can be ascribed to the loss of water not chemically bonded into the fibre and to the amount of moisture found in the fibre superficial area [45]. All samples start losing weight since the early stages of the test, when the temperature is still well below  $T=110^{\circ}\text{C}$ . After this initial drop, the weight reaches a constant value that depends on fibre water absorption capacity. Isothermal tests carried out at  $T=110^{\circ}\text{C}$  on water-saturated fibres revealed a water content of  $83.3\pm 1.5\text{ wt\%}$ , and  $63.8\pm 2.0\text{ wt\%}$ , for hemp shives, and kenaf bast fibres respectively. The difference in the water absorption capacity can be attributed to the different content of hemicellulose (Table 1) which is the element responsible for moisture absorption [12]. As mentioned in Chapter 2 Section 2.5, the biodegradation of polylactic acid starts with an abiotic process in which water and temperature trigger hydrolytic degradation. Therefore, the capacity of the natural fibre of absorbing water is an important factor in the study of the biodegradation of green composites based on PLA.

After removing the absorbed water, the samples were heated up to  $800^{\circ}\text{C}$  with a heating rate of  $10^{\circ}\text{C}/\text{min}$ . The thermogravimetry (TGA) and derivative thermogravimetry (DTG) results are shown in Figure 3.2. The major constituents of natural fibres are cellulose, hemicellulose, and lignin [46]. According to the literature, the depolymerization of hemicellulose occurs between  $180$  and  $350^{\circ}\text{C}$ , the random cleavage of the glycosidic linkage of cellulose between  $275$  and  $350^{\circ}\text{C}$ , and the degradation of lignin between  $250$  and  $500^{\circ}\text{C}$  [47]. The differences in the inherent structures and chemical nature of the cellulose, hemicellulose, and lignin possibly account for the different thermal behaviours. Cellulose, the main constituent for all the plant fibres, consists of a long polymer of glucose without any branches, its structure is order, and the thermal stability is high. Different to cellulose, hemicellulose consists of various saccharides with many branches, its structure appears random and amorphous. Therefore, hemicellulose is easy to degrade to micro-molecular volatiles at low temperatures. Lignin is full of aromatic rings with various branches. The degradation of lignin occurring in a wide temperature range because the activity of the chemical bonds in lignin covers an extremely wide range [48]. As a result of the different interactions of the three elements, the natural fibres decompose at different temperature ranges. The thermal degradation temperatures at  $5\text{wt.}\%$  loss ( $T_{5\text{wt.}\%}$ ) for hemp shives, and kenaf bast fibres are at around  $257$  and  $277^{\circ}\text{C}$  respectively (Figure 3.2a). To avoid the thermal degradation phenomenon and preserve the characteristics of the natural fibres, the process temperature of the green composite manufacturing must be less than  $T_{5\text{wt.}\%}$ . In the principal degradation step, the curves DTG show more peaks due to the

different thermal behaviour of the three major constituents of the natural fibres (Figure 3.2b). As previously said, hemicellulose decomposes before cellulose and the lignin is the most difficult to decompose. The main decomposition temperature ( $T_{peak}$ ) occurs at around 360°C, and 337°C for kenaf, and hemp respectively, and a prominent peak appears the corresponding to the maximum decomposition rate (Figure 3.2b). Table 3.3 reports the results of thermal analysis for the natural fibres under study.

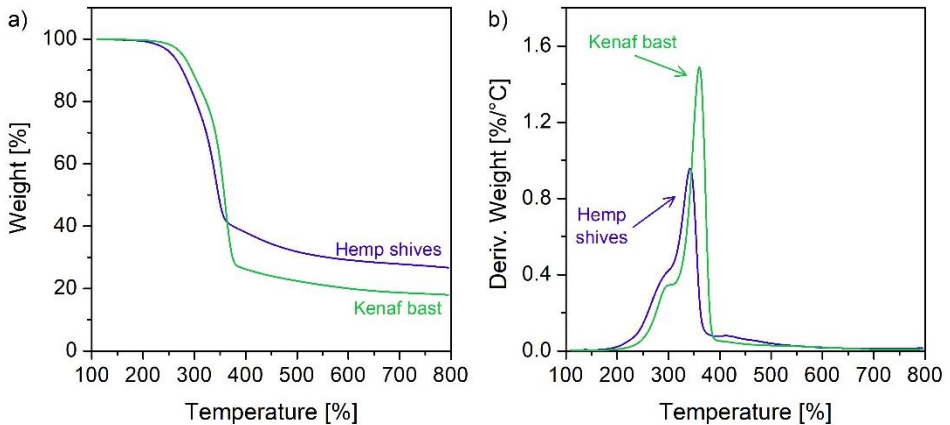


**Figure 3.2** TGA (a) and DTG (b) thermograms of milled natural fibres after the isothermal tests.

**Table 3.3** Thermal degradation temperatures at 5wt% loss,  $T_{peak}$  and residue at 800°C.

Materials	$T_{5wt. \%}$ [°C]	$T_{peak}$ [°C]	Residue at 800°C [%]
Hemp shives	257	337	16.7
Kenaf bast	277	360	8.3

The dimensional analysis of milled natural fibres has been carried out to evaluate the effect of the grinding on the raw materials. Image analysis of optical micrographs of the fibres after grinding was carried out using an Olympus BX53M microscope (Olympus Corporation, Shinjuku, Japan) to determine size and shape (aspect ratio) of the fibres. This method is often

used in literature for glass or natural fibres reinforced polymer composites and is usually based on 100–500 fibre observations [49] [50] [51] [52] [53] [54]. The number of fibres analysed is around 1000 for each system. Before the dimensional analysis, the natural fibres were dispersed in an aqueous solution of polyvinyl alcohol (PVA) to favour their deposition on glass microscope slides. Each system was subjected to approximately 1000 observations. An example of images captured for the two types of natural fibres is reported in Figure 3.3. The images show fibres of different sizes and shapes. The grinding technology and the high fragility of the raw materials caused the surface erosion of the natural fibres in addition to cutting. Therefore, two main entities can be defined: the cut fibres and the particles having a small dimension obtained from the surface erosion of the natural fibres.

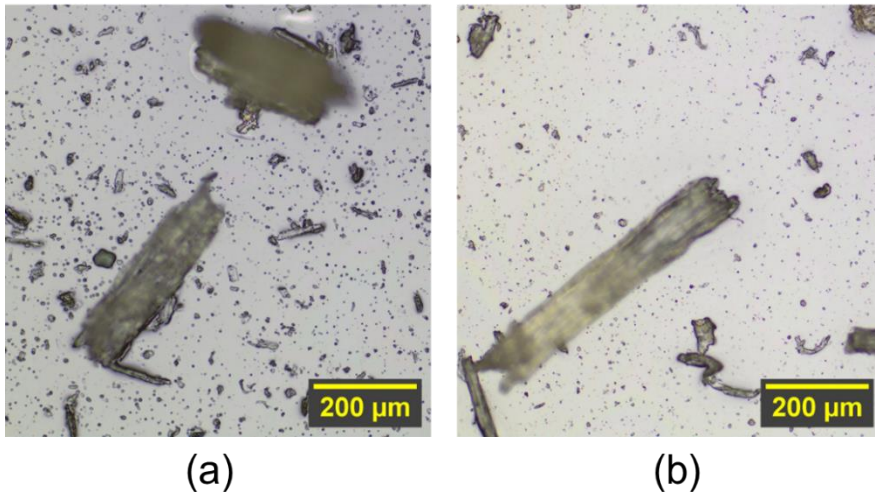


**Figure 3.3** Hemp shives (a), and kenaf bast (b) fibres optical microscope images.

Volume and number distribution of the milled natural fibres were estimated considering the fibre length ( $L$ ) as characteristic size (Figure 3.4). The number distribution represents the fibre number counted in each length range reported as a differential across the total number of counts (number frequency,  $f_N$ ). The volume distribution corresponds to the distribution per volume of the fibre length in a given interval shown as a differential of the total volume of all counts (volume frequency,  $f_V$ ). The mean and median values for the two distributions are reported in Table 3.4. The number

distribution shows a high number of fibres less than 100  $\mu\text{m}$  in length (insets, Figure 3.4). These small fibres, born as a result of surface erosion of the raw materials, are not negligible to understand the composite properties such as their rheological behaviour in the molten state. For a given volume fraction, the specific surface of small particles is larger than the one of big particles, modifying the rheology of the molten composite by increasing friction and turbulence between the polymer matrix and the particles. The volume distribution is estimated assuming the fibre shape as an equivalent cylinder. The results show that fibres with a length over 100  $\mu\text{m}$  dominate the distribution. The small fibres (i.e., lower than 100  $\mu\text{m}$ ), not occupying large volumes, have a negligible effect on the distribution. The choice of the distribution to consider depends on the properties of interest. For example, the volume distribution is relevant for the study of composite mechanical properties since the strength and elastic modulus modeling is based on fibre volume fraction. Instead, the rheology behaviour of the composite materials depends on the whole range of fibre sizes and shapes present in the polymer matrix [55].

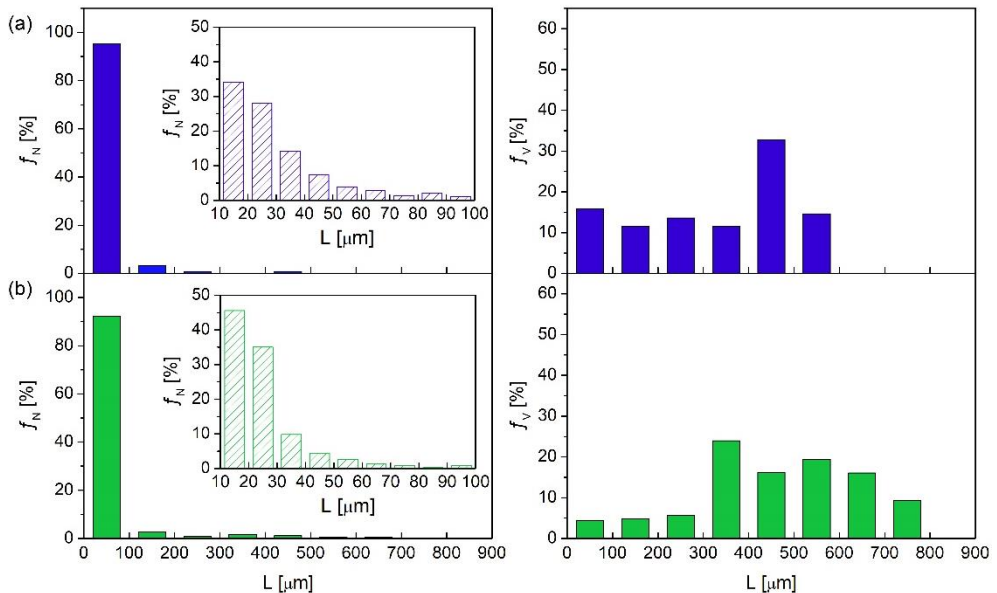


**Figure 3.4** Fibre length distribution expressed as volume ( $f_V$ ) and number ( $f_N$ ) frequency for hemp shives (a, blue), and kenaf bast (b, green) fibres. The number frequency of the fibres with a length less than 100  $\mu\text{m}$  is shown in the insets.

**Table 3.4** Mean and median of the volume and number distribution for the two types of natural fibres.

<b>Fibre content [%]</b>	<b>Mean [<math>\mu\text{m}</math>]</b>	<b>Median [<math>\mu\text{m}</math>]</b>
<i>Number distribution</i>		
Hemp shives	39	26
Kenaf bast	49	21
<i>Volume distribution</i>		
Hemp shives	376	431
Kenaf bast	461	468

### **3.2 Manufacturing of the PLA-based composites filled with natural fibres**

Two industrially feasible technologies can be used for the green compound preparation: static (batch) mixing or extrusion. Although the latter allows continuous production of large material volumes, batch mixing is exploited as it allows to overcome the technological limitations of extruders in the production of green composites at high fibre content. A Brabender Pantograph EC batch mixer (Brabender GmbH & Co. KG, Germany) operating at 180°C and 60 rpm mixing rate was used to obtain samples at volumetric fibre content from  $\Phi = 5$  vol.% to  $\Phi = 35$  vol.%. The mixing time was set to 6 minutes to allow an efficient dispersion of fibers in the matrix. Before compounding the polymer was dried overnight at 85°C under vacuum and the natural fibres were conditioned at 25°C and 80% RH. The hemp shives and kenaf bast composites were cut into granules and the panels (10 cm x 10 cm x 0.3 cm) for the subsequent characterizations were obtained by compression molding using a hydraulic press (Bench Top Hydraulic Press 20MT, Lab Tech Engineering Company LTD). The mold was pre-heated at  $T=180^\circ\text{C}$ . The molding cycle consisted of two heating phases at 180°C: the first of 5 minutes without pressure, to allow the softening of the pellets, the second of 4 minutes at a pressure of about 15 MPa, to allow the material to be compacted. The material was then cooled down to about 40°C maintaining constant pressure and the panel was removed from the mold.

The schematic representation of the molding cycle is shown in Figure 3.5.

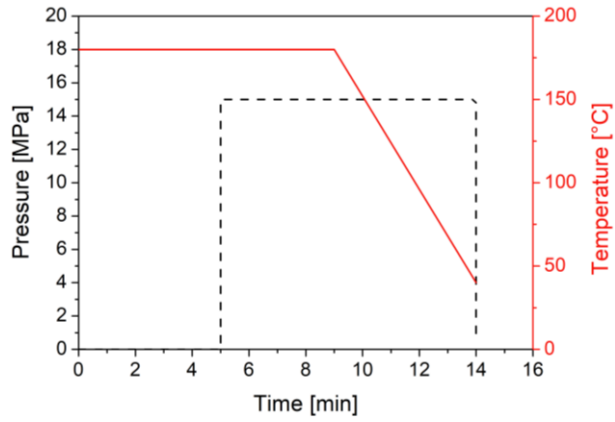


**Figure 3.5** Molding conditions of the PLA-based composites filled with natural fibres.

# Identification of the percolation threshold in natural fibre-based composites

## 4.1 Relevance of the percolation threshold in green composites

The green composites, here intended as biobased and biodegradable polymer-based composites filled with natural fibers, have gained increasing interest during the past decade due to their eco-friendly nature [56]. Their full biodegradability represents an important property to reduce the problem of plastic pollution. As reported by Azwa et al., the natural fibres affect the biodegradation process of the biodegradable polymeric matrices [12]. Due to the presence of many hydroxyl groups in their chemical structure, the natural fibres are strongly hydrophilic, unlike the biopolymer which is generally hydrophobic. This results in a very poor interfacial adhesion that promotes the access of biological (microorganisms) or chemical (oxygen/moisture) destroying agents into the polymeric matrix [57]. Several factors affect the biodegradation process of green composites such as fibre volume fraction, shape of reinforcement, temperature, area of exposed surfaces, and reaction between water and matrix. Among all, the interconnection between fibres is an important parameter in order for water and microorganisms from the outside to be conveyed to the interior of the materials [40]. When the amount of such fibres exceeds a critical percolation threshold ( $\Phi_c$ ), the solid phase forms continuous paths throughout the material and an increase in the biodegradation kinetics is expected. Therefore, the  $\Phi_c$  identification of green composites is extremely important to evaluate their biodegradation process.

The possibility of dramatic changes in the physical properties of composites due to the formation of a continuous filler network is related to the achievement of a specific percolation threshold [58] [59] [60] [61]. The direct global connection of the fillers generally results in a critical behaviour of the material transport properties (e.g., dielectric constant, electrical or thermal conductivity, and diffusion) as predicted by the percolation theory

[62]. The latter claims that, near percolation, these physical properties of composites follow a power-law relationship (4.1):

$$\text{Properties} \propto (\Phi - \Phi_c)^\beta \quad (4.1)$$

where  $\Phi$  is the filler content,  $\Phi_c$  is the so-called percolation threshold and  $\beta$  is a critical exponent that is different for various properties [63]. Therefore,  $\Phi_c$  is identified by studying the behaviour of the material properties near percolation.

The goal of this chapter is to provide the tools for the determination of the percolation threshold in natural fibre composites. Computational simulations are employed in many studies of percolation problems [64] [65] [66]. Among all, the excluded volume percolation theory which introduces the dependence of  $\Phi_c$  on the orientation and aspect ratio of the fillers is widely used [67] [68] [69]. This approach is seen as the starting point in the percolation studies by yielding a rough estimate of  $\Phi_c$  although the true value can greatly differ from it [70] [71]. To predict accurately the percolation threshold of green composites filled with randomly distributed fibres, a simple two-phase rheological model is proposed [72]. This rheological approach has been successfully applied in polymer nanocomposites containing highly flexible nanoplatelets and polymer blends filled with interfacial-located clay nanoparticles [73] [74] [75]. This method allows to estimate the network elasticity of samples at different compositions which follow a critical behaviour as predicted by percolation theory. To validate the results obtained with the proposed rheological model, the dielectric properties of water-saturated green composites at different fibre content were evaluated. The formation of a continuous network of highly hydrophobic fibres allows the access of water molecules inside the polymeric matrix causing a high increase in the dielectric constant [76] [77] [78].

## 4.2 Excluded volume percolation theory

Geometric percolation is reached when the fillers, randomly added to a matrix, result in a continuous network inside the material. The critical volume percolation threshold ( $\Phi_c$ ) can be estimated with the excluded volume percolation theory. The underlying idea is that the concentration threshold of a system is not correlated to the real volume of the object itself but to its excluded volume ( $V_{ex}$ ), i.e., the volume around an object into

which the centre of another similar object is not allowed to penetrate. Application of this concept results in percolation threshold values lower than those expected since the objects can have a true volume smaller than the excluded volume especially when they are not densely packed. Therefore, the introduction of the excluded volume concept in the percolation theory allowed the development of general empirical rules for the dependence of the percolation threshold,  $\Phi_c$ , on the object shape and orientation.

The percolation concept was introduced through a lattice model in which the sites are occupied by hard-core spheres. In this model the critical volume percolation threshold,  $\Phi_c$ , is defined as:

$$\Phi_c = \rho_c^s f \quad (4.2)$$

where  $\rho_c^s$  is the critical site-occupation probability of the lattice, and  $f$  is the filling factor of the lattice when each lattice site is occupied by a sphere [79]. This parameter is also defined as the product between the critical concentration,  $N_c$ , and the volume of each object,  $v$  [80]:

$$\Phi_c = N_c v \quad (4.3)$$

The excluded volume percolation theory correlates the critical concentration of objects with the total excluded volume ( $V_{ex}$ ) through the excluded volume of the single object ( $V$ ):

$$V_{ex} = N_c V \quad (4.4)$$

Therefore, substituting (4.4) in (4.3), the critical volume percolation threshold assumed the following expression:

$$\Phi_c = \frac{V_{ex}}{V} v \quad (4.5)$$

The short fibre composites can be assimilated to "capped cylinder" systems with a random orientation in the space. The excluded volume of a stretched object is different compared to the object's real shape and depends on the relative orientations of elements [67].

Considering a statistical distribution of the fibre orientation, only an average excluded volume  $\langle V \rangle$  can be defined such that the total excluded volume  $\langle V_{ex} \rangle$  is given by:

$$\langle V_{ex} \rangle = N_c \langle V \rangle \quad (4.6)$$

$\langle V_{ex} \rangle$  represents the total excluded volume averaged over the orientations distribution characterizing the system objects. The latter, for each type of object, assumes a constant value within a range of values in which the extremals correspond to the system characterized by a random orientation (lower limit) and a system of strictly parallel objects (upper limit). The  $\langle V_{ex} \rangle$  values, given by the literature, are reported in Table 4.1 [81].

**Table 4.1** The  $\langle V_{ex} \rangle$  values for 3D systems of equal size objects.

System	$\langle V_{ex} \rangle$
Parallel objects	2.8
Perpendicular objects	0.7
Capped – cylinders randomly aligned	1.4

For a "capped cylinder" system, the  $\langle V \rangle$  and  $v$  are defined by the following expressions [67]:

$$\langle V \rangle = \frac{4\pi}{3} D^3 + 2\pi D^2 L + D L^2 \frac{\pi}{2} \quad (4.7)$$

$$v = \frac{4\pi}{3} \left(\frac{D}{2}\right)^3 + \pi \left(\frac{D}{2}\right)^2 L \quad (4.8)$$

where  $D$  and  $L$  are the diameter and the length of the object, respectively. Therefore, the critical volume percolation threshold for a short fibre composite as a function of the aspect ratio,  $AR$ , assumed the following expression:

$$\Phi_c(AR) = \frac{\langle V_{ex} \rangle}{\frac{4\pi}{3} + 2\pi(AR) + \frac{\pi}{2}(AR)^2} \left( \frac{\pi}{6} + \frac{\pi}{4}(AR) \right) \quad (4.9)$$

Figure 4.1 reports the relationship between the critical volume percolation threshold and the fibre aspect ratio for 3D systems of equal size objects: parallel objects ( $\langle V_{ex} \rangle = 2.8$ ), randomly aligned capped cylinders ( $\langle V_{ex} \rangle = 1.4$ ), and perpendicular objects ( $\langle V_{ex} \rangle = 0.7$ ). The critical volume percolation threshold shows a decreasing trend with increasing AR and a strong dependence on the relative orientations of objects. In detail, the aspect ratio dependence of the  $\Phi_c$  shows a logarithmically linear dependence at high aspect ratios (greater than 30) which tends to increase nonlinearly with decreasing aspect ratios. The reason for this trend is that the influence of fibre ends on the percolation threshold becomes significant with decreasing fibre length [68]. Regarding the fibre orientation, the critical volume percolation threshold increase changing from perpendicular to parallel objects. The intersection probability between two fibres becomes lower for parallel objects, affecting the percolation threshold of the composite systems.

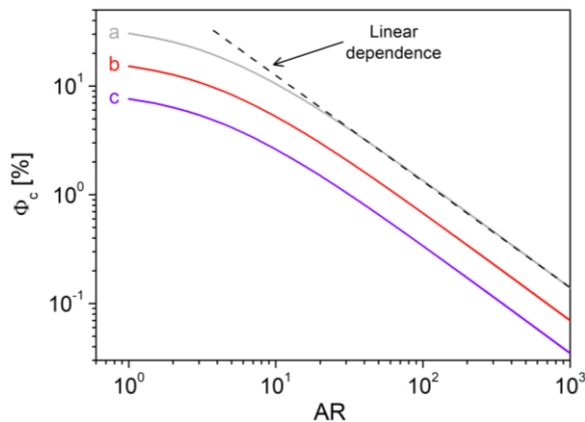


**Figure 4.1** Theoretical dependence of percolation threshold ( $\Phi_c$ ) on the aspect ratio (AR) according to the excluded volume percolation theory. The  $\Phi_c$  variation is reported for 3D systems of equal size objects: parallel objects (a), randomly aligned capped cylinders (b), and perpendicular objects (c).

Using Equation 4.9 for an estimate of  $\Phi_c$  presumes the knowledge of the orientation of the fibers, which reflects the complex flows experienced during processing and, hence, is difficult to predict. As far as the analyzed systems are concerned, the chaotic flow imparted during the melt compounding in the internal mixer suggests the picture of random orientation. However, some fiber orientation may have occurred during the

compression molding step of specimen preparation. The shear rate experienced while compressing the sample is maximum in the proximity of the surfaces of the press plates, and this could cause rotation and some alignment of the fibers parallel to the specimen surfaces. Such an orientation, if any, should concern a surface layer of our samples, which are thick enough to assume that their core maintains the random orientation of the fibers imparted by the internal mixer. A similar picture was conjectured based on experimental studies and Monte Carlo simulations in injection-molded short-fiber composites [82]. Because of the complexity of the matter, assumptions about fiber orientation were not made.

To estimate the percolation threshold of the studied systems, the aspect ratio distributions of the milled natural fibres have been estimated (Figure 4.2). The kenaf exhibits a wider distribution, which is likely due to the high thinness and flexibility of the initial fibers. The average AR values are  $3.3 \pm 1.9$  and  $4.7 \pm 2.7$  for the hemp and kenaf fibers, respectively.

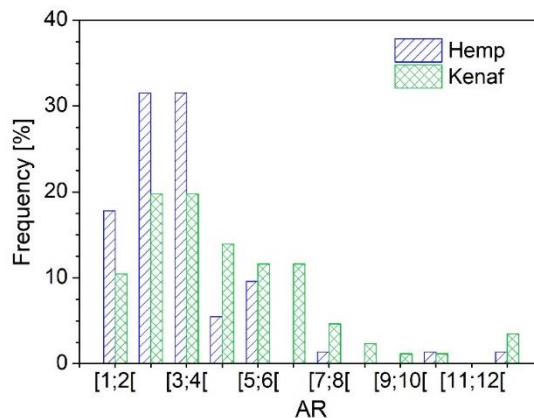


**Figure 4.2** Distributions of aspect ratio (length over diameter) of the fibers.

Substituting into Equation 4.9 leads to the theoretical values of  $\Phi_c$  summarized in Table 4.2. The ranges of possible  $\Phi_c$  are wide. Further uncertainty derives from the wideness of the AR distributions. It is clear that, unless finely controlling the compounding process and dealing with highly uniform fibres, theoretical calculations only provide large intervals of possible  $\Phi_c$  in real composites. This makes it necessary to rely on experimental methods able to reveal the existence of percolating fibre networks without the need for assumptions about the morphology and space

arrangement of the fibres. In this sense, rheology and dielectric spectroscopy represent powerful tools.

**Table 4.2** Ranges of  $\Phi_c$  computed using Equation 4.9 for the composites under investigation.

$\langle V_{ex} \rangle$ (fiber orientation)	$\Phi_c$ [vol.%]	
	<i>Hemp shives</i>	<i>Kenaf bast</i>
0.7 (perpendicular)	5.2 (4.1÷7.1)	4.2 (3.2÷6.4)
1.4 (random)	9.9 (8.1÷14.1)	8.3 (6.5÷12.7)
2.8 (parallel)	18.7 (16.3÷28.3)	15.8 (13.0÷25.5)

### 4.3 Estimating $\Phi_c$ through linear viscoelastic analysis: the two-phase model

The percolation threshold of composites loaded with randomly distributed natural fibres was estimated experimentally through a simple two-phase rheological model [72]. This method allows to evaluate the fibre network elasticity which follows a critical behaviour above  $\Phi_c$  as predicted by the percolation theory. This rheological approach has been successfully applied in polymer nanocomposites containing highly flexible nanoplatelets and polymer blends filled with interfacial-located clay nanoparticles [73] [74] [75]. The numerous analogies in the rheological behaviour between polymer nanocomposites and natural fibre-based composites have allowed the extension of the two-phase model to this new material class. The independent rheological responses of the polymer and the filler network represent the underlying physics of the model. In detail, for times longer than the polymer relaxation time, the only contribution to the elastic modulus comes from the filler network. The proposed model allows to identify the shift factors necessary to build a master curve of the elastic moduli which reflects the relaxation spectrum of the filler network alone.

#### *Linear viscoelasticity*

A stress-controlled rotational rheometer (mod. AR-G2 by TA Instruments) in parallel plate geometry (plate diameter 25mm) was used to carry out the rheological measurements. Oscillatory shear experiments were

performed at  $T=180^{\circ}\text{C}$  from frequency  $\omega=600$  rad/s down to  $\omega=0.06$  rad/s in a nitrogen atmosphere on samples previously dried at  $T=85^{\circ}\text{C}$  overnight under vacuum. The elastic ( $G'$ ) and viscous ( $G''$ ) shear moduli were recorded at strain amplitude low enough to be in the linear regime, whose limits were assessed through preliminary strain amplitude shear tests.

The occurrence of degradation phenomena of the PLA matrix in presence of natural fibres makes it challenging to obtain the relaxation spectrum of the composite materials [83]. As an example, in Figure 4.3 the elastic and viscous moduli of the composite at 10 vol.% of hemp shives estimated through two consecutive frequency sweep experiments are reported. The scans show that the moduli decrease while testing and the time interval between consecutive data capture increases with decreasing the frequency (see inset of Figure 4.3).

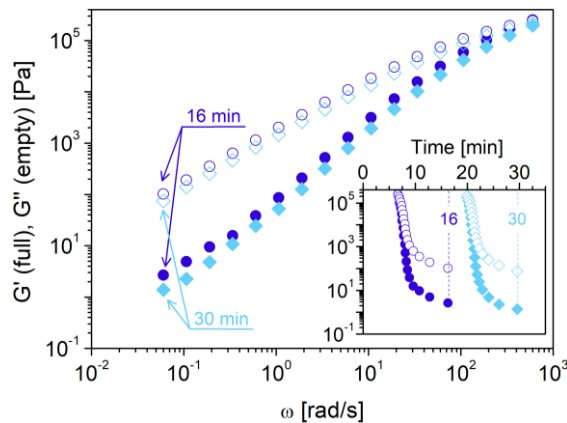


**Figure 4.3** Elastic and viscous moduli collected during two consecutive frequency scans (circles: first scan; diamonds: second scan) for the PLA composite loaded with 10 vol.% hemp shives. The inset reports the same data as a function of the acquisition time.

The time-resolved mechanical spectroscopy (TRMS), i.e., the study of the viscoelastic properties as a function of time, can be used as a tool to clean up the frequency dependence of the viscoelastic moduli from degradation phenomena [84]. Filippone et al. [85] [86] define a simple testing procedure based on a time sequence of frequency scans which allows to obtain an accurate estimate of the time evolution of the viscoelastic moduli by plotting the moduli as a function of the acquisition time. The

extrapolation procedure is reported in Figure 4.4, where the elastic and viscous modulus as a function of the acquisition time for the composite at 10 vol.% of hemp shives are shown at different frequencies. The decrease of viscoelastic moduli over time at every single frequency reflects the degradation kinetics of the specific dynamic population. At high frequencies, the response to the degradation of small chain fractions is explored. This specific dynamic population, since adapts to rapid deformations, is only slightly affected by the degradation. At low frequencies, however, the degradation effect on the dynamics of large portions of the chain is observed. In this case, the overall elasticity is strongly influenced by the alterations of the molecular architecture induced by the degradation.

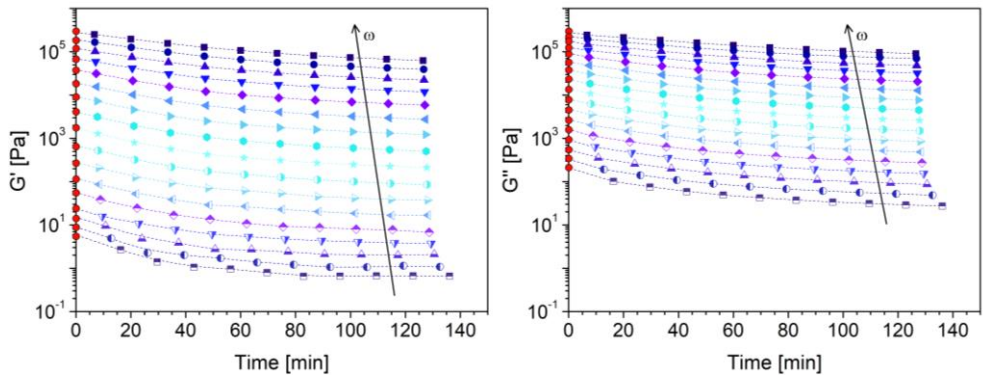


**Figure 4.4** Time evolution of elastic (left) and viscous (right) moduli for the composite at 10 vol.% of hemp shives. The red circles represent the extrapolated moduli at time-zero at each frequency.

The extrapolated elastic,  $G'(0)$ , and viscous,  $G''(0)$ , moduli at time-zero are reported as a function of frequency in Figure 4.5 for both the neat polymer and the composite systems. The neat polymer matrix shows a terminal Maxwellian behaviour ( $G' \sim 2$ ,  $G'' \sim 1$ ) at low frequency and a change in viscoelastic behaviour from mainly viscous to predominantly elastic above  $\omega=100$  rad/s. The addition of the fibres to the polymer matrix causes a significant increase in the moduli with  $\Phi$  especially at low frequencies, with a more pronounced effect on  $G'$  at low  $\omega$ . This behaviour points out that the melt state relaxation spectrum of the green composites is strongly affected by the fibre content. At high frequencies (short timescales) both  $G'$  and  $G''$  shift upwards without substantially changing their frequency

dependence. In this fast regime, the rheological response is dictated by the dynamics of portions of the polymer chains, which are only marginally affected by the presence of the fibres. The increase in rheological properties is only apparent, being explained by the concept of shear stress-equivalent inner shear rate: the actual deformation experienced by the polymer confined in the small gap between contiguous fibres is higher than what externally imposed, thus the measured moduli are higher than those of the unfilled matrix [87]. Much more interesting is the effect of the fibres at low frequency (longer timescales): as the mechanical oscillation slows down, the probed length scale increases and the effect of the fibres clearly emerge. Two behaviours can be identified depending on the fibre content. At low  $\Phi$ , the moduli only slightly increase with respect to the neat matrix and exhibit a reduced frequency dependence compared to the unfilled PLA (which approaches the Maxwellian behaviour,  $G' \sim \omega^2$  at low  $\omega$ ). At high  $\Phi$ , the effect is much relevant, with a clear flattening of  $G'$  indicative of a drastic slowing down of the relaxation dynamics. A true arrest (i.e., a frequency-independent  $G'$ ) is expected above  $\Phi_c$ .

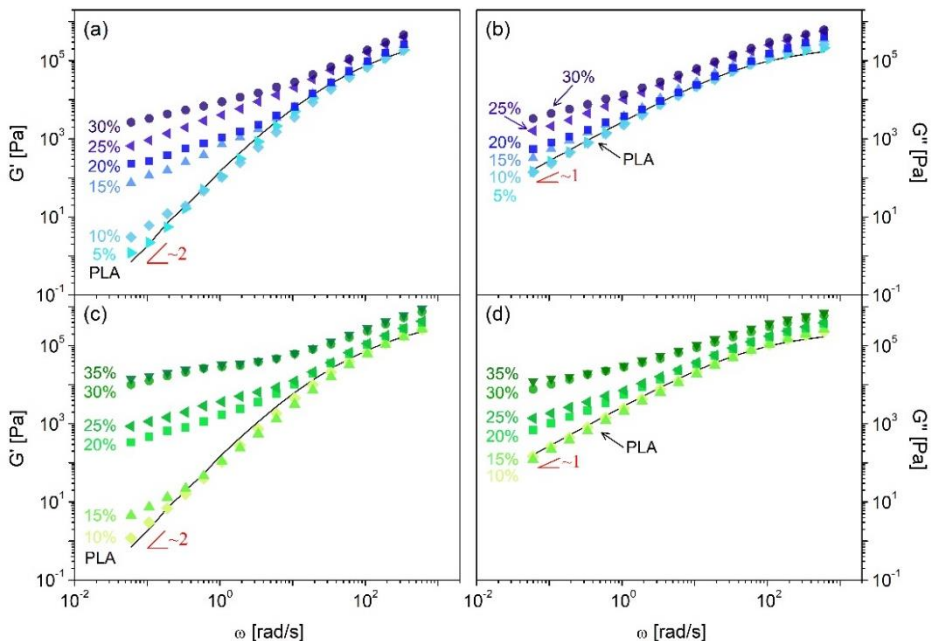


**Figure 4.5** Frequency dependence of the elastic ( $G'$ ) and viscous ( $G''$ ) moduli at time-zero of the PLA-based composites filled with hemp shives (a, b) and kenaf bast fibres (c, d) at different volumetric fibre loadings. The solid line represents the variation of moduli for the neat PLA.

In principle, looking for the plateau of  $G'$  is a simple way of identifying  $\Phi_c$ . Unfortunately, this condition is not observed in our samples, at least in the investigated frequency range. Exploring lower frequencies is difficult because of the rapid growth of the experimental times with decreasing  $\omega$ . To overcome this limitation, a simple rheological model, the “two-phase model”, was proposed, that is developed for polymer nanocomposites above  $\Phi_c$  [88].

Nanocomposites above  $\Phi_c$  can be depicted as a three-dimensional network of fractal clusters of nanoparticles embedded in the host matrix. This network has a predominantly elastic behavior that prevails over the elastic connotation of the polymer matrix. In contrast, the polymer is mostly responsible for the viscous connotation of the nanocomposite. As a result, the linear viscoelasticity of the material can be assumed as the result of the combination of the independent responses of (i) a “purely elastic” network of nanoparticles, and (ii) a “purely viscous” polymer. Despite such strong assumptions, the two-phase model is able to successfully capture the behavior of a wide variety of polymer nanocomposites [72], as well as of nanocomposites based on immiscible blends [74] [75]. The validity of the assumptions on the basis of the two-phase model is proved by building a master curve of  $G'$  of samples a different  $\Phi > \Phi_c$  using only two interrelated shift factors with a precise physical meaning: the vertical shift factor ( $b_\Phi$ ) is the elasticity of the filler network identified as the low frequency plateau of  $G'$ ; the horizontal shift factor ( $a_\Phi$ ) is the frequency at which the network elasticity equals the viscosity of the polymer matrix, defined as the viscous modulus of the neat polymer corrected to account for hydrodynamic effects due to the nanoparticles. Besides proving the correctness of the assumptions of the two-phase model, the master curve offers a simple way for identifying  $\Phi_c$ : because of the interrelation between the shift factors, only the  $G'$  curves of samples above  $\Phi_c$  can be deterministically scaled, while those of samples at  $\Phi < \Phi_c$  slide along a distinct track that does not superimpose to the master curve [73].

The studied composites are very different from polymer nanocomposites. The main differences are sketched in Figure 4.6. Unlike nanoparticles, which experience Brownian motions, depletion interactions, and other nanoscale phenomena that cause relevant rheological alterations even at low filler contents, the micron-sized fibers considered here have negligible rheological effects unless reaching high volume [89]. Nonetheless, it is assumed that the basic assumptions of the two-phase model hold irrespective of the size of the particles. To prove this statement, the  $G'$

curves of the composites starting from the highest compositions were scaled using the same procedure proposed for nanocomposites. The step-by-step procedure is reported below for both the systems object of the study.

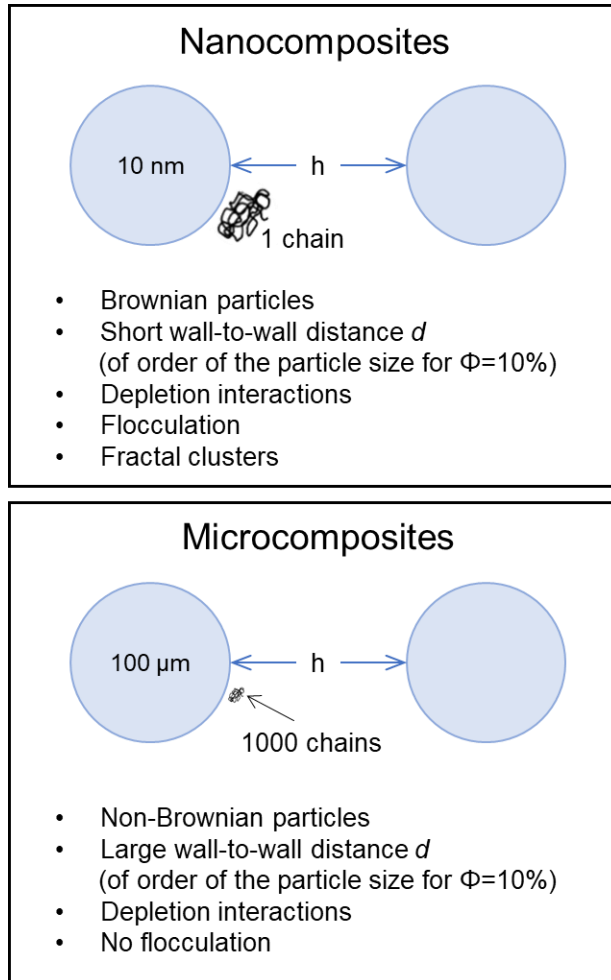


**Figure 4.6** Main differences between nano- and micro-composites. Schematic readapted from [90].

### *Two-phase model application*

In the building of the master curve, the first phenomenon to consider is the hydrodynamic effect triggered by the reduction of the effective gap distance available for the polymeric matrix between the particles. The

amplification factors related to the hydrodynamic interaction,  $B(\Phi)$ , are evaluated as the ratio between the complex modulus of the filled sample and that of the neat matrix ( $B(\Phi) = G^*(\Phi)/G^*_{PLA}$ ) in the high-frequency region i.e., where the rheological response is governed by the polymeric matrix behaviour. The normalization of the complex moduli with respect to  $B(\Phi)$  and the relative amplification factors are shown in Figure 4.7 for both composite systems.

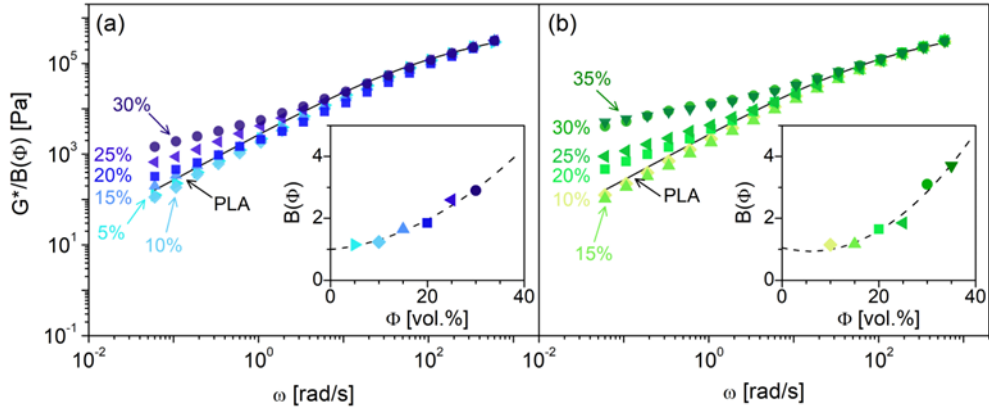


**Figure 4.7** Frequency dependence of the complex moduli at time-zero divided by the amplification factor for hemp shive (a) and kenaf bast (b) based composites at different volumetric fibre loadings. The solid line represents the complex modulus for the neat PLA. The insets show the amplification factor as a function of filler volume fraction (solid line is a guide for the eye).

The second step for building up the master curve of  $G'$  requires the identification of the horizontal ( $a_\Phi$ ) and vertical ( $b_\Phi$ ) shift factors, i.e., the points at which the network elasticity,  $G'_0(\Phi)$ , identified as the low-frequency plateau of the elastic modulus, equals the viscous modulus at the neat polymer amplified to account for the hydrodynamic effect,  $B(\Phi) \cdot G''_{PLA}$ . The shift factors can be easily defined for composites with strong fibre networks in which the elastic modulus plateau at low frequency is clearly recognizable. For these systems, the overlay of the  $G'$  curves is a direct consequence of the physical meaning of the shift factors. The two-phase model indeed reflects the physical picture of a filler network that scales along the viscous modulus of the neat matrix. Therefore, the chosen of the shift factors is bound: the vertical shift factor corrects to account for the hydrodynamic effect,  $b_\Phi/B(\Phi)$ , following the same functional dependence of the  $G''_{PLA}$ .

For composites with a more tenuous fibre network, the shift factors are identified using the predictive capacity of the two-phase model. In this case, the pairs  $(a_\Phi, b_\Phi)$  are obtained by looking for the overlay of the  $G'$  curve with the part of the master curve obtained for the composites at  $\Phi$  sufficiently high to identify  $G'_0$  clearly. This concept is explicated in Figure 4.6 for the composite at  $\Phi=15$  vol.% of hemp shives. Note that because the network elasticity is too weak to intercept the amplified viscous modulus of the matrix within the investigated frequency range, terminal Maxwellian behaviour has been assumed for the neat polymer ( $G'' \sim 1$ ). Three different pairs of shift factors have been identified (Figure 4.8a) and the related curves ( $G'/b$ ) are shown together with the master curve obtained for the highly loaded samples (Figure 4.8b). The results show that the shift factors identify a specific track in the plane  $G'/b_\Phi - \omega/a_\Phi$  and only one curve (blue triangles) lies onto the master curve. The pairs  $(a_\Phi, b_\Phi)$  associated with the latter are taken for granted.

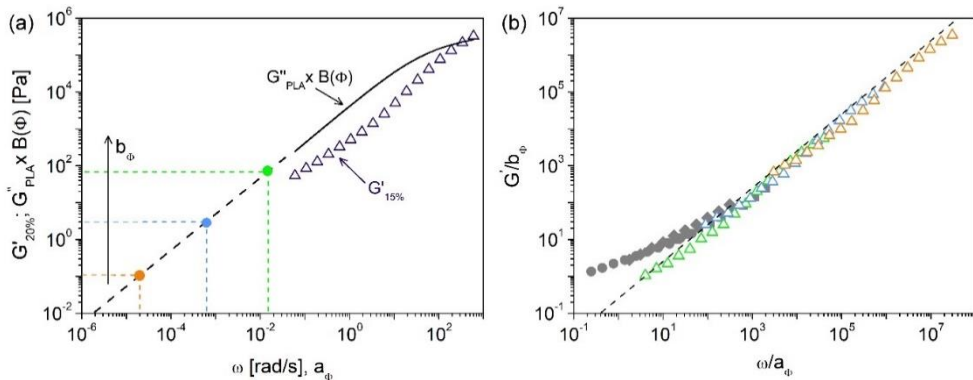


**Figure 4.8** (a) Three possible pairs  $(a_\Phi, b_\Phi)$  and (b) resulting scaled curves of  $G'(0)$  for the composite at  $\Phi = 15$  vol.%. In detail, in (a) the solid and dashed lines are the experimental data and extrapolated terminal behaviour of the viscous modulus at time-zero of PLA; the empty triangles are the elastic modulus at time-zero of the hemp shive composite at  $\Phi = 15$  vol.%. In (b) the three scaled curves (empty triangles) are superimposed on the master curve derived from samples at the highest filler contents (grey full symbols). The dashed line identified the tracks on which the above-mentioned curves can slide according to the two-phase model.

Repeating the same procedure for the samples that showed a tenuous network, the complete master curve is obtained for the two composite

systems (Figure 4.9). The identified shift factors are reported in the insets of Figure 4.9 for all scalable samples.

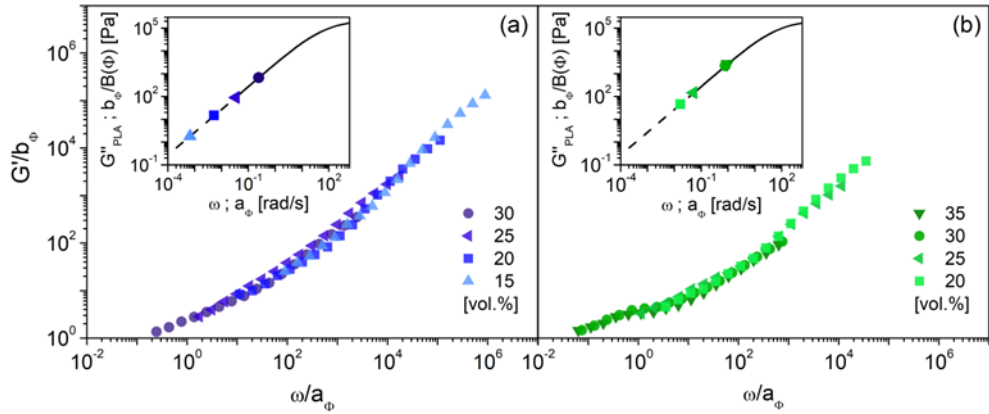


**Figure 4.9** Master curve of  $G'(0)$  for hemp shive (a) and kenaf bast (b) based composites at  $\Phi \geq 15\text{vol.}\%$  and  $\Phi \geq 20\text{vol.}\%$ , respectively. The frequency dependence of the  $G''_{\text{PLA}}$  at time-zero (solid line: experimental data; dashed line: extrapolated data) and the functional dependences  $b_{\phi}/B(\Phi)$  vs.  $a_{\phi}$  (full symbols) are shown in the insets.

According to the two-phase model physics, the  $G'$  curves of samples below the percolation threshold (i.e., without a continuous fibre network) do not scale on the master curve. Figure 4.10 shows three possible curves of  $G'(0)/b_{\phi}$  (red hexagons) for the composites at  $\Phi=10\text{ vol.}\%$  and  $\Phi=15\text{ vol.}\%$  of hemp shive and kenaf bast fibres, respectively. The resulting scaled curves identify a "track" (dash line) on which they slide for each pair ( $a_{\phi}$ ,  $b_{\phi}$ ) according to the two-phase model. No shift factors allow the scaled curve superposition on the master curve derived from samples at the highest filler contents. This behaviour indicates the absence of a continuous fibre network in the considered samples. The two-phase model thus allows to identify the range of compositions in which the percolation threshold must be searched, i.e., between the last scalable curve and the first non-scalable curve ( $10 < \Phi < 15$  for hemp shive-based composites and  $15 < \Phi < 20$  for kenaf bast-based composites.). In addition, the identification of the network elasticity of all the samples above  $\Phi_c$  as  $b_{\phi} = G'_0(\Phi)$  allows the accurate estimation of the percolation threshold as below reported in detail.

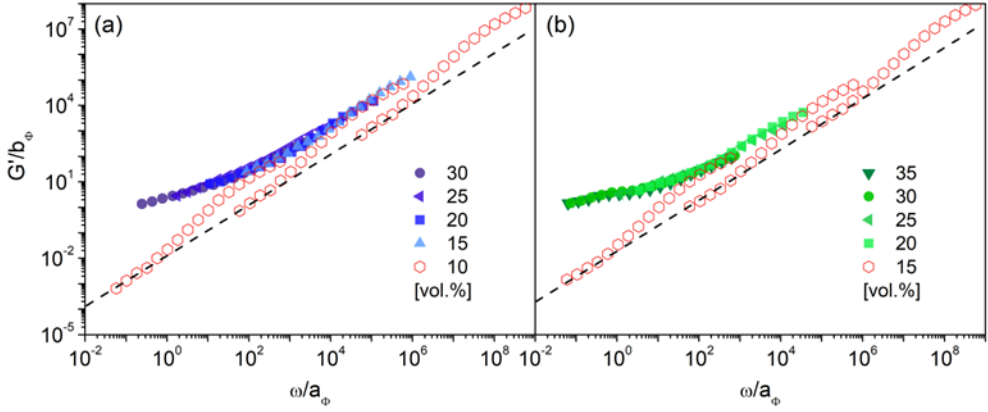


**Figure 4.10** Master curve of  $G'(0)$  for hemp shive (a) and kenaf bast (b) based composites at  $\Phi \geq 15\text{vol.}\%$  and  $\Phi \geq 20\text{vol.}\%$ , respectively. The curves at  $\Phi = 10\%$  (hemp shives composites) and  $\Phi = 15\%$  (kenaf bast composites) cannot be scaled onto the master curve (red empty hexagons). The dashed lines identified the tracks on which the above-mentioned curves can slide according to the two-phase model.

#### *Estimation of the percolation threshold*

In this work, the two-phase model application aims at the percolation threshold identification of composite systems loaded with micrometric natural fibres. The good quality of the results reveals that above  $\Phi_c$  the fibre content increase strengthens the fibre network preserving the overall structure. Furthermore, the model allowed the identification of the composition range in which the  $\Phi_c$  must be searched and the extrapolation of the network elasticity which is equal to the vertical shift factor ( $b_\phi$ ) for the building of the master curve. As predicted by the percolation theory, the critical behaviour of  $G'_0$  near  $\Phi_c$  is described by a power-law relationship:

$$G'_0 = k (\Phi - \Phi_c)^v \quad (4.10)$$

where  $k$  and  $v$  are two constants, the latter being related to the stress-bearing mechanism [63]. The Equation (4.10) has been fitted varying  $\Phi_c$  in the range where the critical behaviour of the network elasticity was observed:  $10 < \Phi < 15$  for hemp shive-based composites and  $15 < \Phi < 20$  for kenaf bast-based composites. Adopting such a procedure, the highest value of the determination coefficient,  $R^2$ , has been attained for a value of  $\Phi_c = 10.1 \text{ vol.}\%$  and  $\Phi_c = 19.5 \text{ vol.}\%$  for hemp shive and kenaf bast-based composites respectively, thus identifying their percolation threshold. The results of the fitting procedure are reported in Figure 4.11; the coefficients  $k$

and  $\nu$  for the different values of  $\Phi_c$  are summarized in Table 4.3 together with the regression coefficient  $R^2$ .

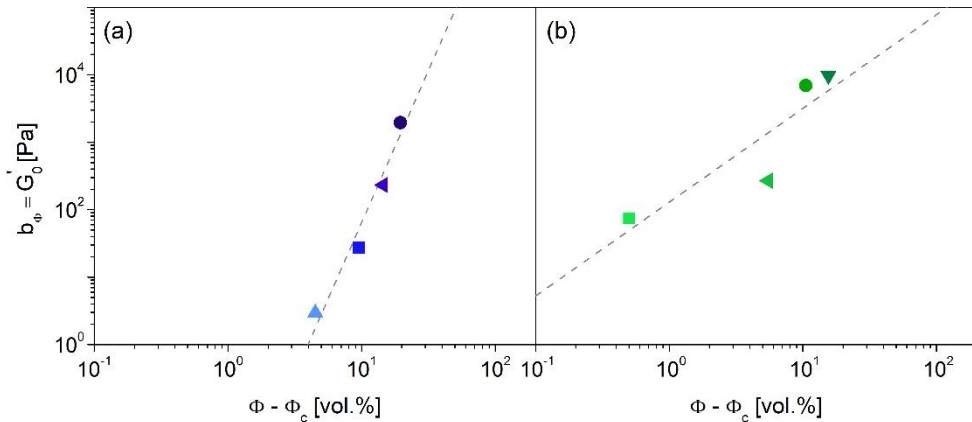


**Figure 4.11** Power-law dependence of the network elasticity above  $\Phi_c$ . The dashed line is the fitting of Equation (4.10) to the experimental points setting  $\Phi_c = 10.1$  vol.% for hemp shive-based composites (a) and  $\Phi_c = 19.5$  vol.% for kenaf bast-based composites (b).

**Table 4.3** Parameters  $k$  and  $\nu$  obtained for different values of  $\Phi_c$  by fitting Equation 4.10 to the experimental data.

$\Phi_c$ [%]	$k$ [Pa]	$\nu$	$R^2$
<i>Hemp shive based-composites</i>			
<b>10.1</b>	<b>0.002</b>	<b>4.51</b>	<b>0.9780</b>
10.5	0.003	4.30	0.9754
11	0.008	4.03	0.9666
12.5	0.106	3.18	0.9518
14.9	24.171	1.07	0.7175
<i>Kenaf bast based-composites</i>			
15.1	0.131	3.77	0.8474
17	2.062	2.90	0.8793
19	48.481	1.78	0.9271
<b>19.5</b>	<b>129.321</b>	<b>1.39</b>	<b>0.9311</b>
19.9	410.072	0.889	0.8797

The corresponding values of  $k$  and  $v$  at  $\Phi_c$  are in line with those predicted or experimentally derived for different systems [19], but they will not be discussed here for the sake of brevity. The  $\Phi_c$  for the hemp (10.1%) agrees with the theoretical prediction for randomly distributed fibers (see Table 4.2). The  $\Phi_c$  for the kenaf fibers (19.5%) is substantially higher, close to the upper limit of parallel alignment of the fibers. This is in contrast with the theoretical expectations, according to which the  $\Phi_c$  of kenaf fibers should be lower than that of hemp ones. The reason for such a discrepancy must be sought in the morphological differences between the two types of fibers. The longer kenaf fibers are more inclined to orient and align during melt processing. Fiber flexibility could also play a role. Bending and folding of the kenaf fibers during the intensive mixing process may have increased the volume fraction needed for percolation. In any case, the difference between the  $\Phi_c$  for the two systems is confirmed also by dielectric measurements.

#### 4.4 Estimate of $\Phi_c$ through dielectric spectroscopy

Dielectric spectroscopy (DS) is a technique frequently used to evaluate the response of a sample subjected to an applied electric field of fixed or changing frequency [91] [92]. This technique allows measuring the frequency dependence of the material dielectric constant,  $\varepsilon$ , which indicates the material's aptitude to become polarized and store charge when subject to an electric field applied through parallel plates acting as a capacitor. The capacitance of the capacitor,  $C$ , is directly proportional to  $\varepsilon$  through the following expression:

$$\varepsilon = \frac{C d}{A} \quad (4.11)$$

where  $d$  represents the thickness of the sample material, and  $A$  is the area of the electrode. The dielectric constant is a complex number where the real part,  $\varepsilon'$ , the so-called permittivity, characterizes the energy storage during the cycle, the imaginary part,  $\varepsilon''$ , named the dielectric loss factor, is the dissipation term. The dielectric response of the material depends on the polarizability of its molecules. The type of polarization can be distinguished according to the mechanism that occurs in the process. The four familiar types of polarization mechanisms are atomic/electronic, ionic, dipolar, and interfacial polarization. Atomic and electronic polarization occur at high frequencies, are instantaneous, and do not affect the dielectric constant dependence on frequency. Ionic polarization can be observed in ionic solids

and is commonly detected in ceramics, inorganic crystals, and glasses. The presence of polar groups in the material triggers dipolar polarization. Interfacial polarization affects dielectric properties at very low frequencies and usually decreases with increasing frequency. This polarization type occurs in a composite due to the different conductivity or polarization between the matrix and fillers [93] [94].

In this chapter, the dielectric properties of natural fibre based-composites in water-saturated conditions are evaluated to validate the  $\Phi_c$  values obtained through the proposed rheological method. Dielectric spectroscopy allows you to evaluate the dielectric properties variation of the material during the progressive absorption of water. The formation of a continuous network of highly hydrophobic fibres promotes the access of water molecules inside the polymeric matrix causing a high increase in the dielectric constant when the saturated condition is reached [76] [77] [78]. To estimate the percolation threshold of the green composites, the attention was focused on  $\epsilon''$ , which is correlated to the real part of the complex conductivity,  $\sigma'$ , through the relationship  $\sigma' = \epsilon_0 \epsilon'' \omega$  ( $\epsilon_0 = 8.85 \times 10^{-12} \text{ Fm}^{-1}$  permittivity of free space).

### *Moisture absorption*

To evaluate the dielectric properties of natural fibre-based composites, the first step provides the water soaking of the samples until the saturation conditions are reached. In detail, samples with different volumetric fibre contents were immersed in water at  $T = 30^\circ\text{C}$  under an agitation speed of 120 rpm. The dimensions of the samples are  $2.5 \times 1.2 \times 0.3 \text{ cm}$ . To monitor the weight changes until the saturation point, the samples were removed from the water at specific time intervals and carefully dried with absorbing paper. Water absorption was evaluated by the weight gain relative to the dry weight of the samples using a micro-balance accurate to 10 mg. Percentage weight variation during water sorption,  $M(t)$  was computed as follows:

$$M(t) = \frac{W_t - W_0}{W_0} \quad (4.12)$$

where  $W_0$  and  $W_t$  denote the mass of the dried specimen and weight at any specific time  $t$ , respectively. No additional daily weight gain is recorded when the samples reach the saturation condition. The percentage weight measured in this condition is the saturation weight,  $M_s$ . Assuming, for

simplicity, the validity of Fick's law it is possible to estimate the diffusion coefficient D according to the following Equation:

$$\frac{M(t)}{M_s} = \frac{4}{d} \left( \frac{D t}{\pi} \right)^{\frac{1}{2}} \quad (4.13)$$

where  $M_s$  is the saturation weight, and  $d$  is the initial thickness of the sample. Equation 4.13 indicates that  $D$  can be determined in the linear region of the weight gain plot. In this zone,  $M(t)/M_s$  is a linear plot of  $t^{1/2}$  that allows the calculation of the diffusion coefficient from the slope,  $\theta$  [95]. Thus, the diffusion coefficient can be calculated as follows:

$$D = \frac{\pi d^2 \theta^2}{4} \quad (4.14)$$

However, Equation 4.14 is valid for a one-dimensional shape. To apply this expression to three-dimensional shapes, the Stefan approximation can be considered (Equation 4.15) [96]:

$$D_c = D \left( 1 + \frac{d}{h} + \frac{d}{w} \right)^{-2} \quad (4.15)$$

where  $D_c$  is the corrected diffusion coefficient, related to the geometry of the immersed specimen,  $h$  being the length and  $w$  the width of the same. This equation assumes that the diffusion rates are the same for all directions [97].

The time evolution of the sample percentage weight variation during the water absorption process is reported in Figure 4.12. The weight gain follows the typical behaviour described by Fick's law for both composite systems. An initial stage with rapid weight gain is followed by a second stage with an asymptotic behaviour until reaching the saturation point beyond which no further water is absorbed. As expected, the neat PLA shows the lowest water uptake values with a saturation weight of 0.8 wt.% after 10 days that remains constant until 30 days (Figure 4.12). This poor weight variation demonstrates that the matrix has little effect on the water absorption process of the analysed systems. A significant increase in saturation weight and time occurs with the addition of natural fibres. As it can be seen, the saturation weight for the hemp shive-based composite at 30 vol.% is 6.5 wt.% for an immersion time of 30 days which is eight times greater than the value of

unfilled PLA. During the water absorption process, the water penetrates for the capillarity effect and attaches to hydroxyl groups of cellulose and hemicellulose that can readily interact with water molecules thus allowing water to enter the composite material [98]. Then, the natural fibres swell and expand due to the water absorption effect until to reach the saturated condition [99]. As the fibre content increase, water uptake occurs to a greater extent achieving high saturation values.

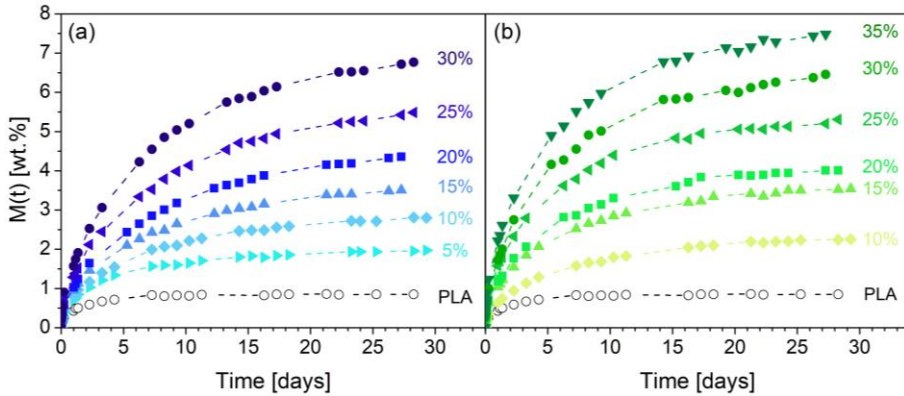


**Figure 4.12** Weight change as a function of soaking time in the water at 30°C for hemp shives (a) and kenaf bast (b) based composites at different volumetric fibre loadings compared to the pure PLA. The lines are guides for the eye.

The natural fibre type affects the water absorption of the green composites. The saturation weight is indeed slightly lower for kenaf bast based composites than for the hemp shive composites for the same fibre content. This behaviour can be related to the higher absorption capacity of the hemp shive fibres. Isothermal tests carried out at  $T = 110^{\circ}\text{C}$  on water-saturated fibres revealed a water content of  $83.3 \pm 1.5$  wt% and  $63.8 \pm 2.0$  wt% for hemp shives and kenaf bast fibres, respectively (see Figure 3.1 in Chapter 3). The greater absorbency of the hemp shives can be attributed to the higher content of hemicellulose (see Table 3.1 in Chapter 3) which is the element responsible for moisture absorption [12]. The slope values of  $M(t)/M_s$  vs.  $t^{1/2}$  ( $\theta$ ), the diffusion coefficients ( $D$ ), and the corrected diffusion coefficients ( $D_c$ ) for the neat PLA and both the composite systems are reported in Table 4.4.

**Table 4.4** Values of slope of  $M(t)/M_s$  curve ( $\theta$ ), diffusion coefficient ( $D$ ), and corrected diffusion coefficient ( $D_c$ ) for hemp shive and kenaf bast-based composites at different volumetric fibre content compared to the neat PLA.

$\Phi$ [vol.%]	$\theta \times 10^{-3}$ [ $s^{-1/2}$ ]	$D \times 10^{-8}$ [ $cm^2 s^{-1}$ ]	$D_c \times 10^{-8}$ [ $cm^2 s^{-1}$ ]
<i>Neat PLA</i>			
0	0.7	4.23	2.30
<i>Hemp shive based-composites</i>			
5	1.7	5.07	2.80
10	2.6	4.96	2.71
15	3.3	5.87	3.23
20	3.8	5.96	3.29
25	4.6	5.59	3.04
30	5.9	5.44	3.00
<i>Kenaf bast based-composites</i>			
10	2.0	5.40	2.94
15	3.2	5.66	3.10
20	3.9	5.91	3.23
25	5.2	6.56	3.59
30	6.4	6.61	3.60
35	7.5	6.94	3.72

A clear increasing tendency in diffusion coefficient occurs with the increasing fibre content to a greater extent for the kenaf bast based composites. Pure matrix possesses a corrected diffusion coefficient of  $2.30 \times 10^{-8} cm^2 s^{-1}$  which is in total agreement with other values reported in the literature [100] [97]. The addition of 30 vol% of natural fibres to PLA composites results in a 30% and 60% increase in the corrected diffusion coefficient for hemp shives and kenaf bast based composites, respectively. The different behaviour of the composite systems could be associated with the different water absorption capacities of the natural fibres used (see Chapter 3, Section 3.1).

#### *Estimate of dielectric loss factor in water-saturated conditions*

To identify the percolation threshold of the green composites, dielectric spectroscopy tests were carried out during the progressive water absorption. A rotational rheometer (ARES, Rheometric Scientific) equipped with a dielectric thermal analysis tool, constituted by a couple of stainless-steel parallel plates (diameter 25 mm) connected with a LCR Meter (E4980A, Agilent) was used to monitor the dielectric property variation. A constant

compressive force was applied to ensure contact between the sample and the parallel plates. For each sample, dielectric measurements were performed at room temperature by monitoring the permittivity,  $\epsilon'$ , and the dielectric loss factor,  $\epsilon''$ , as a function of the frequency,  $\omega$ , in the range  $20 - 6 \cdot 10^4$  Hz. The frequency dependence of permittivity and dielectric loss factor is reported in Figure 4.13 for samples tested after about 10 days of water soaking.

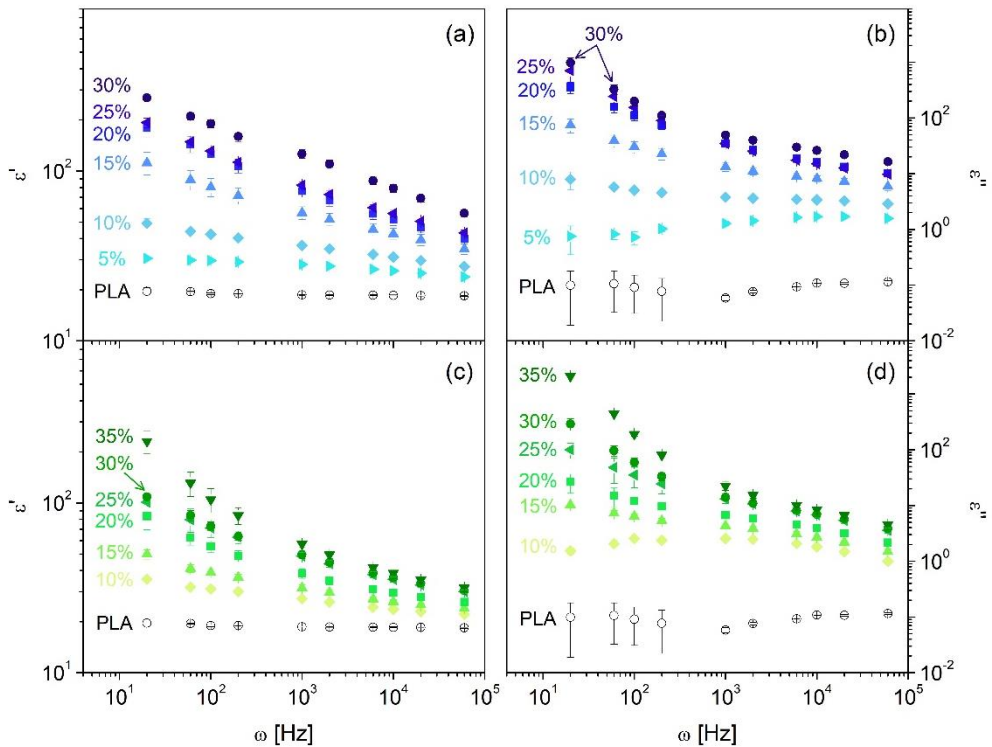


**Figure 4.13** Frequency dependence of the permittivity ( $\epsilon'$ ) and dielectric loss factor ( $\epsilon''$ ) for hemp shives (a) and kenaf bast (b) based composites at different volumetric fibre loadings compared to the pure PLA. The results show the material dielectric properties after 10 day of water soaking.

The results show that the dielectric properties progressively increase with the fibre loading over the entire range of frequencies. For the composite systems, in the frequency range considered, the dielectric constant depends on two polarization mechanisms: dipolar and interfacial polarization. The first is due to the water molecules which penetrate and attach to hydroxyl groups of the natural fibres, the latter occurs for the differences in conductivities or polarizations of the matrix and fibres [76]. Both

contributions are influenced by the fibre contents as generate an interfacial region growth and an increase of the polar groups. As a result, the neat matrix shows the lowest values of permittivity and dielectric loss factor that increase with the fibre loading. Furthermore, at low frequencies, the dielectric properties show higher values since the complete orientation of the molecules is possible only at lower frequencies and the dipolar polarization requires long timescales to reach the equilibrium static field value. The greater intensity of the dielectric loss factor at low frequencies (Figure 4.13) makes this parameter an excellent candidate for monitoring the dielectric property variation of composites during the water absorption process. The time evolution of  $\epsilon''$ , at the lowest frequency measured (20Hz), is reported in Figure 4.14 for samples at different fibre loadings. The dielectric loss factor increases over time to reach a constant value ( $\epsilon''_s$ ) in correspondence to the water saturation condition of the samples. The large dipolar character of the water absorbed by the natural fibres gives a strong increase in the dipolar polarization of the samples over time and with the fibre content. In detail, while the dielectric loss factor of the neat matrix remains constant, in composite systems the growth of the hydroxyl groups with  $\Phi$  involves a significant increase in the dielectric loss factor.

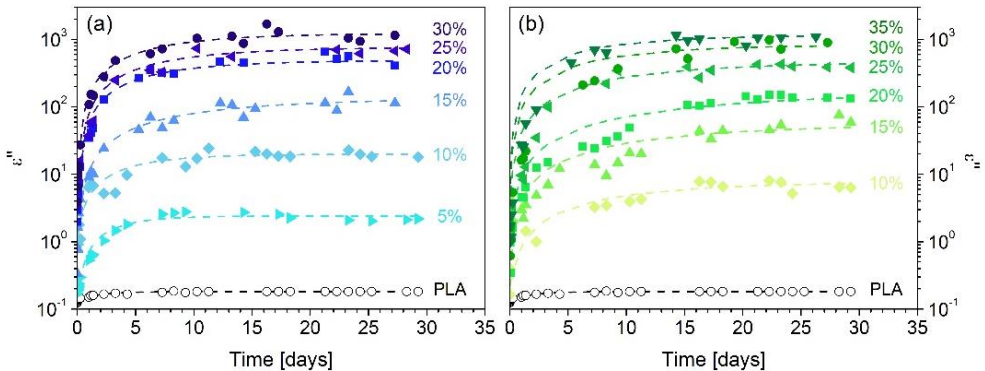


**Figure 4.14** Dielectric loss factor at 20Hz as a function of soaking time for hemp shives (a) and kenaf bast (b) based composites at different fibre loadings compared to the pure PLA. The dash lines are guide for the eye.

Figure 4.15 reports the dielectric loss factor for water-saturated samples,  $\epsilon''_s$ , as a function of the fibre content. A sudden increase in dielectric loss factor was noticed in the range  $10 < \Phi < 15$  and  $15 < \Phi < 20$  for hemp shive and kenaf bast based composites, respectively. This critical behaviour can be associated with the formation of a continuous fibre network inside the

composite materials that allow water absorption by the fibres trapped in the polymeric matrix. Unlike, under the percolation threshold, only the fibres close to the surface absorb water molecules.

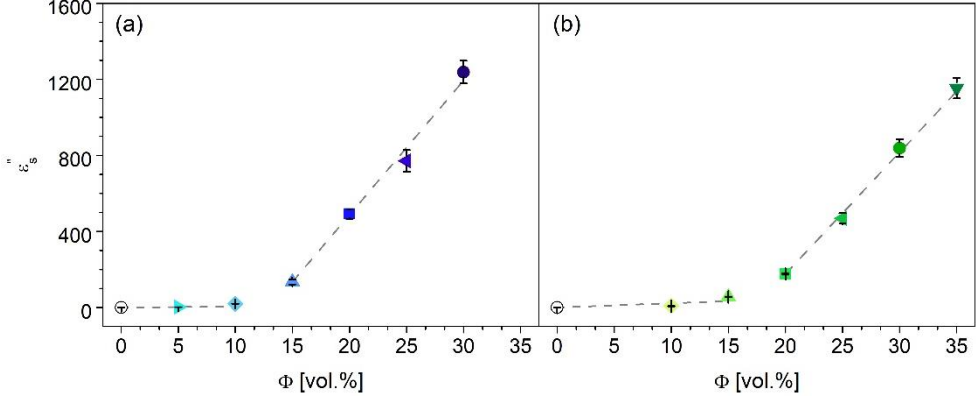


**Figure 4.15** Dielectric loss factor for water-saturated samples as a function of filler content: hemp shives (a) and kenaf bast (b) based composites.

#### *Identification of the percolation threshold*

Dielectric spectroscopy was used to validate the rheological estimates of  $\Phi_c$ . The inherent hygroscopicity of natural fibers allows to identify percolating paths in the samples above  $\Phi_c$ . Since PLA absorb negligible amounts of water compared to the fibers (Figure 4.12) transition in the dielectric behavior under saturation conditions can be ascribed to the fibers (Figure 4.15). In particular, the formation of a percolating network of water-containing fibers is associated with a plateauing of the real part of the complex conductivity,  $\sigma'$ , indicative of direct current-like imperfect charge transport [101]. The low frequency  $\sigma'$  value,  $\sigma'_0$ , is a good estimate of the sample electrical conductivity, which is expected to exhibit power-law dependence on fiber content above  $\Phi_c$ :

$$\sigma'_0 = h (\Phi - \Phi_c)^\mu \quad (4.16)$$

$h$  and  $\mu$  being coefficients that depend on the conductive mechanism [63].

The real part of the complex conductivity,  $\sigma'$ , is correlated to the dielectric loss factor,  $\epsilon''$ , through the following relationship:

$$\sigma' = \varepsilon_0 \varepsilon'' \omega \quad (4.17)$$

where  $\varepsilon_0 = 8.85 \times 10^{-12} \text{ Fm}^{-1}$  is the permittivity of free space.

The frequency-dependent real part of the complex conductivity is plotted in Figure 4.16 for water-saturated samples of different compositions.

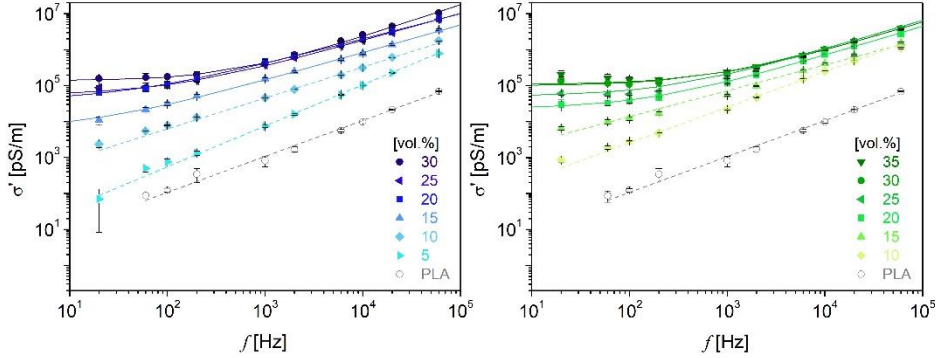


**Figure 4.16** Real part of the complex conductivity for hemp- (left) and kenaf-based (right) composites at different fiber content. The samples were equilibrated in tap water for  $\sim 3$  weeks. Lines are the fitting of the alternated current universal law to the data.

A plateau of  $\sigma'$  is only noticed at  $\Phi \geq 10\%$  for the hemp-based systems and  $\Phi \geq 15\%$  for the kenaf-based ones. This means that the percolation thresholds must be sought in the  $\Phi$ -intervals 10-15% and 15-20% for hemp and kenaf, respectively. For an accurate estimate of the  $\Phi$ -dependent  $\sigma'_0$  values, we fit the alternated current universal law,  $\sigma'(f) = \sigma'_0 + Af^u$  [102] [103], to the experimental data. Then, in analogy with what we did with the network elasticity data, we fitted Equation (4.16) to  $\sigma'_0$  data for different values of  $\Phi_c$  falling in the identified intervals, looking for the maximization of  $R^2$ .

The so-obtained (di)electrically derived percolation thresholds were 10.1% and 18.5% for the hemp- and kenaf-based systems, respectively. The critical scaling of  $\sigma'_0$  is shown in Figure 4.17. The discrepancy between the percolation threshold with the two types of fibers, which already emerged from the rheological analysis, is confirmed. This restates how difficult is the theoretical estimate of the percolation threshold in real composites based on natural fibers. More importantly, the (di)electrically computed  $\Phi_c$  values are

in very good agreement with the rheologically derived ones. Since electrical and rheological percolation takes place at very similar filler content [104], we can conclude that the proposed rheological method is an effective method for the estimate of the percolation threshold in challenging materials such as green composites. We observe that dielectric measurements required a laborious procedure for the samples to absorb the equilibrium water content, with the need for continuous monitoring of sample weight and dielectric parameters over long experimental timescales (about three weeks) dictated by the characteristic diffusion time of the water in the fibers (Figure 4.17). In contrast, a single set of simple linear viscoelastic measurements, analyzed in the framework of the two-phase model, is sufficient to lead to the same result with the same degree of accuracy.

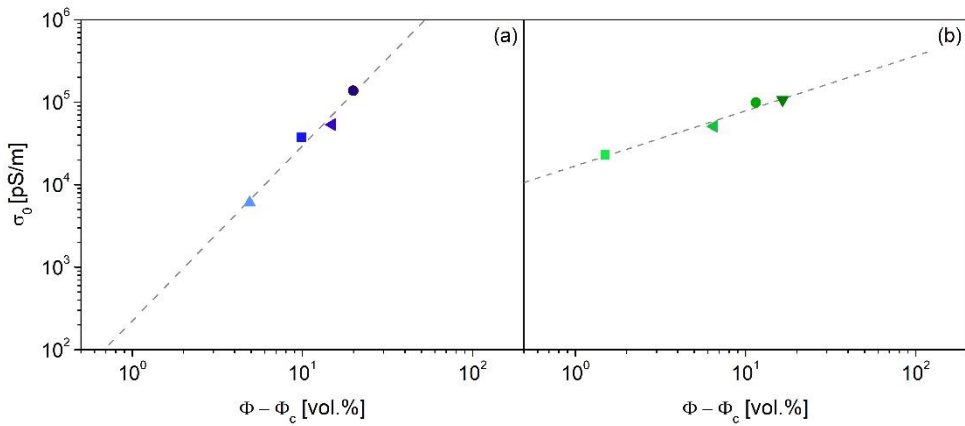


**Figure 4.17** Scaling of the network elasticity as a function of  $\Phi - \Phi_c$  for the hemp- (a) and kenaf-based (b).

# Degradation process study of green composites

## 5.1 Purpose and structure of the study

In this chapter, a description of the natural fibre effect on a host biodegradable polymer matrix is provided. Contrary to what is commonly perceived, biodegradation of such materials in the natural environment can be a very slow process, with obvious consequences in terms of their actual environmental sustainability. From a chemical point of view, the biodegradation of polymer matrices is the result of the combined effect of water and microorganisms: the former induces hydrolysis of the polymer, while the latter digests the shortened chains and mineralizes the material. Natural fibres play a crucial role in this process, as they favour the access of water and microorganisms from the external environment, hence triggering the phenomenon. The best conditions to promote biodegradation are still debated (see Chapter 2 for more details).

In this study, preliminary analyses after composite processing were carried out to assess the effect of the production process on polymer matrix degradation. Subsequently, the natural fibre effect on the matrix degradative phenomena in melt and solid states were investigated. In detail, degradation phenomena in the melt state were examined by rheological analysis to evaluate degradation over time of the green composites. Field and laboratory tests were instead performed to evaluate the green composite degradation in the solid state. The former mimic environmental conditions experience in real applications; the latter are useful for their short duration and the possibility of monitoring the progress of biodegradation. As a laboratory test, hydrolytic degradation *in vivo* was carried out to provide insight into degradation rates and erosion behaviour *in vivo*. For field tests, however, the samples were subjected to biodegradation tests by burial in a mature green compost in order to evaluate their behaviour in real conditions. For all the experiments considered, the degradation rate is estimated by evaluating physical and chemical changes in PLA and green composites. A

parameter usually used to monitor the degradation process is weight loss, though often difficult to measure since all small fragments must be collected and recovered once the material disintegrates. More accurate parameters to give indications of the degradation of the material are the variation in crystallinity degree, molecular weight, and mechanical performances.

## 5.2 Processing effect on green composites

Aliphatic polyesters like PLA are biodegradable polymers susceptible to chemical hydrolysis of the ester backbone in aqueous environments [105]. This characteristic makes them particularly interesting for applications in which biodegradability is desirable [106], but is also one of the main issues when these polymers are processed. Hydrolytic chain scission of ester linkage is in fact also the fastest and most effective degradation process which polyesters undergo during processing. Therefore, the presence of weak hydrolysable bonds makes the material sensitive to moisture and heat [107] [108] and thus their properties are extremely sensitive to stocking, processing, and use conditions [109] [110]. Given the strong dependence of polyesters on processing conditions, preliminary analyses of the samples after processing were carried out to assess the effect of the production process on the polymer matrix degradation.

Differential Scanning Calorimetry was performed using a TA Instrument DSC Q2000 to evaluate the degradation effects on the thermal transitions and on the matrix crystallinity degree. The analyses were carried out under inert nitrogen flux (50 mL/min) on  $12 \pm 2$  mg samples in non-hermetically closed aluminium pans. Three successively dynamic measurements were performed at 10°C/min heating/cooling rates: a first heating scan from 30 to 200°C, a cooling scan up to 30°C, and a second heating scan up to 200°C. The glass transition temperature ( $T_g$ ), cold crystallization temperature ( $T_{cc}$ ), melting temperature ( $T_m$ ), cold crystallization enthalpy ( $\Delta H_{cc}$ ), and melting enthalpy ( $\Delta H_m$ ) were determined from the first heating curves.  $T_{cc}$  and  $T_m$  were taken from the peak temperature of the cold crystallization and the melting respectively. Instead,  $T'_{cc}$  and  $T'_m$  refer to the onset temperature of the cold crystallization exotherm peak and the melting endotherm peak respectively. The crystallization degree ( $\chi$ ) was calculated from the thermograms measured during the first heating scan according to the following expression:

$$\chi = \left( \frac{\Delta H_{m(t)} - \Delta H_{cc(t)}}{\Delta H_m^0 \times \left(1 - \frac{\%wt_{fiber}}{100}\right)} \right) \times 100 \quad (5.1)$$

where  $\Delta H_{m(t)}$  and  $\Delta H_{cc(t)}$  are the melting and cold crystallization enthalpy respectively of the test sample at time  $t$  of degradation;  $\Delta H_m^0$  is the latent heat of crystallization of a fully crystalline PLA (93.0 J/g [111] [107]) and  $\%wt_{fiber}$  is the weight percentage of fibre. To evaluate the effect of the manufacturing process on the neat PLA and green composites, the first heating scan was considered since it represents the material status after processing. The DSC thermograms and data of the first heating scan are shown in Figure 5.1 and Table 5.1 respectively.

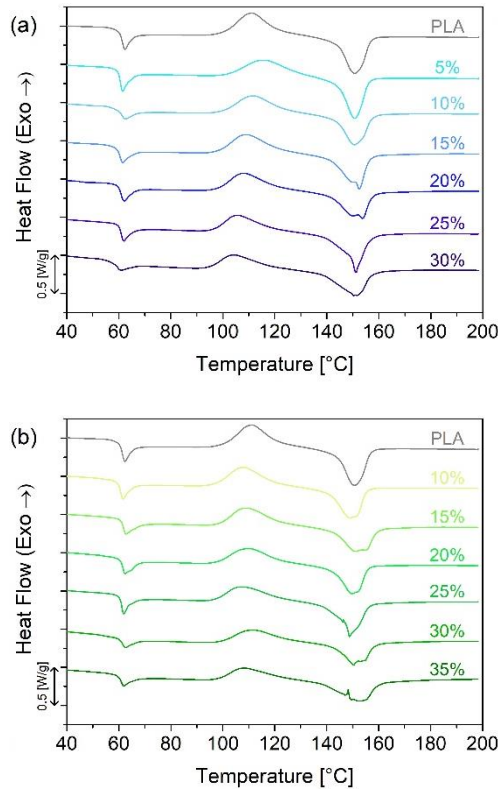


**Figure 5.1** DSC thermograms of hemp shive (a) and kenaf bast (b) based composites at different volumetric fibre content after processing, first heating scan.

**Table 5.1** DSC data on hemp shive and kenaf bast-based composites at different volumetric fibre content compared to the neat PLA after processing by first heating curves.

$\Phi$ [vol.%]	$T_g$ [°C]	$T'_{cc}$ [°C]	$\Delta H_{cc}$ [J/g]	$T'_m$ [°C]	$\Delta H_m$ [J/g]	$\chi$ [%]
<i>Neat PLA</i>						
0	61.41	100.53	24.74	143.22	26.64	2.04
<i>Hemp shive-based composites</i>						
5	60.72	100.92	21.45	141.90	23.85	2.75
10	61.39	100.01	21.91	141.44	23.82	2.33
15	60.54	98.40	22.46	140.14	24.40	3.45
20	60.96	98.24	20.51	138.88	25.37	6.82
25	61.09	96.76	17.82	136.88	26.50	13.13
30	59.78	95.06	15.82	135.57	25.72	16.21
<i>Kenaf bast-based composites</i>						
10	60.71	97.30	21.62	140.28	24.83	3.94
15	61.93	98.74	20.15	139.47	22.70	3.35
20	61.70	97.71	18.37	139.33	21.45	4.36
25	61.22	98.84	18.24	135.23	23.97	8.76
30	61.29	99.08	15.87	134.50	20.75	9.75
35	60.66	98.07	15.13	134.85	22.32	13.00

The following transitions are observed along the increasing temperature axis: glass transition (between 50°C and 70°C), cold crystallization (between 90°C and 130°C), and melting process (between 130°C and 160°C). In detail, the glass transition region allows to evaluate the degradation effect on the amorphous molecular chains. The results show an endothermic phenomenon, the structural relaxation, overlapped with the glass transition [112] [113]. The reason for this endothermic peak is a change in the kinetics of unfreezing [114]. The intensity of the structural relaxation peak decreases increasing the volumetric fibre content indicating that the natural fillers in some way changed the morphology of the amorphous fractions in the polymer during the cooling process [115]. The  $T_g$  is calculated as the temperature at the inflection point of the phenomenon and it is located at  $61.0 \pm 0.6$  for all the samples. Therefore, the natural

fibres did not cause relevant changes in the glass transition region during the manufacturing process. When the glass transition is overcome, the cold crystallization phenomenon starts. For the neat PLA, the cold crystallization starts at around 100°C, since the chains, which were constrained in the glassy state, have the condition to freely crystallize, and at around 112°C the exothermic peak is situated. The natural fibres addition in the polymer matrix causes a shift of cold crystallization peak to a lower temperature and a decrease in its intensity with their content increase (Figure 5.1). The slight reduction of  $T'_{cc}$  (Table 5.1) reveals that the natural fibres promote the formation of polymeric chains able to cold crystallize at lower temperatures. In addition, the cold crystallization enthalpy decrease suggests that the natural fibres did not cause degradation phenomena during the manufacturing process since an increase in the number of chains involved in cold crystallization has not been registered [113]. The last thermal transition is the melting process. The presence of two endotherm convoluted peaks at high fibre contents indicates the formation of two different crystalline distributions. The lowest melting temperature peak corresponds to the population with a lower size, and the highest peak indeed identifies the crystalline conformations with the larger size. The natural fibre addition again causes a slight reduction of the onset temperature of the melting peak (Table 5.1). The crystallization degree was calculated according to Equation 5.1. Both the composite systems show an increase in the crystallization degree at the high fibre contents. This phenomenon can be explained by: (i) the presence of smaller, faster-crystallizing molecules resulting from the degradation of the PLA during the manufacturing process [116], (ii) the effect of the natural fibres that, as is well known, can act as nucleating agents and provide many compact nucleation sites on their fibre surface [117] [118] [119].

Size Exclusion Chromatography (SEC) analyses were run to correlate the matrix crystallinity degree variation to degradation phenomena during the manufacturing process. Before injecting the solute through SEC columns, the samples were diluted in Chloroform and then filtered using a 0.2 mm Teflon filter to extract insoluble components. The pure PLA and the hemp shive-based composites at 10, 20, and 30 vol.% of fibres were analysed, and the weight average molecular weight ( $M_w$ ) of the matrix after the manufacturing process is reported in Table 5.2. The SEC measurements were only conducted on the hemp shive composites since they have a higher water content compared to kenaf bast fibres as reported in Chapter 3 in Section 3.1. The water is the responsible element for the PLA hydraulic degradation and thus a possible increase in matrix crystallinity degree. The

results show a molecular weight decrease of the composites negligible compared to the neat matrix. Therefore, the  $\chi$  increase with the fibre content is mainly related to the nucleation process induced by the natural fibres since the contribution of the matrix degradation is negligible.

**Table 5.2** Molecular weight of pure PLA and hemp shive-based composites at 10, 20 and 30 vol.% of fibres after manufacturing process.

$\Phi$ [vol.%]	$M_w$ [g/mol]
0	115000
10	112400
20	102000
30	110000

The cooling scan only shows the glass transition phase not providing any information related to the process effect on the polymeric matrix. Finally, the same thermal transitions as shown in the first scan develop in the second heating scan as reported by the thermograms shown in Figure 5.2. An interesting result is observed in the crystallization degree (Table 5.3). No relevant variation of  $\chi$  is noted with the natural fibre increase. This result may suggest that a controlled cooling process does not trigger the nucleating effect of the natural fibres.

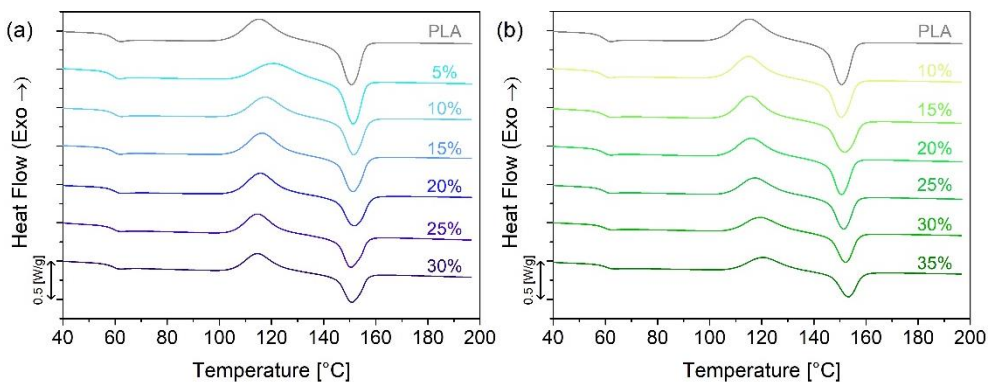


**Figure 5.2** DSC thermograms of hemp shive (a) and kenaf bast (b) based composites at different volumetric fibre content after processing, second heating scan.

**Table 5.3** DSC data on hemp shive and kenaf bast-based composites at different volumetric fibre content compared to the neat PLA after processing by second heating curves.

$\Phi$ [vol.%]	$T_g$ [°C]	$T'_{cc}$ [°C]	$\Delta H_{cc}$ [J/g]	$T'_m$ [°C]	$\Delta H_m$ [J/g]	$\chi$ [%]
<i>Neat PLA</i>						
0	59.95	104.14	25.29	144.71	26.24	1.02
<i>Hemp shive-based composites</i>						
5	59.28	107.21	21.08	145.59	22.51	1.64
10	60.17	106.59	22.28	145.50	23.18	1.10
15	59.39	106.12	22.10	144.99	23.01	1.19
20	59.82	106.08	20.61	145.06	21.54	1.31
25	59.60	105.53	17.65	145.03	19.31	2.51
30	59.56	105.40	17.90	144.92	19.03	1.85
<i>Kenaf bast-based composites</i>						
10	59.35	104.83	22.34	144.74	23.47	1.39
15	59.83	106.09	21.38	145.02	22.34	1.26
20	59.49	106.05	18.05	145.21	19.76	2.42
25	59.55	107.22	17.09	145.60	18.58	2.28
30	60.11	108.67	14.62	146.19	16.22	2.65
35	60.64	109.35	13.78	146.46	15.42	2.97

To evaluate the changes in the viscoelastic properties of the neat PLA and composite systems, dynamic mechanical thermal analysis (DMTA) was performed using a Triton Technology Tritec 2000 DMA. The samples (30×10×3 mm<sup>3</sup> rectangular bars) were heated from room temperature to 105°C at a heating rate of 2°C/min in an air atmosphere. The storage modulus ( $E'$ ) and the loss factor ( $\tan\delta$ ) were measured as a function of the temperature in the linear regime, which was previously evaluated for each composition through preliminary oscillatory tests. The measurements were run in a single cantilever bending mode at an oscillatory amplitude of 0.02 mm and a frequency of 1 Hz.

The typical outcome of this testing protocol is shown in Figure 5.3 for neat PLA.

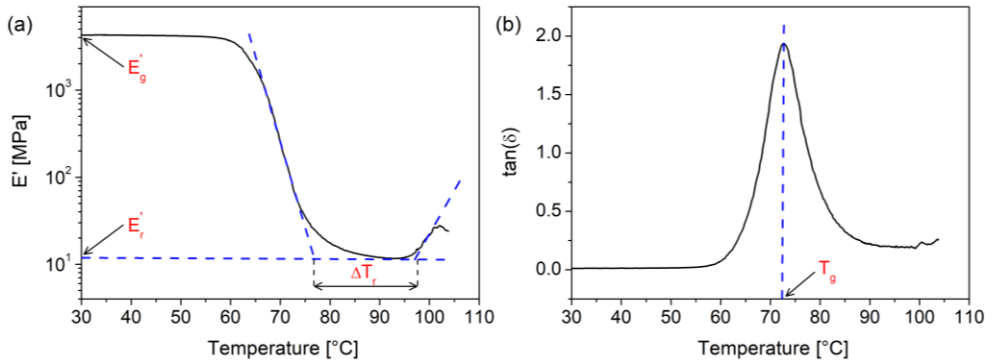


**Figure 5.3** Evolution of elastic modulus  $E'$  (a) and loss factor  $\tan(\delta)$  (b) with temperature for neat PLA.

At low temperatures, where the polymer is "frozen" in a non-equilibrium state and polymeric chains are mostly unable to move, the glassy region develops. The glassy modulus ( $E'_g$ ), identified as the plateau value of  $E'$  at low temperature, assumes a value close to  $4.5 \cdot 10^3$  MPa for the neat PLA. A sharp descent of  $E'$  takes place around  $60^\circ\text{C}$ , where the glass transition region is centred. The glass transition temperature ( $T_g$ ) was identified as the peak of the loss factor. Subsequently, the rubbery region develops, which can be very short or even absent for low-molecular-weight PLA. In this region, all the amorphous phase has undergone the glassy-rubbery transition, and the polymeric chains have sufficient mobility to develop crystalline regions. A sudden increase of  $E'$  modulus, between  $95^\circ\text{C}$  and  $110^\circ\text{C}$ , indicates the cold crystallization of the PLA causing an increase in polymer rigidity. As the temperature increases, the thermal energy provided to the material is indeed enough to let part of the polymer chains rearrange from an amorphous form to a crystalline form. Two important parameters were identified in the rubbery region: the rubbery modulus ( $E'_r$ ) and the length of the rubbery plateau ( $\Delta T_r$ ). The first, equal to the minimum module value in the rubbery region, describes the behaviour of the materials above  $T_g$ . The second, equal to the length of the temperature range between the offset temperature of the glass transition region and the onset temperature of the cold crystallization region, depends on the PLA molecular weight. The latter can be considered as a gauge for the PLA level degradation in

decomposition studies [120]. The temperature dependence of the elastic modulus and loss factor is reported in Figure 5.4 for both composite systems.

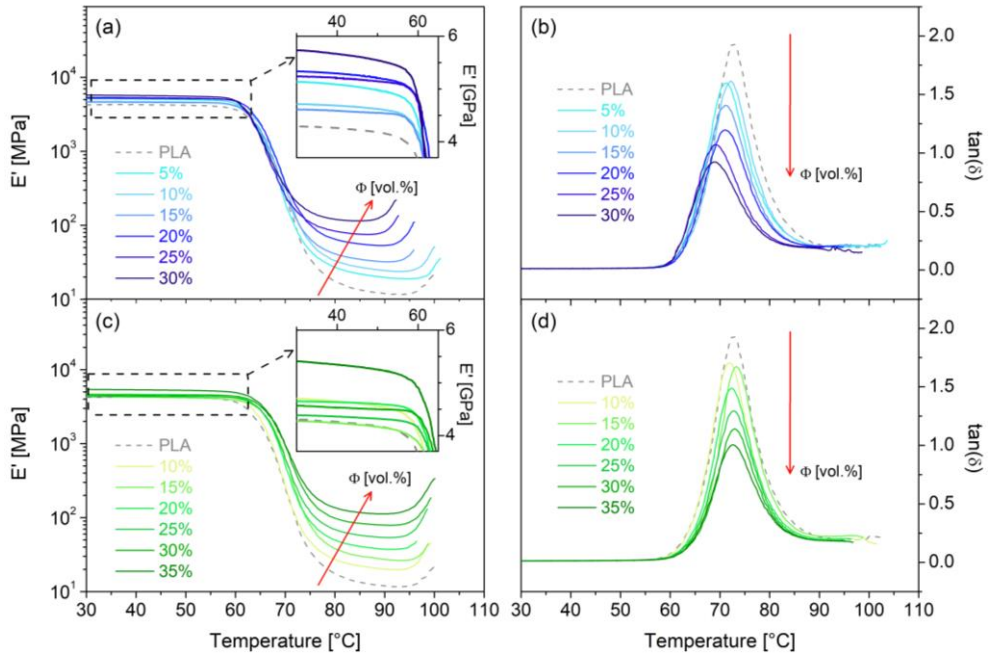


**Figure 5.4** Temperature dependence of the elastic modulus,  $E'$ , and loss factor,  $\tan(\delta)$ , for hemp shives (a, b) and kenaf bast (c, d) based composites at different volumetric fibre content after processing. The dashed line represents the variation of  $E'$  and  $\tan(\delta)$  for the neat PLA.

At low temperatures, the glassy modulus shows a non-monotonous increase in the fibre content (inset in Figure 5.4a, c). Generally, one would expect that increased filler content strengthens the PLA-based composite resulting in higher  $E'$  values. However, the glassy modulus of a composite material depends not only on the fibre loading but also on (i) the quality of the fibre-matrix interaction and (ii) on the polymeric matrix crystallinity [121] [122]. A sharp descent of  $E'$  takes place around  $60^\circ\text{C}$  and identified the glass transition region. The glass transition temperature of the natural fibre-based composites was measured as the  $\tan(\delta)$  peak and the results are reported in Table 5.4. As expected, due to the difference between the two measurement techniques, the temperature related to the glass-rubber relaxation is higher than the calorimetric glass transition temperature. The  $T_g$  negligible

variation with the fibre content is correlated to concurrent events that occur in opposite directions in the glass transition phase and the particular morphology of PLA [120]. As a result of increasing the polymeric matrix crystallinity with the fibre content (Table 5.1), the  $\tan(\delta)$  peak amplitude shows a decrease as the filler quantity augments. As the crystalline phase becomes more important, the stiff framework within the material arrests the segmental motion of the polymer, and the samples gain dimensional stability [123] [124]. The increased rigidity of the polymer is reflected in the  $E'$  value which results in lower  $\tan(\delta)$  values. Above the glass transition phase, the rubbery region develops where the increase in the fibre content results in a growth of the rubbery modulus and a small reduction of the rubbery plateau length. The latter could suggest that the manufacturing process of the green composites affects the amorphous regions favouring the formation of shorter chains that crystallize at lower temperatures since the mobility is enhanced by the availability of more free volume [125] [113] [113]. However, SEC analyses (Table 5.2) detected negligible degradation of green composites during the manufacturing process.

**Table 5.4** Calorimetric (from first heating scan) and viscoelastic parameters related to the glass transition relaxation of hemp shive and kenaf bast-based composites at different volumetric fibre content compared to the neat PLA.

$\Phi$ [ vol.% ]	$T_g$ (DSC) [°C]	$T_g$ (DMA) [°C]
<i>Neat PLA</i>		
0	61.41	72.70
<i>Hemp shive-based composites</i>		
5	60.72	71.40
10	61.39	72.26
15	60.54	71.03
20	60.96	71.08
25	61.09	69.19
30	59.78	69.08
<i>Kenaf bast-based composites</i>		
10	60.71	71.61
15	61.93	73.28
20	61.70	72.50
25	61.22	72.68
30	61.29	72.88
35	60.66	72.60

### 5.3 Degradation phenomena in the melt state

The first step in the study of the natural fibre effect on polylactic acid degradation was to evaluate the degradation phenomena over time of the samples in the melt state through rheological analysis. The latter represents a powerful means of investigation to determine degradation kinetics as viscosity strongly depends on molecular weight distribution [126] [127] [128]. In detail, sequences of small amplitude oscillatory shear tests were carried out to monitor the degradation kinetic of composites loaded with micrometric natural fibres (testing conditions are reported in Chapter 4, Section 4.3). Figure 5.5 reports the results of the consecutive frequency scan on the same sample for the neat matrix and the composites at  $\Phi = 10$  vol.% of hemp shives and kenaf bast fibres.

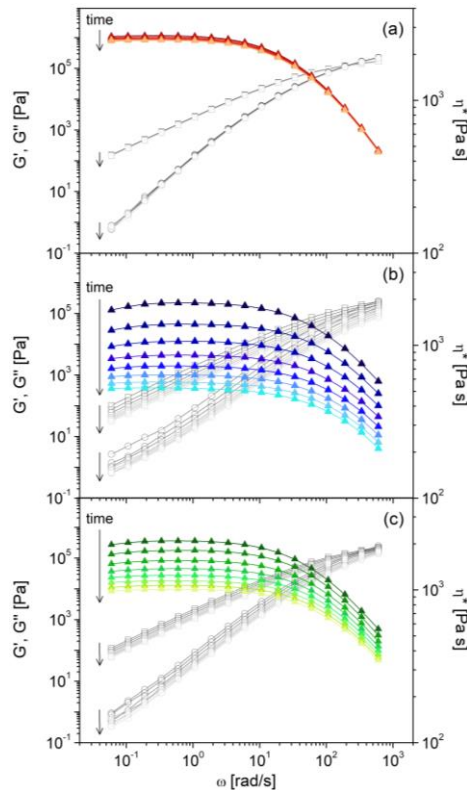


**Figure 5.5** Complex viscosity decrease (full triangles) as collected through consecutive frequency scans over  $\sim 2$  h for pure PLA (a) and hemp shive (b) and kenaf bast (c) based composites at 10 vol.% of fibres. The elastic and viscous moduli are reported as grey squares and circles, respectively.

The shear moduli ( $G'$ ,  $G''$ ) and the complex viscosity ( $\eta^*$ ) progressively decrease while testing. The reduction is more pronounced for the composite, meaning that the fibres promote matrix degradation. The zero-shear complex viscosity ( $\eta_0^*$ ), i.e., the material viscosity when it is effectively at rest, is correlated to the weight-average molecular weight ( $M_w$ ) of a polymer by the following equation:

$$\eta_0^* = k (M_w)^{3.4} \quad (5.2)$$

where  $k$  is a constant that is specific to the polymer being assessed [116]. This relationship demonstrates that slight variations in molecular weight led to great variations in melt viscosity when this viscosity is determined at a very low shear rate. Therefore, the time evolution of the zero-shear complex viscosity can be taken as a reference to monitor the degradation advancement [83].

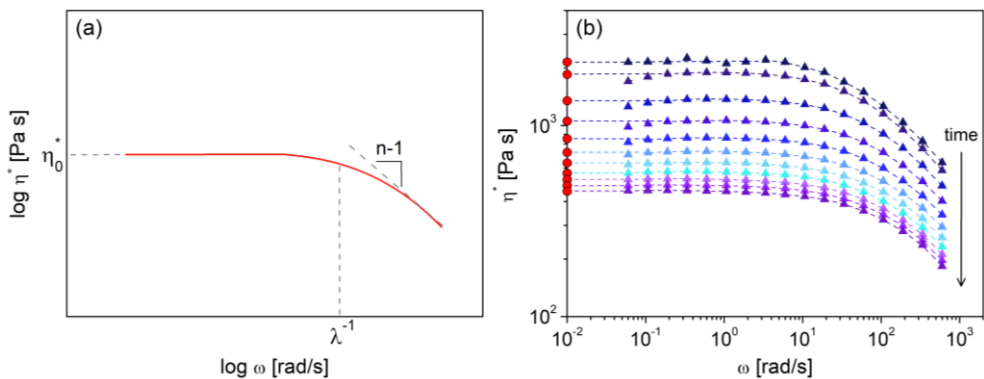


**Figure 5.6** (a) Graphical description of the parameters of Equation (5.3). (b) Decrease of the complex viscosity collected through consecutive frequency scans for hemp shive-based composites at 10 vol.%. The red circles represent the extrapolated zero-frequency complex viscosity over time.

The simple testing procedure based on consecutive frequency scans allows obtaining the  $\eta_0^*$  variation over time by identifying the low-frequency plateau of the complex viscosity. The extrapolation procedure is shown in Figure 5.6, where the frequency dependence of the  $\eta^*$  is reported for composite at 10 vol.% of hemp shives.

To identify the zero-shear viscosity, the following model was fitted to the experimental data (5.3):

$$\eta^*(\omega) = \frac{\eta_0^*}{(1 + \lambda \omega)^{1-n}} \quad (5.3)$$

Equation (5.3) is a simple Carreau-like equation, where  $\eta_0^*$  is the zero-shear viscosity;  $\lambda$  represents the main polymer relaxation time;  $n$ , generally known as “flow index”, quantifies the non-Newtonian feature of the polymer. The graphical description of these parameters is reported in Figure 5.6a. The development of a continuous fibre network in the polymeric matrix results in a deviation of the complex viscosity trend from that predicted by Equation 5.3. The frequency dependence of the complex viscosity at time-zero,  $\eta^*(0)$ , is reported in Figure 5.7 for the composite systems at different fibre loading.

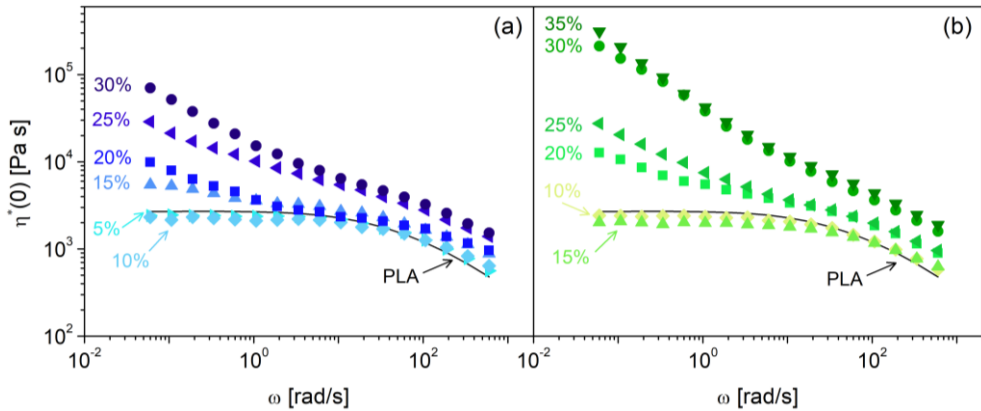


**Figure 5.7** Frequency dependence of the complex viscosity ( $\eta^*$ ) at time-zero of the PLA-based composites filled with hemp shives (a) and kenaf bast fibres (b) at different volumetric fibre loadings. The solid line represents the variation of moduli for the neat PLA.

The  $\eta^*(0)$  values were obtained by combining the elastic and viscous moduli at time-zero extrapolated in the previous chapter (see Chapter 4 Section 4.2) according to the following equation:

$$\eta^*(0) = \frac{\sqrt{(G'(0))^2 + (G''(0))^2}}{\omega} \quad (5.4)$$

The presence of natural fibres in the polymer reduces the effective gap distance available for the polymeric matrix between the particles by an amount proportional to the filler content. Consequently, an increase in the matrix deformation rate in the gap between the particles is recorded at high frequency, that is when the polymer governs the rheological response. This hydrodynamic effect is expressed in a vertical shift of the complex viscosity at high frequencies (Figure 5.7).

The zero-shear viscosity extrapolation requires the identification of amplification factors,  $B(\Phi)$  to consider the hydrodynamic effect. These factors, defined as the ratio between the complex modulus of the filled sample and that of the neat matrix in the high-frequency region, have already been identified in Chapter 4 Section 4.3 for the network elasticity extrapolation. The normalization of the complex viscosity with respect to  $B(\Phi)$  is shown in Figure 5.8 for both composite systems. An evident deviation of the plateau of  $\eta^*$  at low frequency is observed at  $\Phi \geq 15\%$  and  $\Phi \geq 20\%$  for hemp shive and kenaf bast-based composites respectively (Figure 5.8). This rheological behaviour is related to the formation of a continuous fibre network at  $\Phi \geq \Phi_c$ , as reported in Chapter 4 (Section 4.3). In detail, below  $\Phi_c$ , the rheological response is essentially Newtonian as a direct consequence of the relaxed state of PLA in the whole range of investigated frequencies. Above  $\Phi_c$ , the arrest of the relaxation dynamics in composites causes an asymptotic rise of the complex viscosity at low frequencies. Consequently, the strong percolating effects deviate  $\eta^*$  trend from that provided by the Carreau-like equation not allowing the identification of  $\eta_0^*$ .

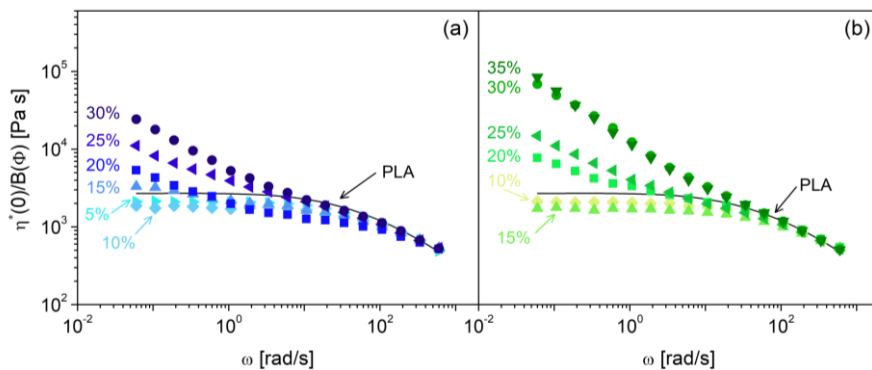


**Figure 5.8** Frequency dependence of the complex viscosity ( $\eta^*$ ) at time-zero divided by the amplification factor for hemp shive (a) and kenaf bast (b) based composites at different volumetric fibre loadings. The solid line represents the complex modulus for the neat PLA.

The time evolution of the zero-shear complex viscosity is addressed below for the composites at  $\Phi < \Phi_c$ . The analysed systems showed different values of  $\eta_0^*(t)$  for  $t \rightarrow 0$ , i.e., when the degradation process caused by rheological measures has not yet started. This rheological behaviour is the result of (i) the degradative effects of the fibres on the polymeric matrix during the manufacturing process of the green composites; (ii) a non-negligible increase of the viscoelastic functions with respect to the pure matrix because of the hydrodynamic interactions among the fibres [129]. Therefore,  $\eta_0^*(t)$  was normalized with respect to its initial value to facilitate the comparison (Figure 5.9).

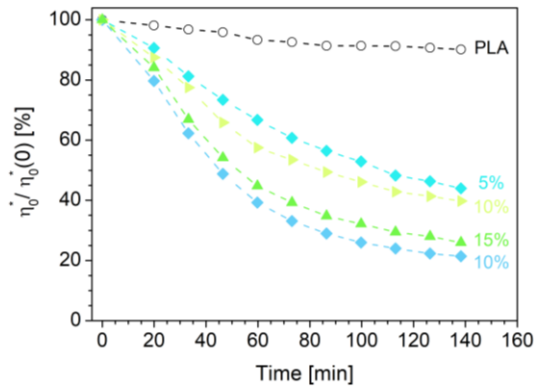
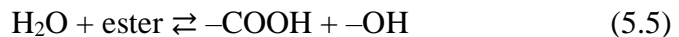


**Figure 5.9** Time evolution of the zero-frequency complex viscosity ( $\eta_0^*$ ) normalized with respect to the initial value ( $\eta_0^*(0)$ ) for neat PLA and green composites at  $\Phi < \Phi_c$ . Lines are guide for the eye.

The pro-degradative effect of the fibres is obvious: the higher the  $\Phi$ , the faster and more significant the drop of  $\eta_0^*$ . The strong degradation of the green composites can be explained by the presence of water molecules bound to hydroxyl groups of natural fibres which trigger the hydrolytic degradation of PLA [130]. From a chemical point of view, at the temperature considered ( $T=180^\circ\text{C}$ ), hydrolytic degradation is indeed the predominant degradation mechanism [131] [132]. In detail, the water molecules hydrolyse the ester bonds along the backbone of the PLA chain causing a chain cleavage reaction, according to the following reaction:



In addition, the results revealed that the degradation process depends on the natural fibre type. The hemp shives have a higher degradative effect than the kenaf bast fibres with the same fibre content. This behaviour can be related to the higher absorption capacity of the hemp shive fibre. Isothermal tests carried out at  $T=110^{\circ}\text{C}$  on water-saturated fibres revealed different water content of 20 wt.% (see Figure 3.1 in Chapter 3). The greater absorbency of the hemp shives can be attributed to the higher content of hemicellulose which is the element responsible for moisture absorption [12].

## **5.4 Hydrolytic degradation of PLA-based composites in water environment**

Hydrolytic degradation is a complex mechanism dependent on the interaction of living organisms with biodegradable polymers (e.g., polysaccharides, polyesters, and polyamides). The latter can be subject to different degradation mechanisms, such as thermal, mechanical, or chemical degradation, which can act alone or in combination [133]. However, hydrolysis of susceptible chemical bonds is the most important degradation mechanism of all, leading to chain scission and a decrease in molecular weight [134] [135] [136]. Environmental characteristics strongly affect the kinetics of the process, which is slow when it occurs in air or water at neutral pH. Acid, base, or enzyme catalysis is thus required to accelerate the first stage of degradation of biodegradable polymers. Further factors influencing the rate of hydrolytic degradation are parameters related to polymer characteristics such as polymer chain length, crystallinity, molecular weight distribution, sample shape, porosity, processing conditions, and the diffusivity of water in the polymer matrix [137] [17] [138] [105]. Central to the comprehension of these hydrolytic degradation processes, is an understanding of water fluxes in these systems. An increase in the crystallinity degree lowers the rate of degradation since water penetrates hardly into the highly ordered crystalline regions of polymers [139]. Furthermore, the relative rates of hydrolysis and water diffusion in each polymer control the hydrolytic degradation mechanism which can occur through a surface or bulk process. Therefore, for both of these processes, an understanding of water flux in polymers is important. The different erosion mechanisms following hydrolysis have been described by Viera et al. [133]. It should be noted that the term “degradation” in this case specifically refers to the polymer chain scission reaction, whereas “erosion” refers to the loss of polymer material as oligomers and monomers leave the

polymer [140]. Surface erosion involves a thickness reduction with a loss of material from the surface and occurs when the rate of hydrolysis exceeds the rate of diffusion of water into the bulk. This process can be due to the hydrophobicity of the polymer, a high glass transition temperature, a high crystallinity degree, and/or a very rapid hydrolysis rate [141]. Bulk erosion involves uniform degradation through the thickness and occurs when the hydrolysis rate is lower than the water diffusion rate. The bulk process is the dominant mechanism for polyesters such as PLA. The simplest case of mass erosion occurs when the diffusion speed of the hydrolytic catalyst (e.g., degradation products) is faster than the reaction speed. In this case, the degradation will occur uniformly through the thickness, with hydrolytic chain scissions. In this case, the degradation will occur uniformly through the thickness, with hydrolytic chain scissions. Typically, during bulk erosion, a decrease in the molecular weight of the polymer occurs before any mass loss is observed. The more complex situation, where bulk erosion occurs with autocatalysis leading to the formation of pores due to loss of the degraded material, typically occurs only after extensive degradation. In this case, the accumulation of oligomers with acidic end groups that diffuse more slowly out of the polymer than water leads to higher local acidity internally, resulting in heterogeneous degradation [142] [143]. However, if the thickness of the polymer is sufficiently small and the degradation products diffuse rapidly, then autocatalysis is largely suppressed [144]. Overall, it should also be noted that surface or bulk erosion modes are two extremes of the degradation process, and the erosion of a polymer usually shows characteristics of both.

For most biodegradable materials, especially synthetic polymers like PLA, biodegradation is considered to consist of a sequential mechanism. The first step is hydrolytic degradation which reduces the molecular weight as a result of the hydrolysis of the ester bonds along the backbone of the PLA chain (Reaction 5.5). In detail, water molecules penetrate the polymer triggering hydrolytic degradation and converting very long polymer chains into shorter water-soluble fragments [145]. Only when PLA molecular weight reaches 10000 Da or less, the second step can start in which the microorganisms assimilate the small molecules produced [146]. For this reason, the knowledge of hydrolytic degradation is of fundamental importance to fully understand the biodegradation process of PLA and its composites. In this study, hydrolytic degradation tests were performed on  $30 \times 10 \times 3 \text{ mm}^3$  rectangular bars dipped in test tubes containing 50 mL of water at pH 7.5. The test tubes were located in a shaker incubator (Bormarc Shaker SKI 4) at  $T=45^\circ\text{C}$  and an agitation speed of 150 RPM. A test

temperature lower than the PLA glass transition temperature ( $T_g=60^\circ\text{C}$ ) was set to evaluate the sample hydrolytic degradation in very mild conditions. At selected periods, specimens were removed from the water and dried under vacuum at  $30^\circ\text{C}$  for about 8 days and then at  $50^\circ\text{C}$  until constant weight. This slow drying cycle was adopted to avoid changes in the materials during the drying phase. To evaluate the hydrolytic degradation rate of the green composites, different analyses were conducted on the samples before and after the water soaking. Differential Scanning Calorimetry (DSC) and Dynamic Mechanical Thermal Analysis (DMTA) experiments were used to monitor the extent of degradation by understanding the role of the natural fibres on the matrix degradation. Furthermore, the average molecular weight evolution was estimated by Size Exclusion Chromatography (SEC) analyses to validate the suitability of thermal analysis techniques for monitoring PLA degradation.

Differential Scanning Calorimetry was performed to evaluate the hydrolytic degradation effects on the thermal properties of the green composites. In detail, the analyses were carried out under the same conditions indicated in Section 5.2 and the first heating scan was considered to assess the hydrolytic degradation effect on samples as it represents the current status of the materials. The DSC thermograms and data of the samples after 50 days of water soaking are shown in Figure 5.10 and Table 5.5 respectively.

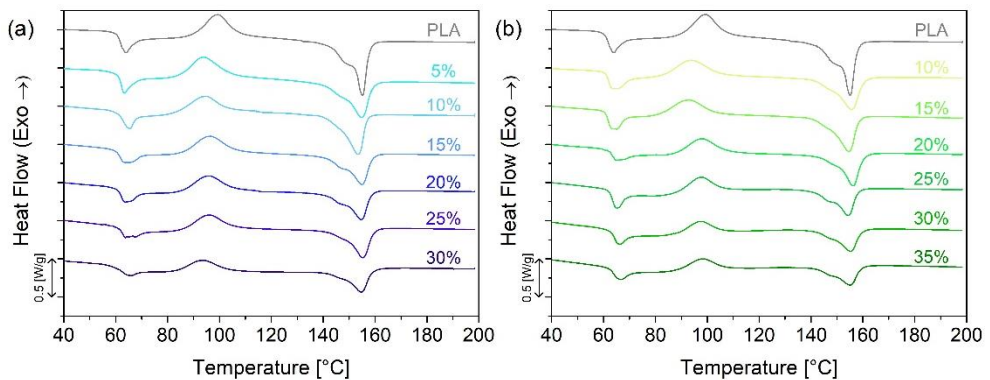


**Figure 5.10** DSC thermograms of hemp shive (a) and kenaf bast (b) based composites at different volumetric fibre content after 50 days of water soaking, first heating scan.

**Table 5.5** DSC data on hemp shive and kenaf bast-based composites at different volumetric fibre content compared to the neat PLA after 50 days of water soaking by first heating curves.

$\Phi$ [vol.%]	$T_g$ [°C]	$T'_{cc}$ [°C]	$\Delta H_{cc}$ [J/g]	$T'_m$ [°C]	$\Delta H_m$ [J/g]	$\chi$ [%]
<i>Neat PLA</i>						
0	62.08	89.91	23.49	142.40	32.12	9.28
<i>Hemp shive-based composites</i>						
5	62.25	84.47	23.43	140.06	28.80	6.15
10	62.68	82.49	23.43	139.73	26.64	3.92
15	61.94	85.98	22.17	140.72	24.43	2.95
20	62.32	85.49	19.65	140.73	20.77	1.57
25	62.83	85.70	18.09	141.40	20.65	3.87
30	62.60	83.61	12.86	140.87	16.39	5.78
<i>Kenaf bast-based composites</i>						
10	62.08	83.36	21.65	141.05	26.73	6.23
15	61.89	81.52	20.92	140.27	24.29	4.43
20	62.97	87.75	19.17	141.54	21.31	3.03
25	63.69	87.55	16.23	140.95	19.89	5.60
30	64.34	87.91	11.18	141.37	16.19	8.31
35	64.08	88.26	10.91	142.13	14.81	7.05

The samples after 50 days of water soaking (Figure 5.10) show the same thermal transitions along the increasing temperature axis compared to the materials immediately after processing (Figure 5.1): glass transition (between 50°C and 70°C), cold crystallization (between 80°C and 120°C) and, melting process (between 135°C and 160°C). The variation of the thermal properties after 50 days of water immersion was analysed for both composite systems to evaluate the hydrolytic degradation process effect on natural fibre-based composites (from Figure 5.11 to Figure 5.15). The first thermal transition along the increasing temperature axis is the glass transition. The DSC thermograms in Figure 5.10 show the same structural relaxation endothermic peaks recorded before the hydrolytic degradation test (Figure 5.1). The glass transition temperature variation, which describes the thermal behaviour in this region, is reported in Figure 5.11. The results show a slight increase of  $T_g$  at high fibre contents which can be ascribed to

the effect of the natural fibres on the amorphous chains during the hydrolytic degradation process. Nevertheless, these variations can be considered irrelevant as they are less than 10% after 50 days of water soaking. This result is due to the glass transition temperature being sensitive to large-scale morphological changes.

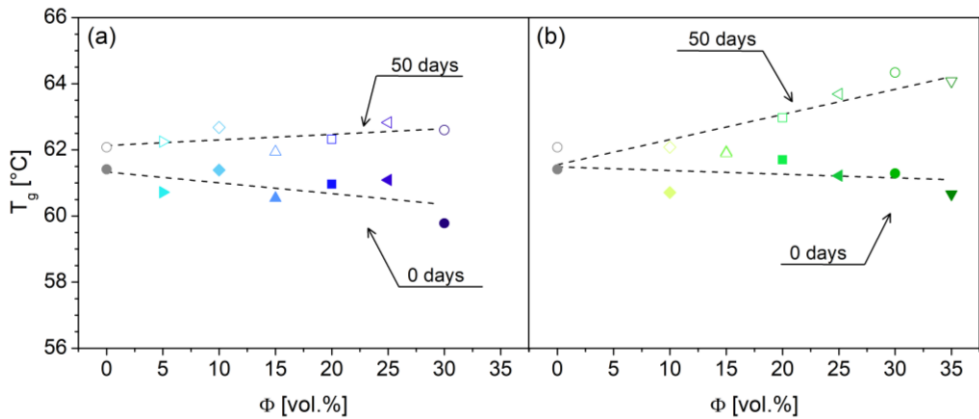


**Figure 5.11** Glass transition temperature of hemp shive (a) and kenaf bast (b) based composites at different volumetric fibre content before (full symbols) and after 50 days (empty symbols) of water soaking. The lines are guides for the eye.

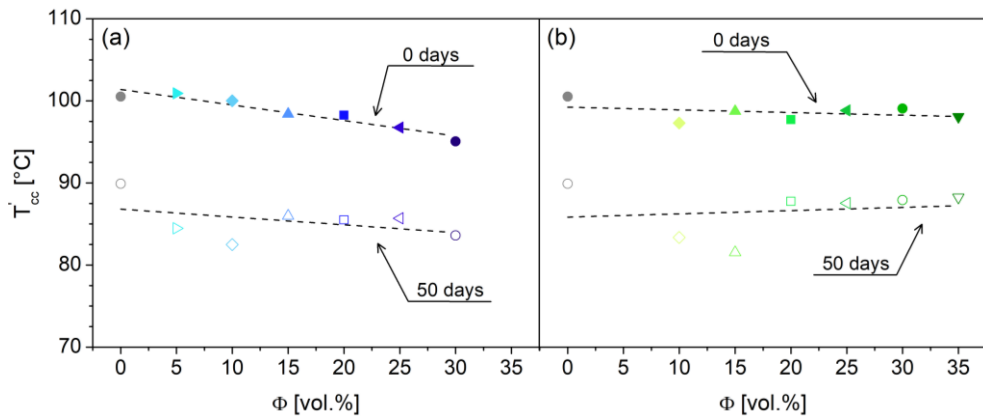


**Figure 5.12** The onset temperature of the cold crystallization exotherm peak of hemp shive (a) and kenaf bast (b) based composites at different volumetric fibre content before (full symbols) and after 50 days (empty symbols) of water soaking. The lines are guides for the eye.

When the glass transition is overcome, the cold crystallization process starts. An important variation in the onset temperature of the exotherm peak was observed after the hydrolytic degradation test (Figure 5.12). In detail,  $T'_{cc}$  shows a decrease of  $13.2 \pm 2.7$  °C and  $12.0 \pm 2.7$  °C for hemp shive and kenaf bast-based composites respectively. This relevant variation highlights that the hydrolytic degradation process causes the formation of polymeric chains able to cold crystallize at lower temperatures. The enthalpy of cold crystallization, on the other hand, shows no change suggesting that the degradation process did not cause an increase in the number of chains involved in cold crystallization.

The last thermal transition is the melting process which shows interesting changes in the samples after 50 days of water soaking. In detail, the onset temperature of the melting endotherm peak takes on an approximately constant value for all the samples due to an increase in  $T'_m$  for high-fibre composites (Figure 5.13). Regarding the melting enthalpy, the peak area shows a decrease at  $\Phi \leq 10$  vol.% and  $\Phi \leq 15$  vol.% for hemp shive and kenaf bast-based composites respectively, and an increase for samples at the higher volumetric fibre content (Figure 5.14). According to Chapter 4, where the percolation threshold was identified, the trend variation occurs when the percolation threshold is overcome. Melting enthalpy variation has direct effects on the crystallinity degree of green composites.

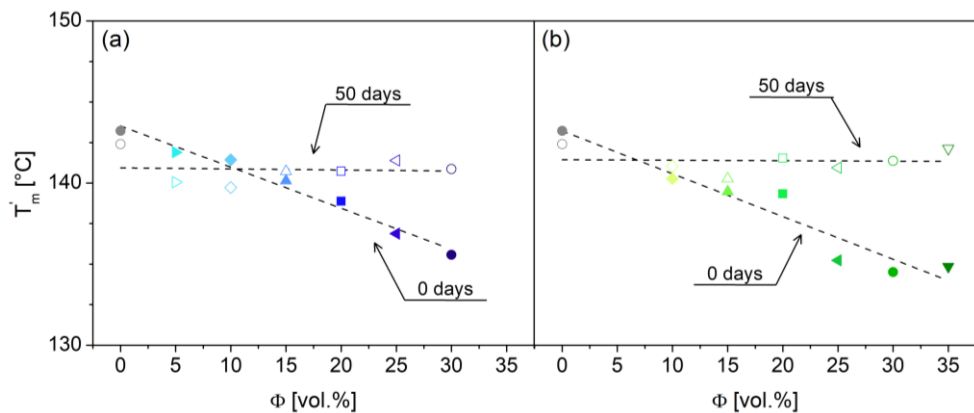


**Figure 5.13** The onset temperature of the melting endotherm peak of hemp shive (a) and kenaf bast (b) based composites at different volumetric fibre content before (full symbols) and after 50 days (empty symbols) of water soaking. The lines are guides for the eye.

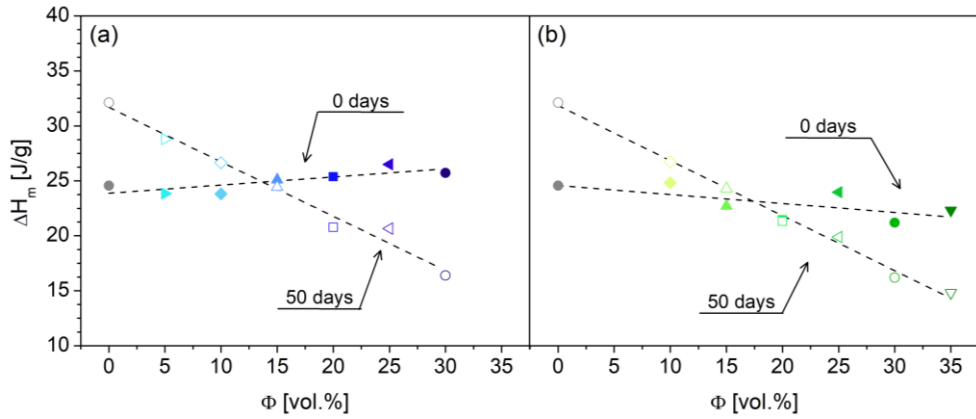


**Figure 5.14** The melting enthalpy of hemp shive (a) and kenaf bast (b) based composites at different volumetric fibre content before (full symbols) and after 50 days (empty symbols) of water soaking. The lines are guides for the eye.

Figure 5.15 report the crystallinity degree values of the green composite systems before and after the hydrolytic degradation test.

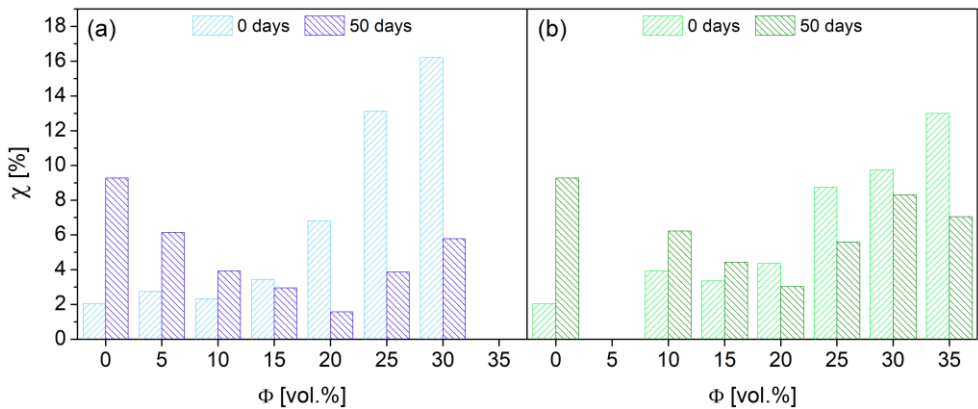


**Figure 5.15** Matrix crystallization degree of hemp shive (a) and kenaf bast (b) based composites at different volumetric fibre content before and after 50 days of water soaking.

According to the melting enthalpy variation at the percolation threshold and considering the non-variation of the cold crystallization enthalpy after the water immersion, the crystallinity degree shows an increase at  $\Phi < \Phi_c$  and

a decrease at  $\Phi > \Phi_c$ . This result can be explained by a higher hydrolytic degradation rate of the polymeric matrix in presence of a natural fiber continuous network. The hydrolytic degradation process of PLA is indeed a two-stage mechanism [147]. In the first stage, random hydrolytic scission of ester bonds proceeds with the diffusion of water molecules into the amorphous regions. An increase in the crystallinity degree is observed in this phase. The  $\chi$  increase is caused, at short times, by the change of some amorphous regions into crystals and then by the effect of the erosion of the amorphous parts. In the second stage, also the crystalline regions undergo hydrolysis with a hydrolytic attack which occurs from the edge toward the centre of the crystalline domains [32] [31]. The crystallinity degree decrease of the composites above the percolation threshold can be related to the trigger of hydrolytic degradation in the crystalline domains after 50 days of water immersion (Figure 5.15). Therefore, the formation of a natural fibre continuous network into the polymeric matrix produces an increase in the hydrolytic degradation rate.

To evaluate the hydrolytic degradation effects on the viscoelastic properties of the neat PLA and its composites, dynamic mechanical thermal analyses were performed. In detail, the analyses were carried out under the same conditions indicated in Section 5.2, and the variation of the elastic modulus and loss factor was monitored at 0, 10, 20, 30, and 50 days of water soaking.

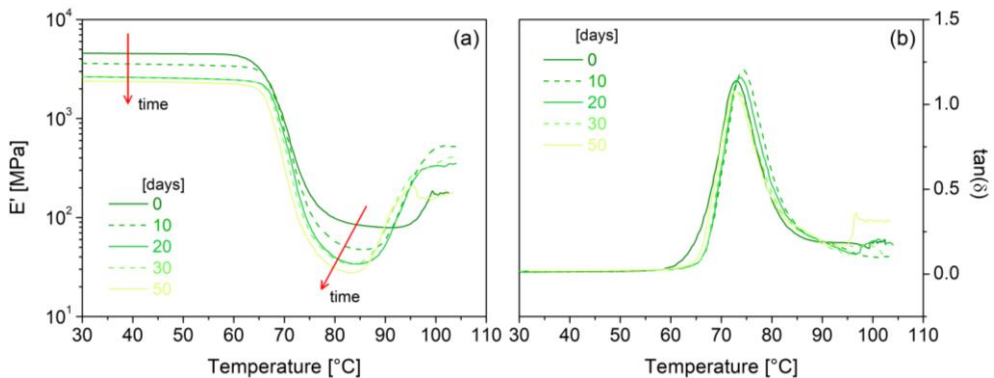


**Figure 5.16** Temperature dependence of the elastic modulus (a), and loss factor (b) for composite filled with 30 vol.% kenaf bast fibres after 0, 10, 20, 30, and 50 days of water soaking.

Figure 5.16 reports the typical trend of the elastic modulus and loss factor as the immersion time progresses for the composite at  $\Phi = 30$  vol.% kenaf bast fibres. The results show that the glassy and rubbery modulus ( $E'_g$ ,  $E'_r$ ) and the length of the rubbery plateau ( $\Delta T_r$ ) progressively decrease while testing. No significant change, however, was observed for the glass transition temperature ( $T_g$ ), identified as the peak of the loss factor, as it is sensitive to large-scale morphological changes.

To assess the natural fibre effect on the elastic modulus below the glass transition temperature, the glassy modulus variation at different immersion times was analysed (Figure 5.17). The neat PLA reports an increase in modulus after 10 days of water soaking followed by a decrease for the next few days. In contrast, the composite systems show a marked decrease in  $E'_g$  after only 10 days and achieve a constant value after 50 days. In addition, the more pronounced effect in the case of kenaf bast fibres, probably due to their different fibre/matrix interaction, indicates that fibre type is an important parameter in the process of hydrolytic degradation.

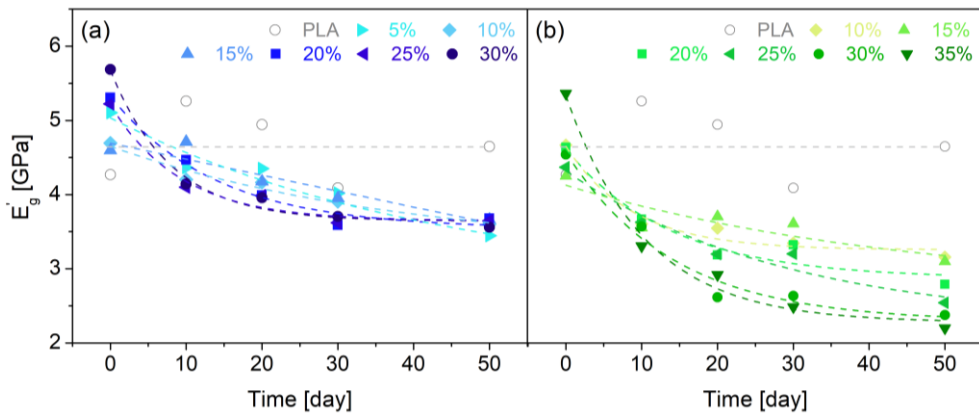


**Figure 5.17** Glassy modulus as a function of immersion time for hemp shive (a) and kenaf bast (b) based composites at different volumetric fibre content. The lines are guides for the eye.

Figure 5.18 reports the glassy modulus of the samples before and after 50 days of water immersion. Before the hydrolytic degradation test begins, the natural fibres reinforce the polymeric matrix ( $E'_g$  increases) while, after 50 days, they cause a marked decrease of the elastic properties ( $E'_g$  decreases).

The glassy modulus variation in composite systems depends not only on the fibre loading but also on (i) the quality of the fibre-matrix interaction and (ii) on the polymeric matrix crystallinity [121] [122]. In detail, good interfacial adhesion and a high crystallinity degree produce better elastic properties. For the samples at  $\Phi < \Phi_c$ , an increase of the crystallinity degree was detected after 50 days of water soaking due to the hydrolytic degradation of the matrix amorphous regions (Figure 5.15). Therefore, the decrease of  $E'_g$  can be correlated to the fibre-matrix debonding for the water effect that worsens the composite properties. On the other hand, for the samples at  $\Phi > \Phi_c$ , the crystallinity degree decreases compared to the zero time (Figure 5.15). Therefore, in this case, the  $E'_g$  reduction is the consequence of the decrease in the quality of the fibre-matrix interaction and the polymeric matrix crystallinity. In the end, for the neat PLA, the absence of the natural fibre and the increase in the crystallinity degree are the cause of the  $E'_g$  increase.

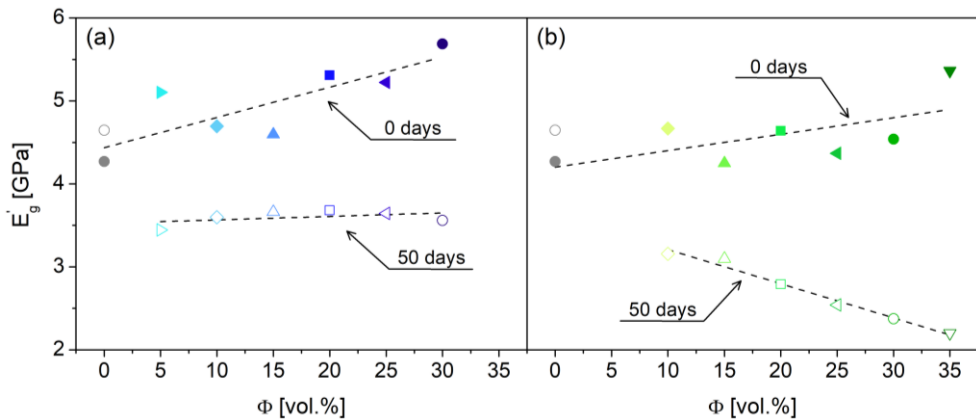


**Figure 5.18** Glassy modulus of hemp shive (a) and kenaf bast (b) based composites at different volumetric fibre content before (full symbols) and after 50 days (empty symbols) of water soaking. The lines are guides for the eye.

The length of the rubbery plateau at different immersion times was analysed in Figure 5.19 for the neat PLA and both the composite systems. The results show a decrease of the  $\Delta T_r$  with the immersion time until to achieve a constant value after 50 days. The rubbery plateau is narrower as samples are more degraded since the cold crystallization starts at lower temperatures. In accordance with the thermal analysis in Figure 5.12, these

results indicate that the effect of hydrolytic degradation on the amorphous regions is forming shorter chains that easily rearrange in spherulites since the mobility is enhanced by the availability of more free volume.

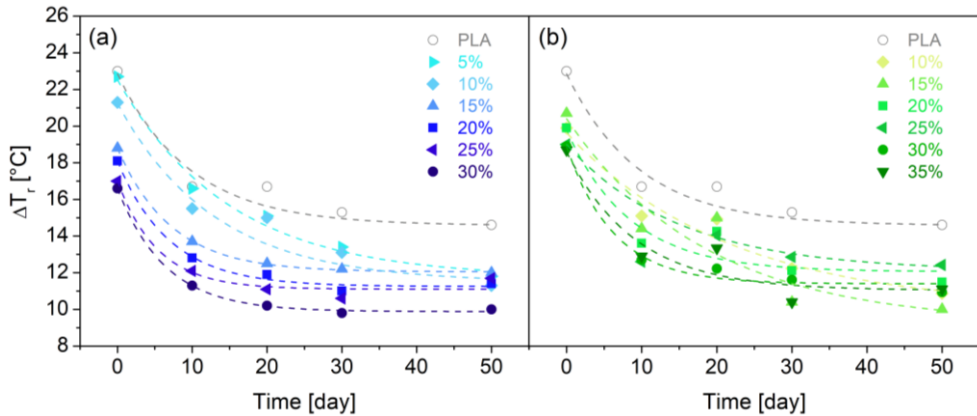


**Figure 5.19** Length of the rubbery plateau as a function of immersion time for hemp shive (a) and kenaf bast (b) based composites at different volumetric fibre content. The lines are guides for the eye.

The rubbery modulus variation at different immersion times was analysed to evaluate the natural fibre effect on the elastic modulus above the glass transition temperature (Figure 5.20). Before the hydrolytic degradation test begins, the natural fibres reinforce the polymeric matrix ( $E_r'$  increases) while, after the water immersion of the samples, they cause a marked decrease of the elastic properties ( $E_r'$  decreases). In detail, the rubbery modulus progressively decreases over time linearly for pure PLA, hemp shives-based composites, and kenaf bast-based composites at  $\Phi \leq 10$  vol.% and exponentially for the kenaf bast-based composites at  $\Phi \geq 15$  vol.%. In addition, after 50 days of immersion in water, kenaf fibres produce a greater reduction in modulus. The variation rate of  $E_r'$  over time can be related to the rate of the hydrolytic degradation process. In particular, the degradation seems to be negligible at low fibre contents (i.e., the rubbery modulus is nearly constant with immersion time), while it becomes relevant at high fibre contents. The variation rate of the rubbery modulus, expressed as  $dE_r'/dt$ , is reported as a function of  $\Phi$  in Figure 5.21. The results confirm that increasing the natural fibre content accelerates the elastic modulus decrease over time to a greater extent for the kenaf bast fibres. In addition, the

influence of the percolation threshold is evident. A clear discontinuity in the  $dE_r'/dt$  trend is observed in correspondence with the range in which  $\Phi_c$  has been identified, i.e., between  $10 \leq \Phi_c \leq 15$  vol.% and  $15 \leq \Phi_c \leq 20$  vol.% for hemp shive and kenaf bast based composite respectively (see Chapter 4). In agreement with the crystallinity degree variation of the green composites after 50 days of water soaking (Figure 5.15), the higher variation rate of the rubbery modulus above the percolation threshold demonstrates that the formation of a continuous network of natural fibres within the PLA polymer matrix favours the hydrolytic degradation process.

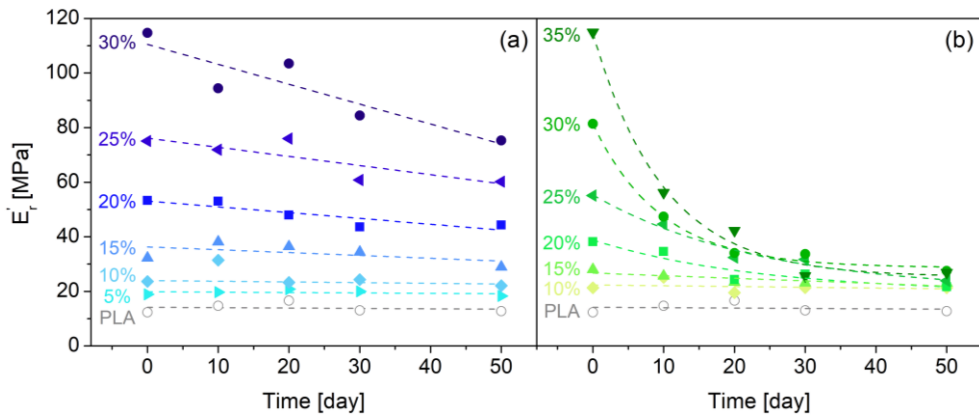


**Figure 5.20** Rubbery modulus as a function of immersion time for hemp shive (a) and kenaf bast (b) based composites at different volumetric fibre content. The lines are guides for the eye.

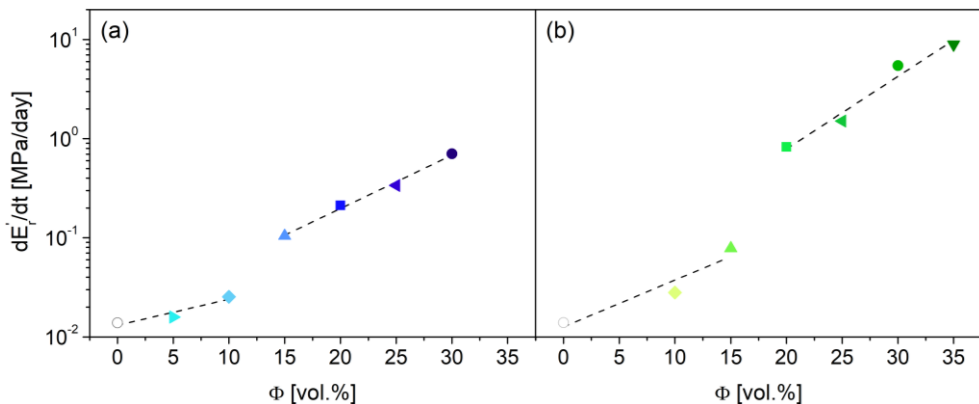


**Figure 5.21** Variation rate of rubbery modulus of hemp shive (a) and kenaf bast (b) based composites at different volumetric fibre content. The lines are guides for the eye.

To assess the hydrolytic degradation entity of the green composites, SEC analyses were performed on the pure PLA and hemp shive-based composites after 50 days of water soaking. The testing conditions are given in Section 5.2. The weight average molar weight ( $M_w$ ), number average molar weight ( $M_n$ ) and polydispersity index ( $PI=M_w/M_n$ ) of the tested samples are reported in Table 5.6 while Figure 5.22 compare the values of  $M_w$  before and after 50 days of water soaking.

**Table 5.6** Weight and number average e molecular weight and polydispersity index of hemp shive-based composites at different volumetric fibre content after 50 days of water soaking.

$\Phi$ [vol.%]	$M_n$ [g/mol]	$M_w$ [g/mol]	PI
0	53300	86000	1.61
5	53000	85000	1.60
10	50400	80900	1.60
15	49700	79600	1.60
20	49100	78900	1.61
25	47800	76600	1.60
30	42600	69650	1.63

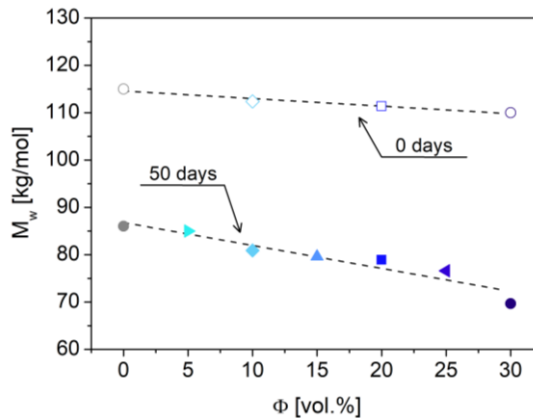


**Figure 5.22** Weight average molecular weight ( $M_w$ ) of hemp shive-based composites at different volumetric fibre content before (empty symbols) and after 50 days (full symbols) of water soaking. The lines are guides for the eye.

A relevant reduction in the PLA molecular weight is observed after the hydrolytic degradation test. The water molecules hydrolysed the ester bonds along the backbone of the PLA chain causing a chain cleavage reaction. The  $M_w$  reduction is more pronounced for the green composites, meaning that the fibres promote matrix degradation. In detail, the natural fibres act as a water vehicle that accelerates matrix hydrolysis.

## **5.5 Characterization of degradation in compost of hemp shive-based composites**

The biodegradation process under real conditions is a complex mechanism to understand and predict. To date, there is no model to predict the lifetimes of any biodegradable polymer given the complexity of real environments such as soil and seawater. Several elements and mechanisms can indeed affect degradation under real conditions [148]. A sequence of steps makes up the biodegradation process. Polymers are initially fragmented into smaller particles and then depolymerized with the formation of oligomers, dimers, and monomers. The depolymerization products are subsequently assimilated by microorganisms and converted to carbon dioxide, nitrogen gas, methane, and water [17]. However, in the natural environment, biotic and abiotic factors frequently act synergistically on biodegradable polymers in a complex interplay of processes and chemistries. The most important aspect concerning biodegradation rates is therefore the direct environment of the polymer. The biodegradation of polyester *in vitro* is obviously going to be very different when compared to the same polymer sample in natural environments. The rate of biodegradation depends on several factors such as moisture content, temperature, pH, availability or otherwise of oxygen, the presence of suitable microbes, etc [149]. All these factors vary in different environments. Given these considerations, the necessity of degradation tests in natural environments is obvious.

To evaluate the effect of the natural fibre on the PLA biodegradation rate in natural environments, degradation tests in compost are performed on the hemp shive-based composites. Homemade mature green compost was used for biodegradation tests and was sieved through a 2 mm mesh to remove coarser particles before use. Three important compost properties were determined before starting the biodegradation tests: the water-holding capacity (WHC), the moisture content, and pH. The first was measured by saturating a compost sample with distilled water, which was then weighed

to derive the saturated weight ( $w_{\text{sat}}$ ). The sample was then dried in a vacuum oven at 110°C to constant weight to determine the dry weight, ( $w_{\text{dry}}$ ). The WHC was calculated according to Equation (5.6). The moisture content was measured by weighting a compost sample before ( $w_i$ ) and after ( $w_f$ ) vacuum drying at 110°C. This parameter was calculated according to Equation (5.7). To determine the pH, a compost sample was mixed with distilled water (1:2), then left at room temperature for 1 h and the pH value of the supernatant was measured with a pH meter. Table 5.7 are reported the results of the compost properties.

$$\text{WHC}(\%) = \frac{w_{\text{sat}} - w_{\text{dry}}}{w_{\text{sat}}} \times 100 \quad (5.6)$$

$$\text{Moisture content}(\%) = \frac{w_i - w_f}{w_i} \times 100 \quad (5.7)$$

**Table 5.7** Water holding capacity, moisture content and pH of the homemade mature green compost.

<b>Compost properties</b>	<b>Values</b>
WHC [%]	80
Moisture content [%]	55
pH	6.6

Neat PLA matrix and hemp shive-based composites with different fibre content were cut in samples of 2.5x1.2x0.3 cm and buried in cylindrical plastic boxes (*diameter 8 cm and height 16 cm*) containing compost to a depth of about 7 cm and incubated at 55°C and 22% relative humidity. Containers were weighed three times a week and water loss through evaporation was adjusted by the water addition. At selected buried periods, specimens were removed from the compost and cleaned with paper towels. Visual inspection, Differential Scanning Calorimetry (DSC), and Size Exclusion Chromatography (SEC) analyses were used to monitor the extent of degradation by understanding the role of the natural fibres on the matrix degradation. The test conditions of DSC and SEC analyses are the same as reported in Section 5.2.

The samples were removed periodically and subjected to visual inspection to evaluate the physical changes of the neat PLA and hemp shive-based composites with different fibre content buried in compost. Light

microscopy images of the surface of filled and unfilled samples at different buried times in compost are reported in Figure 5.23. Neat PLA and green composites show the same surface morphology before burial (Figure 5.23a). A polymer layer covers the surface and an evident texture generated by the contact of the molten polymer with the Teflon sheet during the hot moulding process is observed. A certain level of superficial erosion is observed in filled samples after 10 days in compost as pointed out by the disappearance of the initial texture and the appearance of micro-holes and natural fibres (Figure 5.23b). The neat PLA surface shows an evident erosion only after 40 days in compost while the green composites show a more advanced erosion state (Figure 5.23c).

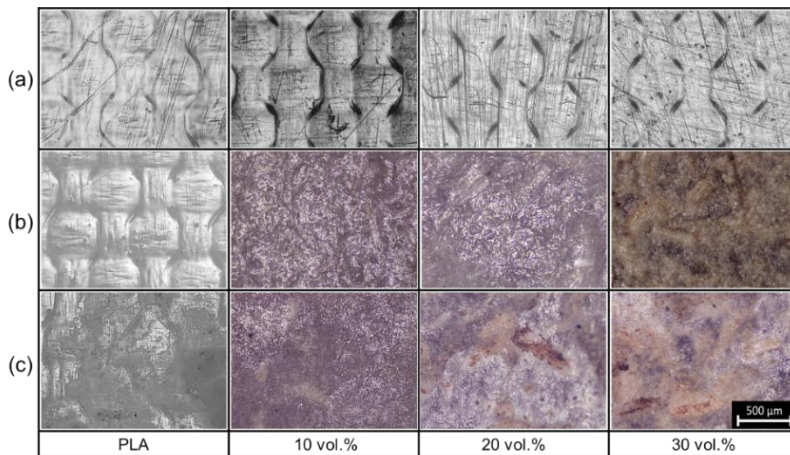


**Figure 5.23** Light microscopy of the surface of neat PLA and hemp shive-based composites at 10, 20, and 30 vol.% unburied (a) and buried in compost at 55°C for (b) 10 and (c) 40 days. The scale bar represents 500 µm.

Figure 5.24 reports the degradation evolution of neat PLA and green composites during composting exposure inspected by a digital camera. PLA matrix shows a rapid transition from transparent to opaque against degradation time in all the samples. The opacity is a degradation consequence and can be correlated to different phenomena such as light scattering due to the presence of water and/or to the degradation products formed during the hydrolytic process or to the formation of holes in the bulk of the specimen during degradation or to the evolution in crystallinity of the polymer matrix [147] [150]. Indeed, as reported in Section 5.6, the hydrolytic degradation begins with the water molecule diffusion into the

amorphous regions which causes a random hydrolytic scission of ester bonds. The latter generates an increase in the crystallinity degree of the sample [151]. Surface fractures are evident after 40 days of burial, especially for pure polymer (Figure 5.24d). However, after 100 days, fragmentation progressed rapidly in all samples, which show a reduction in thickness and loss of material that is largely embedded with compost (Figure 5.24e). The greater fragmentation of pure polymer compared to green composites could be explained by: (i) higher degradation rates as fibre content decreases, (ii) increased mechanical strength of the composites due to the reinforcing effect of fibres.

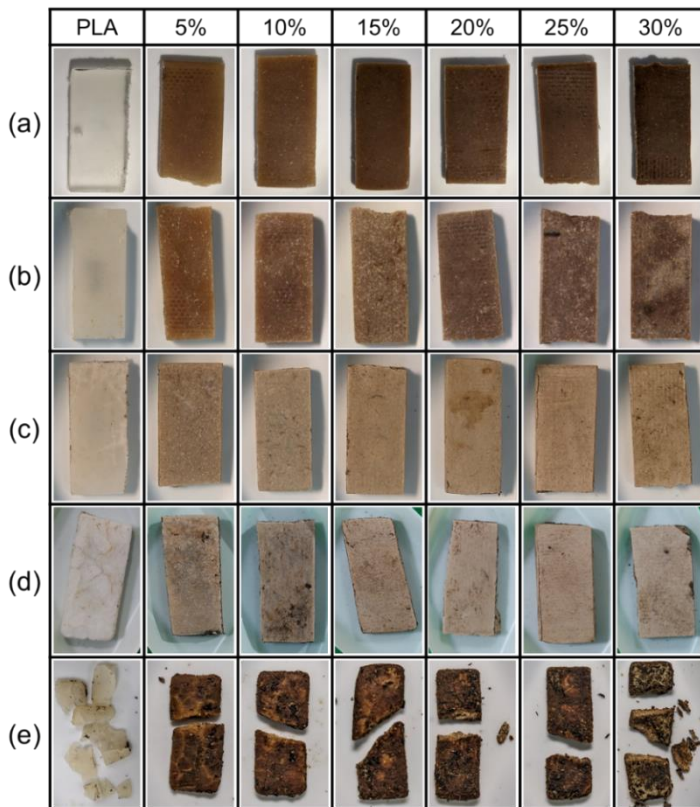


**Figure 5.24** Digital photographs of neat PLA and hemp shive-based composites with different volumetric fiber content unburied (a) and buried in compost at 55°C for 10 (b), 20 (c), 40 (d), and 100 (e) days.

To assess the effect of degradation on the thermal properties of materials, all samples were subjected to differential scanning calorimetry analysis at

different incubation times in compost. The measurements were carried out under the same conditions reported in Section 5.2. Three successively dynamic measurements were performed at 10°C/min heating/cooling rates: a first heating scan from 30 to 200°C, a cooling scan up to 30°C, and a second heating scan up to 200°C. All the scans carried out in the samples having an incubation time greater than 40 days were not distinguishable since the baseline was not linear and the transitions were not distinctly visible.

DSC thermograms and data recorded for the first heating scan of samples before and after 10, 20, and 40 days of burial in compost are shown in Figure 5.25 and Table 5.8, respectively. Before the burial test (Figure 5.25a), three clear thermal transitions along the increasing temperature axis were observed: glass transition (between 50°C and 70°C), cold crystallization (between 80°C and 120°C), and melt process (between 135°C and 160°C). An evident variation of thermal behaviour was shown during the degradation test. The glass transition temperature is clearly visible at zero-day and shows an endothermic phenomenon, the structural relaxation, overlapped with the glass transition. During the burial test, the  $T_g$  is less evident until it becomes unidentifiable for the samples buried for 40 days.  $T_g$  values identified in the first scan (Table 5.8) show equal initial values for all the systems and a greater reduction over time as fibre content decreases. When the glass transition is overcome, the cold crystallization phenomenon starts. The cold crystallization peak, clearly visible before the degradation test, shifts to higher temperatures reducing in intensity during the burial until it disappears after 20 days for composites at 0, 5, 10, 15 vol.% and 40 days for composites at 20, 25, and 30 vol.%. In detail, the onset cold crystallization temperature ( $T'_{cc}$ ) increased by more than 30% after 10 days for all the samples. The reduction of the glass transition temperature and the cold crystallization peak indicates a decrease in the mobile amorphous phase during composting [152]. The last thermal transition is the melting process. The onset temperature of the melting peak increase in the first 10 days at the high fibre content. After 20 days of burial, samples at  $\Phi \leq 15$  vol.% show the formation of two convoluted peaks. This result may be due to the formation of two different crystalline phases, one consists of the crystalline part of PLA marginally affected during the degradation, and the other one is formed by the crystals created during the degradation of the amorphous phase. As reported in Chapter 2 Section 2.5, the hydrolytic degradation of the amorphous regions is indeed the first phase of PLA biodegradation. The melting enthalpy grows with the burial time for all the samples. This phenomenon indicates that the degradation leads to a decrease in macromolecule chain length enabling secondary crystallization as a result of

an increase in the mobility of shorter chains and, especially, due to releasing the constraints in the material formed during the preparation of the testing specimens [152]. The crystallization degree was calculated according to Equation 5.1. An increase in the crystallization degree with the fibre content was observed at zero-day. The natural fibres provide a clear nucleating effect which contributes to increased crystallinity levels in non-degraded materials [153] [154] [155]. As a result of the burial in compost, the degree of crystallinity increased over time. The PLA biodegradation provides indeed a random hydrolytic scission phase of ester bonds in the amorphous regions which triggers the formation of new crystals [147]. In addition, the results show that the increase in  $\chi$  occurs to a greater extent as the fibre content decreases. The higher crystallinity triggered by the fibres during the manufacturing process caused a slowdown of the hydrolytic degradation in the amorphous domains and therefore greater resistance to degradation in the compost of the composite systems [97].

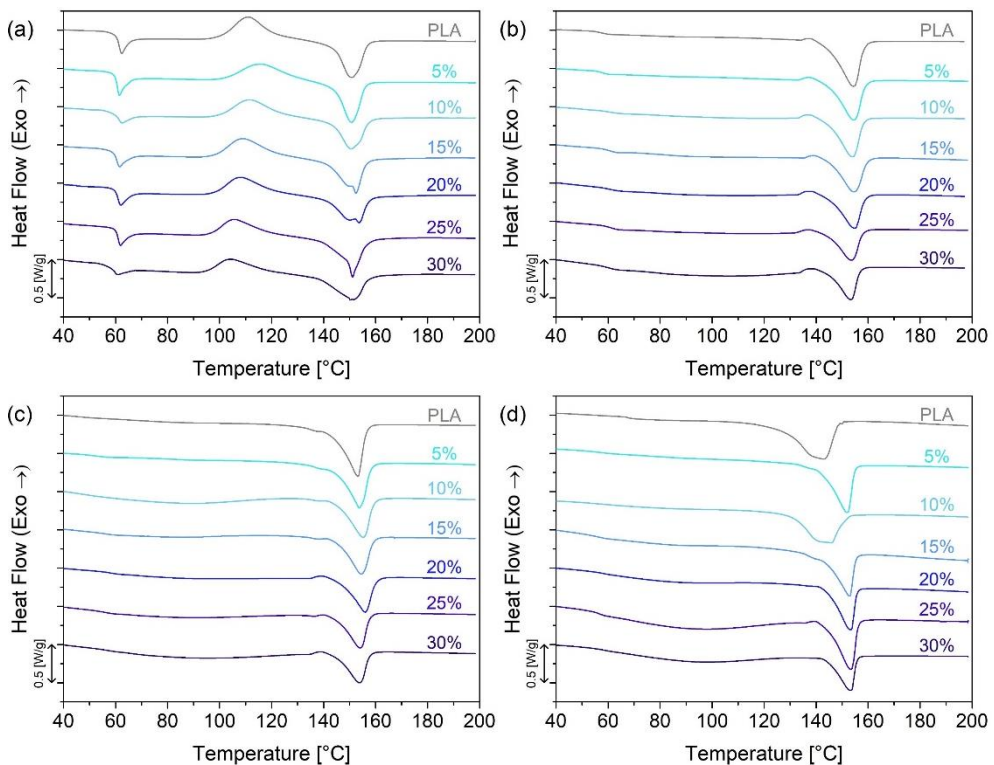


**Figure 5.25** DSC thermograms of neat PLA and hemp shive-based composites at different volumetric fibre content before (a) and after 10 (b), 20 (c), and 40 (d) days of burial in compost, first heating scan.

**Table 5.8** DSC data on hemp-based composites with different volumetric fibre content before and after 10, 20, and 40 days of burial in compost obtained from the first heating curves.

$\Phi$ [vol.%]	$T_g$ [°C]	$T'_{cc}$ [°C]	$\Delta H_{cc}$ [J/g]	$T'_m$ [°C]	$\Delta H_m$ [J/g]	$\chi$ [%]
<i>0 days</i>						
0	61.41	100.53	24.74	143.22	26.64	2.04
5	60.72	100.92	21.45	141.90	23.85	2.75
10	61.39	100.01	21.91	141.44	23.82	2.33
15	60.54	98.40	22.46	140.14	25.10	3.45
20	60.96	98.24	20.51	138.88	25.37	6.82
25	61.09	96.76	17.82	136.88	26.50	13.13
30	59.78	95.06	15.82	135.57	25.72	16.21
<i>10 days</i>						
0	57.35	134.48	0.58	141.81	31.67	33.43
5	57.83	133.56	0.88	141.58	28.01	31.05
10	60.62	133.31	1.26	140.65	26.38	30.67
15	60.04	135.55	0.84	143.09	23.39	29.47
20	60.50	133.33	1.44	142.89	22.36	29.36
25	61.42	132.45	0.85	142.90	19.56	28.30
30	60.57	133.73	1.26	143.03	18.08	27.55
<i>20 days</i>						
0	46.85	-	-	129.7	41.01	44.10
5	52.22	-	-	131.4	35.08	40.14
10	47.23	-	-	133.2	29.05	35.47
15	55.49	-	-	132.2	27.63	36.11
20	57.78	135.41	0.73	143.89	24.83	33.83
25	55.77	137.09	0.20	143.65	21.77	32.63
30	55.57	135.24	0.60	143.51	20.38	32.39
<i>40 days</i>						
0	-	-	-	123.03	49.35	53.06
5	-	-	-	127.54	38.87	44.48
10	-	-	-	128.84	35.36	43.18
15	-	-	-	129.84	30.57	39.95
20	-	-	-	144.51	25.15	35.29
25	-	-	-	144.53	23.48	35.52
30	-	-	-	144.56	18.95	31.03

The molecular weights of the neat PLA and the hemp shive-based composites at different burial times in compost were analysed by SEC analyses to assess the degradation entity of the samples. The testing conditions are given in Section 5.2.

Figures 5.26 and 5.27 present SEC chromatograms of the green composites in comparison with the neat poly(lactic acid) before and after 10, 20, and 40 days of burial in compost. The production step, when the materials were mixed and then hot pressed to obtain the samples for the degradation test, don't cause a relevant change in the molecular weight (Figure 5.26). SEC chromatograms show a narrow, unimodal, and moderately symmetrical distribution at day 0 for all the samples and a decrease of the weight average molecular weight ( $M_w$ ) negligible in composite systems compared to the neat matrix (Table 5.8). The moisture absorbed by the natural fibres thus did not trigger PLA degradation during the manufacturing process.

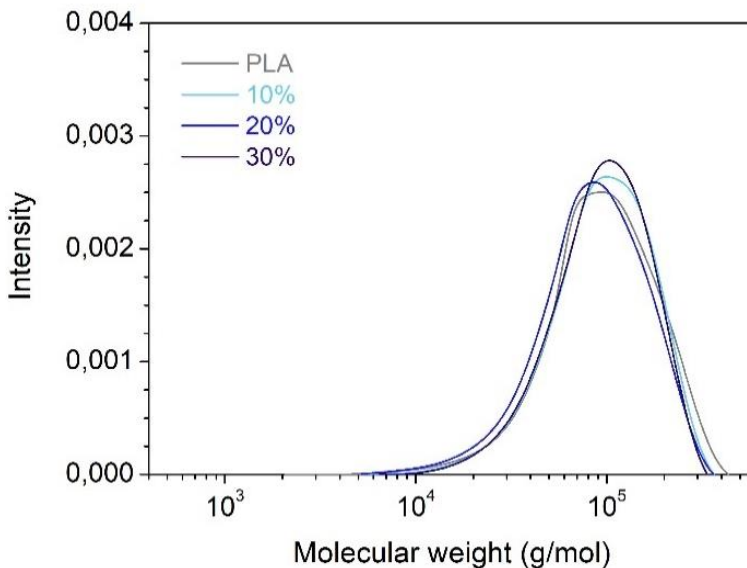


**Figure 5.26** SEC chromatograms of pure PLA and composites at 10, 20 and 30 vol.% before exposure to the composting environment.

**Table 5.9** Weight and number average molecular weight and polydispersity index of hemp shive-based composites at different volumetric fibre content before and after 10, 20, and 40 days of burial in compost.

$\Phi$ [vol.%]	$M_w$ [g/mol]	$M_n$ [g/mol]	PI
<i>0 days</i>			
0	115000	71200	1.61
10	112400	78800	1.43
20	120000	63000	1.62
30	110000	75700	1.45
<i>10 days</i>			
0	83000	48000	1.73
5	89000	52000	1.71
10	84000	50000	1.68
15	78500	46000	1.71
20	73000	42000	1.74
25	67000	38000	1.76
30	65000	37000	1.76
<i>20 days</i>			
0	24800	13500	1.84
5	41100	22400	1.83
10	53400	30600	1.75
15	56300	33300	1.69
20	71700	46300	1.55
25	63600	37100	1.71
30	70400	43100	1.63
<i>40 days</i>			
0	4800	3300	1.45
5	5150	3350	1.54
10	5250	3200	1.64
15	5450	2950	1.85
20	6100	3550	1.72
25	7350	3550	2.07
30	14200	4250	3.34

Samples were removed from the compost at different time intervals and analysed to gain a greater understanding of the degradation behaviours observed during the burial test. A relevant variation of the molecular weight

was observed after 10 days of burial (Figure 5.27a). A shift to the lower molecular weights of the chromatograms and a relevant reduction of  $M_w$  and  $M_n$  values (Table 5.9) were recorded as the natural fibre content increased. This result illustrates how the natural fibres, acting as channels for the absorption of moisture from the soil, affect the level of thermal hydrolysis of the PLA matrix after 10 days in compost [12].

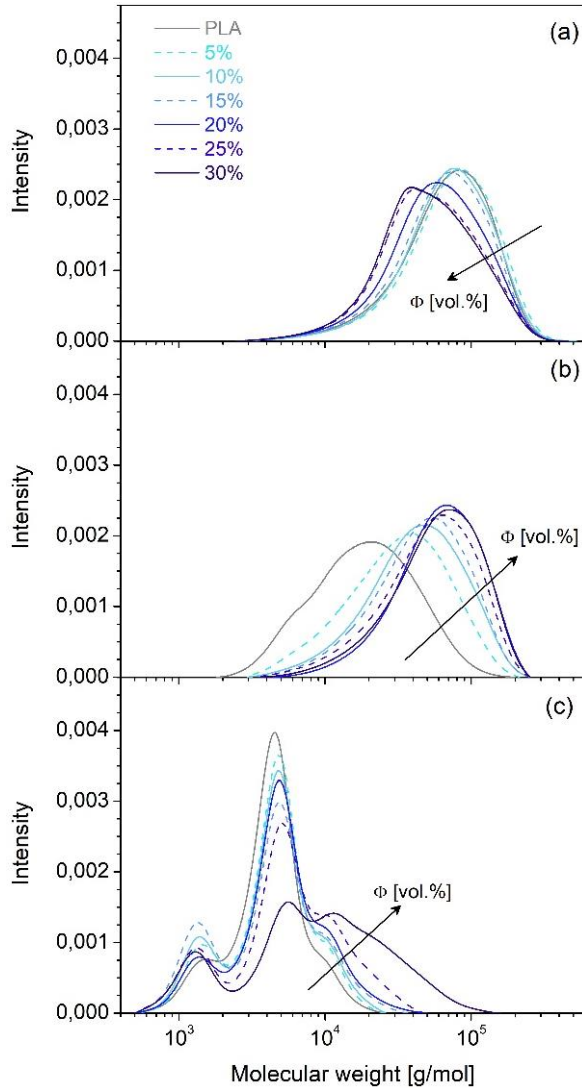


**Figure 5.27** SEC chromatograms of pure PLA and composites at different volumetric fibre content after 10 (b), 20 (c), and 40 (d) days of burial in compost.

An opposite trend of the degradation entity as the fibre content changed was observed after 20 days in compost (Figure 5.27b). High degradation rates were recorded in neat PLA and low-fibre content composites, while degradation was unchanged for high-fibre content. This behaviour can be related to the different crystallinity degrees of the samples before the burial test for the nucleating effect of the natural fibre (see Section 5.2 for more details). The higher crystallinity recorded at high fibre content slows down the hydrolytic degradation process which occurs preferentially in the amorphous regions of the polylactic acid [32] [31]. After 40 days, the molecular weight distributions show a shape variation from unimodal to trimodal (Figure 5.27c) and  $M_w$  values below the solubility limit of PLA oligomers in compost ( $M_{wc} = 35.272$  g/mol) (Table 5.9) [156]. In detail, PLA chains must be degraded to some extent to produce water-soluble fragments which could be subsequently released into the external environment containing degrading agents. Only from this point, the dissolved oligomers can be assimilated and mineralized by microorganisms in the compost. However, although the polymer chains are reduced sufficiently to become soluble, they can penetrate the cell membrane of microorganisms only when  $M_w$  reaches 10000 Da [28]. After 40 days, the pure PLA and composite systems show molecular weight distributions not only shifted toward sufficiently low values to release water-soluble fractions into the compost ( $M_w < M_{wc}$ ) but also to allow final mineralization.

The kinetics of the hydrolytic process that represents the first step of PLA biodegradation can be described as an autocatalytic mechanism [157]:

$$\frac{dC_c}{dt} = kC_cC_e \quad (5.8)$$

in which  $k$  is the kinetic constant that includes the water concentration inside the sample,  $C_c$  is the carboxylic end-groups concentration, and  $C_e$  is the ester concentration.  $C_c$  and  $C_e$  are related to the molecular weight as follows [128]:

$$C_c = \frac{\rho}{M_n} \quad (5.9)$$

$$C_e = \frac{\rho}{M_n} (DP-1) \quad (5.10)$$

where  $\rho$  is the polymer density, and DP is the average degree of polymerization, defined as the ratio  $M_n/M$  in which  $M$  is the molecular weight of the repeating unit ( $M=72$  g/mol for PLA). Substituting Equations (5.9) and (5.10) into equation (5.8) gives the following expression:

$$\frac{dM_n}{dt} = -k'(M_n - M) \quad (5.11)$$

in which  $k' = k\rho/M$  can be considered as the kinetic constant of the hydrolytic process and calculated by knowing the time evolution of the number average molecular mass of the sample (Figure 5.28a). The  $k'$  values at different burial times for neat PLA and composites at 10, 20 and 30 vol.% of fibres are reported in Figure 5.28b. The magnitude of the constants is consistent with those found in the literature [158] [31]. The time evolution of the kinetic constant validates the slowdown of the hydrolytic process in the samples with a high fibre content after 20 days of burial in compost. The crystallinity induced in the matrix by the nucleating effect of natural fibres delays the hydrolytic process of PLA.

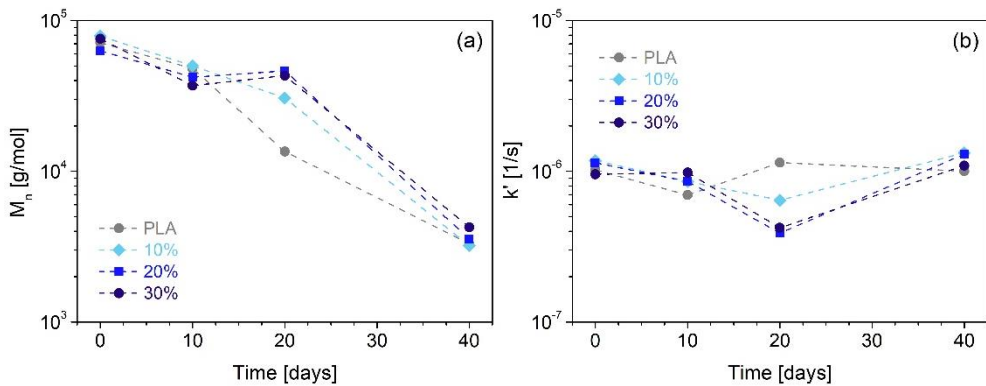


**Figure 5.28** Time dependence of (a) number average molecular mass and (b) kinetic constant of the hydrolytic process for neat PLA and composites at 10, 20 and 30 vol.%.





**PART**

**II**

# **Life cycle assessment of green composites**





## **Background: environmental impact analysis of green composites**

### **6.1 The concept of Life Cycle Assessment (LCA)**

Life cycle assessment (LCA) is an analytical and systematic methodology for assessing environmental impacts associated with all the stages of the life cycle of a commercial product, process, and service [159]. The purpose of conducting LCA studies varies from one application to another. In general, the main aim of using LCA is to reduce the environmental impact of products by guiding the decision-making process toward more sustainable solutions. Given the enormous versatility of the LCA tool, the guideline can not specify how to carry out each individual step. Rather, the International Organization for Standardization (ISO) provides a general protocol to follow and the necessary steps to complete an LCA. The general protocol to perform an LCA indicates that the steps of a product's life must be divided to identify each significant input and output of resources and energy. This rigorous procedure is vital to modify the life-cycle stages and improve environmental effects [160]. ISO 14040 and 14044 define the methodology of conducting a Life Cycle Analysis of a product. From the standards, the steps are (1) identify the goal and scope of the analysis, (2) compile a life cycle inventory (LCI), (3) complete a life cycle impact assessment (LCIA), and (4) interpret the results [161].

The aim of the analysis, the system boundary, and the stages of the product's life cycle considered are defined in the first step. In many studies, the framework of applying LCA is dealing with a "cradle-to-grave approach" which means that it deals with the product life cycle from the manufacturing phase (cradle) moving through the operational phase, and finally to the disposal phase (grave). There are other principles that deal with the "Cradle to Cradle concept" which is a specific kind of cradle-to-grave assessment, where the end-of-life disposal step for a product is a recycling process or in other words, an input for a new process. This kind of approach will lead to an open-loop study where the waste or disposed

materials will be used as raw materials for a new process. Another important parameter defined in the first step is the functional unit that is a set amount of product which is to be analysed, or some other quantity that describes what is being studied. By establishing a functional unit, all the input and output flows of all processes in a system can be compared and compiled. Further, a functional unit is useful for a comparative study of two different materials [162]. The life cycle inventory (LCI) analysis is assessed in the second step and consists in identifying and quantifying the resource flows for the system [163]. In other words, the purpose of LCI is to create an inventory of all inputs and outputs of materials, wastes, and natural resources for all processes, in relation to the functional unit [164]. In detail, this second step involves first the identification of the unit processes which are elementary steps in a product's life, and then the quantification of input and output flows for each unit process. Once data collection is completed, it is organized into a list or "inventory table" to be further analysed in the next step. The assessment of life cycle impact assessment (LCIA) is carried out in the third step to determine and evaluate the overall environmental impacts within the system. In detail, the inventory analysis results are converted to common units within several impact categories [161]. Mandatory phases of LCIA are: (1) selection of impact categories, (2) selection of impact category indicators, (3) classification of inventory results into categories, (4) characterization [161] [165]. Impact categories are groupings of resource flows and environmental factors that cause a common and general type of damage that must follow the goal and scope of the study. The three broad impact categories are: damage to human health, ecosystem health, and resources. However, impact categories more specific can be used [163]. Once the impact categories are established, they must be defined in terms of the characterization model, category indicators, and characterization factors. Subsequently, the assigning inventory results are performed in the third phase. The characterization is the fourth phase which consists of assigning a common unit to the results of each impact category so that the numbers can be aggregated to get a final value for the category, called the category indicator result. The complete list of category indicator results is then called the environmental profile. The optional phases of LCIA are normalization, grouping, and weighting. The final step of LCA is the interpretation of the results in order to be able to draw conclusions and recommendations. The purpose of the LCA is achieved if the results meet the goal and are within the initial scope. If not, the LCA may have to be redefined and repeated as it is not complete [162].

## 6.2 LCA of green composites

Well-known environmental awareness in the direction of attaining sustainability of manufactured goods has led to the development and adoption of environmentally friendly green composites. Unlike conventional synthetic composites, green composites are made of matrices and fiber coming from renewable resources [166]. This promising class of materials can be manufactured in the same way as conventional composites [167], yet substantial environmental benefits are expected during both the use phase and the end-of-life [168] [169]. To assess the environmental impacts associated with this new composite material class, a life cycle assessment (LCA) is hence crucial, possibly splitting the contributions of matrix and reinforcement to enable a conscious selection of the materials for realizing truly sustainable green composites [170]. LCA is a valuable tool for the development of green composites. In detail, a 'cradle-to-gate' assessment allows the production phase to be evaluated, while a 'cradle-to-grave' analysis allows the end-of-life disposal phase to be considered, which can be very significant for composite synthetics [171]. The choice of impact categories is crucial to achieve the objective of the study. Green composites are typically obtained from raw materials produced by agricultural processes. Therefore, impact categories influenced by agriculture must be selected in LCA [172] [173].

A 'cradle-to-grave' life cycle assessment of the green composites starts at the production phase where the most materials and resources are used and the most wastes are produced. The two components, i.e. natural fibres and matrix, must be analysed separately before evaluating the green composite production. In detail, fibre production typically requires crop growth, harvesting, transportation, and manufacturing, while matrix production typically includes raw material extraction, transportation, and manufacturing. Like natural fibres, many green matrices are made from agricultural crops [171]. The analysis of green composites must thus consider the land use impact since the land is a resource [174]. Natural fibres production requires several steps, and the environmental impact of each phase can vary significantly between fibre types. Plowing, sowing, and harvesting phases require the use of agricultural machinery which exploits fossil fuels for power and releases pollutants into the air. The use of fertilizers is often required both to provide farmland with the necessary nutrients for crops and to protect crops during growth from invasive weeds and insects. Transportation must be considered in different stages such as

the transportation of raw materials, finished product and raw waste collected at the place of production. The transportation aspect is typically characterized by the distance travelled and estimating the type and weight of the vehicle, which then leads to the amount of gas used [175]. Having the same or similar uses as traditional composites, the green composites use phase is often omitted in the LCA assuming an equal use and consumption of resources in this phase. This assumption is not valid when the materials have different durability. The latter has considerable influence on environmental impact since longer service lives lead to less material maintenance and replacement. Differences between natural and synthetic fibre use should be noted when the product's purpose is influenced by the weight of the component [176]. In fact, natural fibres have a lower density than synthetic fibres, which causes a reduction in the composite weight. The end-of-life disposal phase is the last step in the LCA of green composites. In this phase, natural fibre composites are potentially less impactful compared to synthetic fibre composites which generally end up in landfills. Landfill use is negative as it may not fully prevent the leaching of waste into the environment [177]. Incineration is an alternate option to landfill for green composites. Natural fibres stored carbon when harvested and retain it during use. When incinerated, the natural fibres release carbon in an amount equivalent to that sequestered by the plant from the atmosphere. Therefore, they do not cause an increase in emissions [178]. Another option for end-of-life disposal of green composites is the natural decomposition in compost. In this case, a biodegradable matrix must be used to avoid the fibre-matrix separation process [177]. The end-of-life disposal method indicated above is unable to generate new value-added products. Alternative methods in this direction include recycling, reusing, and reducing [179].



## Goal and methodology of LCA

Chapter 7 and 8 refer to the original version of the scientific paper published by Journal of Cleaner Production in January 2023 (Available at: <https://doi.org/10.1016/j.jclepro.2023.135901>)

A cradle-to-gate life cycle assessment study was performed to evaluate the environmental footprint of poly(lactic acid) based green composites loaded with natural fibres derived from kenaf and pine needles to compare cultivated and naturally grown feedstocks. In detail, the impact of raw material production/harvesting, (ii) transportation, (iii) fibre production, (iv) melt compounding, and (v) granulation to obtain the bio-pellets was assessed. The goal and scope identification, and the life cycle inventory compilation are assessed in the following chapter. The interpretation of the analysis results is reported in Chapter 8.

### 7.1 Selection of the raw materials

The poly(lactic acid) PLA supplied by NatureWorks LLC, USA (Ingeo™ 4060D, D-lactide content 12%) is selected as the matrix of the investigated green composites. This company's PLA was chosen for its lower environmental impact compared to other brands [27]. It is produced in the form of pellets at the manufacturing facility in Blair, Nebraska (USA), using corn as feedstock.

The natural fibres to be used as filler for the green composites were obtained from either naturally grown or cultivated feedstocks, that is pine needles and kenaf bast fibres, respectively (Figure 7.1a, c). Dry pine needles (from *Pīnūs pīnea*) were hand harvested in an area close to the Vesuvius National Park (Ercolano, Italy). After removing the fascicle sheath (see Figure 9.1a; yield ~88 wt.%), the pine needles were washed with water to remove residual dirt and topsoil and then dried in a vacuum oven at 45°C for 3 hours (Memmert Vacuum Drying Oven VO 400, Vacuumbrand™ PC 3001 Vario™ Pro). Finally, the dry fibres were ground (Retsch cutting mill

SM 100) to a size of a few hundred microns with a yield of ~90 wt.%. The resulting natural fibres (Figure 7.1b), herein referred to as PN, were used as filler to prepare the green composites. Kenaf bast fibres (Hibiscus cannabinus) were cultivated, harvested, and cleaned by mechanical decortication at the Kenaf Eco Fibers Italia (KEFI) plant in Guastalla, Italy. After transportation to the laboratory, the fibres underwent the same grinding process as the pine needles to get kenaf microfibers (yield of ~90 wt.%, Figure 7.1d), which are called KB in the following. The density of milled natural fibres was obtained by using a helium pycnometer (AccuPyc II 1340, Micromeritics—Alfatest, Italy). The measurement results are reported in Table 7.1.

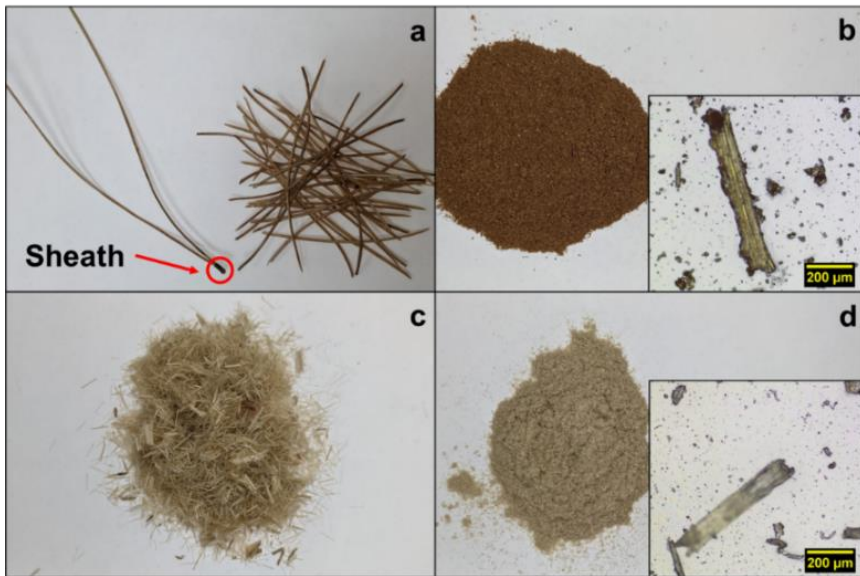


**Figure 7.1** Pine needles and kenaf fibres before (a, c) and after (b, d) the grinding process. The arrow in a) indicates the fascicle sheath. Magnifications in b) and d) show the microfibers obtained after grinding that were used for producing the green composites.

**Table 7.1** - Density of milled natural fibres.

Natural fibres	Density [g/cm <sup>3</sup> ]
Pine needles	1.47
Kenaf bast	1.57

## 7.2 LCA methodology

The main goal of this study is to perform a comparative life cycle assessment between neat PLA and green composites containing different amounts of natural fibres obtained from either kenaf or pine needles. The LCA methodology is applied according to the ISO 14040/44 series (ISO 14040, 2006; ISO 14044, 2006). The LCA analysis has been performed by using openLCA 1.10.3 (GreenDelta, GmbH, Berlin, Germany). To calculate the environmental burdens associated to the different production phases of the green composite pellets, the CML-IA [180] and Cumulative Energy Demand [181] have been selected as impact assessment methods. The chosen impact categories are global warming potential (GWP), primary energy of renewable and non-renewable resources (PED), acidification potential (AP), eutrophication potential (EP), photochemical ozone creation potential (POCP), and ozone depletion potential (ODP). Impacts also include human toxicity potential (HTP), freshwater aquatic ecotoxicity potential (FAETP), terrestrial ecotoxicity potential (TETP), and marine aquatic ecotoxicity potential (MAETP). The LCA analysis considers an impact assessment between the short- and the long-term time horizon [182] [183], which is identified in 25 years for the ODP and by 100 years for all the other categories.

## 7.3 Declared unit and system boundaries

The declared unit of the present study is 1 kg of bio-pellets of PLA filled with pine needle or kenaf bast fibre. The composite samples are classified as  $x$ KB and  $x$ PN, with  $x$  indicating the percentage volume fraction of microfibers. In the present study,  $x$  was varied between 10% and 40%. Pros and cons due to the presence of the lignocellulosic microfibers were assessed by using unfilled PLA as benchmark. A *cradle-to-gate* life cycle analysis was carried out, considering the following three processes: *a*) production of the microfibers; *b*) production of the PLA; *c*) manufacturing of the bio-pellets (Figure 7.2). The transport is considered in processes *a* and *b*, and it refers to the transfer of raw materials to the manufacturing centre (research laboratory). It is assumed that the production of the bio-pellets is performed in the same place where the fibres are ground (i.e., the transport phase is negligible for process *c*). The wastes deriving from the production of KB and PN (e.g., scraps produced during the manual cleaning prior the grinding and residues of the grinding process) are left outside the

system boundaries and are not included in the LCA analysis. It is important to observe that such biomasses are not harmful, and their use to produce peat could result in an environmental credit if a composting process was planned [184].

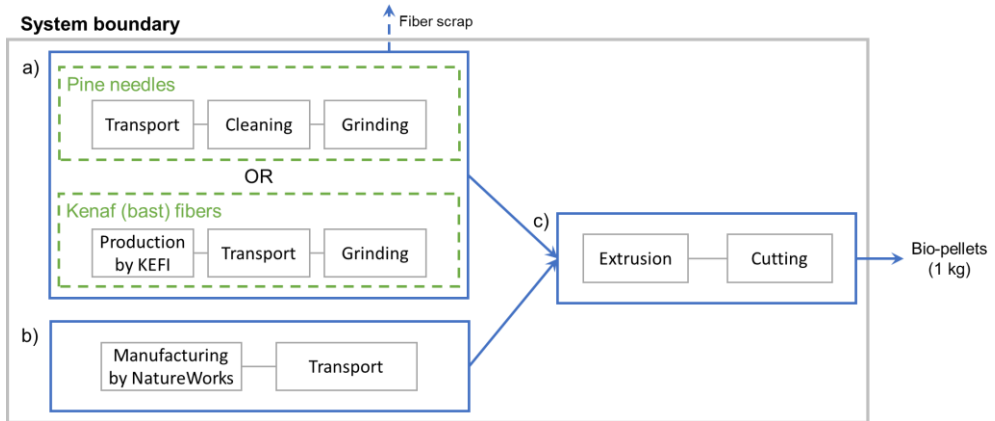


**Figure 7.2** System boundary (*cradle-to-gate* life cycle). The process is divided into three sub-processes: a) production of the microfibers; b) production of the PLA; c) manufacturing of the bio-pellets.

## 7.4 Life cycle inventory and data quality

The data of the life cycle inventory (LCI) included primary data collected at laboratory scale, and data from the ecoinvent database 3.7.1 [185], from the literature, and from manufacturer specifications. In the following, the inventory data are briefly presented with reference to the three sub-processes schematically reported in Figure 7.2.

### *LCI for production of the microfibers*

Inventory data for kenaf cultivation, harvesting and cleaning stages were taken from the literature [186] and reviewed with industry experts, who provided useful indication on the commercial availability of the employed chemicals and fertilizers and their current use. In detail, chemicals and fertilizer assumed for kenaf cultivation are:  $P_2O_5$ ,  $K_2O$ ,  $CaCO_3$ , and urea ammonium nitrate mix (ecoinvent 3.7.1). Fertilizer production data have been selected according to the following order of priority: Italian market, European market, and global market if none of the abovementioned was

available. The harvesting phase was enriched with contributions deriving from the use of agricultural machinery, generally not considered in LCA studies although they account for a non-negligible fraction of the impacts. According to the agricultural guidelines by ecoinvent, the use of agricultural machinery for the harvesting phase of kenaf fibres is considered as a material input flow to the process. Knowing the average amount of kenaf grown per hectare (ha), equal to 15 t/ha [187], the amount of machinery (AM, in kg/WU) was estimated as:

$$AM = W \cdot \frac{OT}{ML} \quad (9.1)$$

where  $W$  is the weight of the machinery,  $OT$  is the operation time (i.e., how long the machinery is used for the process, in hours/WU), and  $ML$  is the machinery lifetime (in hours). The operation time to collect the reference amount of feedstock (working unit (WU), set to 3.9 kg of plant fibre) needed to produce 1 kg of KB was assumed to be the same as reported by Berhongaray et al. [188] for non-woody crops such as kenaf. Other soil management operations (tillage, sowing, etc.) and machinery use (seeder, tractors) are not included in the LCA model due to a lack of data. The Italian market for electricity at high voltage (market for electricity, high voltage | Cut-off, S – IT, ecoinvent 3.7.1) was considered for mechanical decortication of kenaf fibres, which carried out at the industrial scale.

The transport of the pine needles from the harvesting area to the research laboratory (ca. 26 km) was carried out using a light commercial vehicle (transport, freight, light commercial vehicle | Cutoff, S – Europe without Switzerland, ecoinvent 3.7.1). Regarding the kenaf bast fibres produced at the KEFI plant, we assumed that they come from the same area of pine needles. Such an assumption, which is plausible since also the area is suitable for the cultivation of kenaf (Kenaf Eco Fibers Italia), allows a comparison of the two kinds of fibres without considering external factors, such as the impact of transportation from different sites. In this way, the differences in the environmental impact only reflect the fibre nature and, above all, the use of fertilizers needed in the case of kenaf.

Starting from the kenaf fibres by KEFI and the harvested pine needles, microfibers were obtained at the laboratory scale through a grinding process. Only for pine needles, a preliminary cleaning was carried out, as described in Section 7.1. The inventory data of the treatment of non-polluting waters resulting from the washing of pine needles was taken from

the ecoinvent database. The energy consumption of the machinery involved for drying pine needles after the washing step, and for the grinding process was monitored with a wattmeter. The recorded data were then factored with respect to the capacities of the appliances, supplied by the manufacturers, so as to define consumption regardless of mass and volume. For laboratory scale processes, the Italian market for electricity at medium voltage (market for electricity, medium voltage | Cut-off, S – IT, ecoinvent 3.7.1) was considered for the energy input flow in the LCA model. It is assumed that 100% of the electricity consumed is converted to waste heat, which is fully released to the air.

### *LCI for PLA production*

The PLA production data are specific of the selected matrix and fully meet the quality requirements set by the standard [189]. Two transportation routes, named “cargo aircraft” and “container ship” were considered for the transportation of PLA from the NatureWorks LLC manufacturing facility located in Blair, Nebraska (USA) to the research laboratory in Naples (Italy) where the green composites were produced. The total distance of the cargo aircraft route is about 9181 km, 89% of which is covered by air and 11% by road. The details of the “cargo aircraft” transportation step are shown below (see schematic representation in Figure 7.3):

- Transport from NatureWorks LLC manufacturing facility to Blair Municipal Airport by 3.5-7.5t truck (19 km);
- Transport from Blair municipal airport to the Eindhoven airport, the Netherlands, by direct freight flight (7211 km);
- Transfer from Eindhoven airport to Ravago Distribution Center (NV Moerenstraat 85A, Arendonk, Belgium). According to company information [190], NatureWorks relies on Resinex, a company based in Arendonk, Belgium, for the distribution of Ingeo™ polymer in Europe. The transportation is done by 3.5-7.5 tonne truck (41 km);
- Transfer from Ravago Distribution Center to the Eindhoven airport. It has been deemed necessary to consider this route again for logistical reasons (41 km);
- Freight flight from Eindhoven airport to Bergamo airport, Italy (1000 km);
- Transport by 3.5-7.5t truck from Bergamo airport to the Resinex Italian headquarters [191] (18 km);

- Transport from the Italian headquarters of Resinex to the research laboratory in Naples, Italy, by light commercial vehicle (850 km).

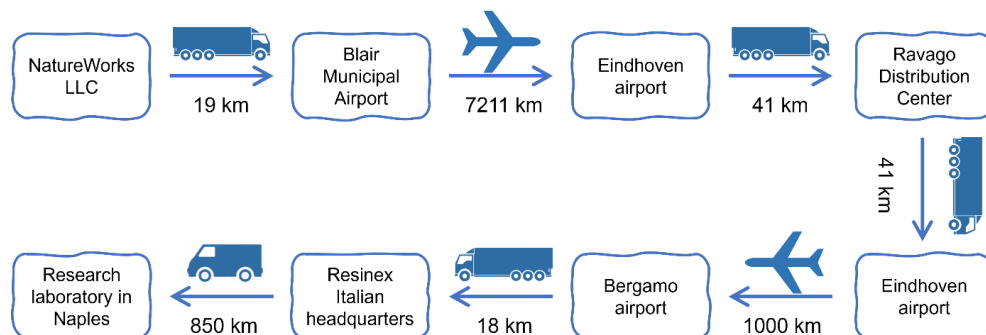


**Figure 7.3** Schematic overview of the main transportation steps of PLA with cargo aircraft.

Instead, the total distance of the container ship route is about 11260 km, 64% of which is accomplished by container ship, 22% by road and 14% by railway. The details of the “container ship” transportation step are shown below (see schematic representation in Figure 7.4):

- Transport from NatureWorks LLC manufacturing facility to the port of New York, USA, (about 2000 km). Considering the Freight Rail map by the U.S. Department of Transportation [192], it is estimated that 1400 km occur by freight train and 600 km by 3.5-7.5 tonne truck;
- Transport from the port of New York to the port of Rotterdam, the Netherlands, by container ship (7260 km);
- PLA is then transported from Rotterdam port to Ravago Distribution Center (Moerenstraat 85A Arendonk, Belgium) by 3.5-7 tonne truck (100 km);
- Transport from Ravago Distribution Center to the Resinex Italian headquarters in Bergamo, Italy (about 1050 km). Considering the report of the European Union Agency for Railways [193], it has been estimated that about 180 km are covered by rail and 870 km by 3.5-7.5 tonne truck.
- Transport from the Resinex Italian headquarters to the research laboratory in Naples, Italy, by light commercial vehicle (850 km).

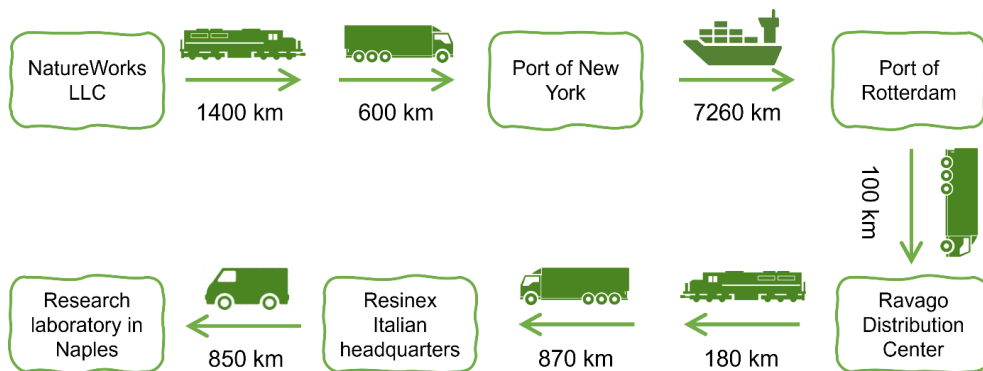


**Figure 7.4** Schematic overview of the main transportation steps of PLA with container ship.

### *LCI for manufacturing of bio-pellets*

The melt mixing process to produce the bio-pellets of PLA filled with either PN or KB was modeled by averaging energy consumption data provided by different machinery manufacturers. Table 7.2 reports the data of different extruders used for the inventory phase of the production of the bio-pellets.

**Table 7.2** Inventory data of twin-screw extruders considered for the production of green composites.

<b>Extruder model</b>	<b>Flow rate (average) [kg/h]</b>	<b>Energy consumption [MJ/kg]</b>
MILACRON TP 75-26	430	1.13
XINDA PSHJ-65	250	2.78
MEIZLON MTX-65	400	1.67
<b>MEAN</b>	<b>360</b>	<b>1.86</b>

Only twin-screw extruders were considered for data collection as their widespread use is justified by better dispersion of fibre and matrix [194]. The computed average of the energy consumption for the extrusion process (1.86 MJ/kg) is comparable to values reported in literature (2 MJ/kg). The energy consumption accounts for the use of the driving power motor, the heating elements, and the pressure control system. Lubricant consumption

and system maintenance interventions were also considered in the designed LCA process by extracting data from the ecoinvent database and adapting them to the present study. At the end of the extrusion process, the extrudate is granulated using a cutting machine to get pellets of green composite. An energy consumption of 80 kJ per kg of pellets was estimated for the granulation phase from manufacturer specifications sheets.

# 8

## **LCA result interpretation of the PLA-based composites filled with pine needles and kenaf fibres**

### **8.1 Environmental impact of microfibers – Naturally grown vs. cultivated feedstocks**

The first step in the life cycle assessment of green composites is the evaluation of the environmental footprint of the single phases: fibres and matrix. Table 8.1 shows the environmental impact parameters related to the production phase of 1 kg of pine needles (PN) and kenaf bast (KB). Since the transport and grinding phases are the same for the two kinds of fibres, the electricity required for washing and drying the pine needles and the fertilizers and other chemicals used to cultivate the kenaf are the factors that lead to differences in their environmental impact. To highlight the differences between fillers derived from naturally grown and cultivated feedstocks, the contributions related to electricity for microfiber production (vacuum drying and grinding), cultivation (irrigation water, chemicals and fertilizers, agricultural machinery), and other sources are shown in Figure 8.1 for each of the environmental impact parameters of Table 8.1 (see Appendix A.1 for the detailed allocations). The net GWP indicators are negative, meaning that both feedstocks absorb more CO<sub>2</sub> during the growth phase than they release in the environment when transformed into fillers for green composites. CO<sub>2</sub> emissions and sequestration data are specified in Table 1 for both fibres. The CO<sub>2</sub> uptakes were calculated by following the biomaterial storage approach [195], assuming an average C content of 50% for pine needles [196] [197] and of around 52% for kenaf fibres [198]. Surprisingly, despite the absence of the cultivation step, the comparison is only slightly favourable to the PN (+8% of net CO<sub>2</sub> uptake). Similarly, only a moderate advantage emerges in terms of PED (9.2% reduction). Such mild environmental gains in terms of greenhouse gas emissions and energy demand indicate that the advantage deriving from the absence of cultivation step for the PN are almost completely compensated by the electric energy

used for vacuum drying the pine needles before grinding. In fact, as shown in Figure 8.1 electricity is the main contributor to the environmental impact of the PN production. The advantage of using pine needles could increase in case of scale up from laboratory to industrial scale production. The impact of cultivation more clearly emerges when looking at other environmental indicators. Dealing with a natural feedstock such as pine needles is clearly preferable in terms of human toxicity and ecotoxicity, whose impact indicators are from 47.9% to 63.8% lower than in case of KB. This is mostly due to the use of fertilizers and other chemicals to grow the plants from which kenaf fibres are obtained at industrial scale.

**Table 8.1** Environmental impact potentials for the production of 1 kg of PN and KB at the gate (CML-IA and Cumulative Energy Demand impact assessment methods).

Impact category	Pine needles	Kenaf bast	Unit	PN over KB environmental benefit [%]
GWP	CO <sub>2</sub> emission	$9.60 \cdot 10^{-1}$	kg CO <sub>2</sub> eq./kg fibres	8.0 (net GWP)
	CO <sub>2</sub> sequestration	$-1.83 \cdot 10^0$		
	Total	$-8.70 \cdot 10^{-1}$		
PED	$1.86 \cdot 10^1$	$2.05 \cdot 10^1$	MJ eq/kg fibres	9.2
AP	$3.62 \cdot 10^{-3}$	$5.01 \cdot 10^{-3}$	kg SO <sub>2</sub> eq./kg fibres	27.7
EP	$9.70 \cdot 10^{-4}$	$1.38 \cdot 10^{-3}$	kg PO <sub>4</sub> eq./kg fibres	29.7
HTP	$1.69 \cdot 10^{-1}$	$3.50 \cdot 10^{-1}$	kg 1,4-DCB eq./kg fibres	51.7
FAETP	$2.70 \cdot 10^{-1}$	$5.36 \cdot 10^{-1}$	kg 1,4-DCB eq./kg fibres	49.5
TETP	$1.70 \cdot 10^{-4}$	$4.70 \cdot 10^{-4}$	kg 1,4-DCB eq./kg fibres	63.8
MAETP	$9.70 \cdot 10^{-1}$	$1.85 \cdot 10^0$	kg 1,4-DCB eq./kg fibres	47.9
POCP	$1.90 \cdot 10^{-4}$	$2.10 \cdot 10^{-4}$	kg ethylene eq./kg fibres	9.5
ODP	$1.57 \cdot 10^{-7}$	$1.65 \cdot 10^{-7}$	kg CFC-11 eq./kg fibres	4.7

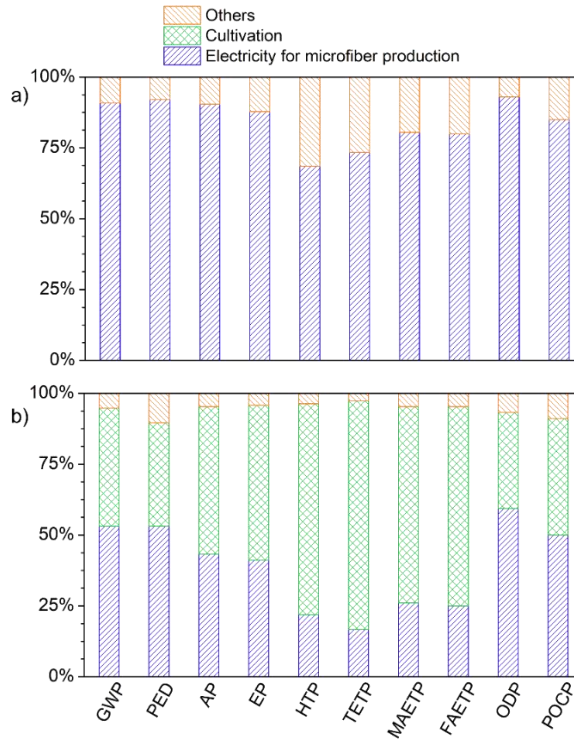


**Figure 8.1** Percentage contributions to the impact categories of Table 8.1 deriving from electricity for microfibers production, cultivation, and other impact sources used to produce pine needles (a) and kenaf bast (b).

For the ozone-related indicators, instead, the environmental gains are only marginal. Overall, the results in Table 8.1 point out that the use of fibres obtained from naturally occurring feedstocks is a winning choice for lowering the environmental impact of green composites production. More in general, similar considerations can be potentially extended also to green garden and park wastes, which have been recently investigated as resource for the production of fillers for composites [199].

## 8.2 Environmental impact of PLA

The environmental impact parameters for the production and transport phases of PLA are reported in Table 8.2. Two routes were hypothesized to carry out the transportation of the polymer from the manufacturing company to the research laboratory: the “cargo aircraft” route uses both freight aircraft and road transport; the “container ship” route uses the railway

network, a container ship, and road transport (see Chapter 7 Section 7.4 for details).

**Table 8.2** Environmental impact potentials for the production and transport phases of PLA (CML-IA and Cumulative Energy Demand impact assessment methods).

Impact category	Production	Transportation		Unit
		Cargo aircraft	Container ship	
GWP	$6.20 \cdot 10^{-1}$ <sup>a</sup>	$5.18 \cdot 10^0$	$2.53 \cdot 10^0$	kg CO <sub>2</sub> eq./kg PLA
PED	NREU	$4.01 \cdot 10^1$	$7.92 \cdot 10^1$	MJ eq./ kg PLA
	REU	$2.66 \cdot 10^1$	$8.10 \cdot 10^{-1}$	MJ eq./ kg PLA
AP	$7.26 \cdot 10^{-3}$	$2.38 \cdot 10^{-2}$	$1.33 \cdot 10^{-2}$	kg SO <sub>2</sub> eq./ kg PLA
EP	$1.38 \cdot 10^{-3}$	$4.49 \cdot 10^{-3}$	$2.87 \cdot 10^{-3}$	kg PO <sub>4</sub> eq./ kg PLA
HTP	$1.12 \cdot 10^{0b}$	$6.80 \cdot 10^{-1}$	$6.30 \cdot 10^{-1}$	kg 1,4-DCB eq./kg PLA
TETP	$4.14 \cdot 10^{-3b}$	$8.0 \cdot 10^{-4}$	$6.8 \cdot 10^{-4}$	kg 1,4-DCB eq./kg PLA
MAETP	$5.11 \cdot 10^{0b}$	$3.49 \cdot 10^0$	$3.63 \cdot 10^0$	kg 1,4-DCB eq./kg PLA
FAETP	$2.01 \cdot 10^{0b}$	$9.30 \cdot 10^{-1}$	$1.00 \cdot 10^0$	kg 1,4-DCB eq./kg PLA
POCP	$6.00 \cdot 10^{-4}$	$8.80 \cdot 10^{-4}$	$7.30 \cdot 10^{-4}$	kg ethylene eq./ kg PLA
ODP	$3.99 \cdot 10^{-13}$	$8.09 \cdot 10^{-7}$	$3.77 \cdot 10^{-7}$	kg CFC-11 eq./kg PLA

a. Net GWP value, i.e., the value obtained subtracting the biogenic carbon sequestration of corn feedstock (1.83 kg CO<sub>2</sub>) to the total GHG emissions.

b. Indicator values based on a different dataset (polylactide production | Cut-off, S – GLO, ecoinvent 3.7.1), which may be overestimated since it considers the energy mix of Continental Europe (UCTE grid mix).

The production phase mainly contributes to the toxicity-related indicators (HTP, TETP, FAETP, MAETP). The latter, which reflect the use of chemicals and fertilizers to grow the crops PLA, were estimated from a dataset (polylactide production | Cut-off, S – GLO, ecoinvent 3.7.1) that refers to the energy mix of Continental Europe (UCTE grid mix) and could be overestimated. The plant-specific-energy mix was instead considered for the other environmental indicators. Comparing the two transportation routes, the cargo aircraft pathway has about twice the impacts compared to the container ship pathway as far as the GWP, NREU, REU and ODP indicators are concerned, while the difference is less prominent in the remaining impact categories. Even in the “best case” of container ship, transportation is responsible for about 80% of the greenhouse gas emissions

and 50% of the primary energy from non-renewable resources. Looking at the other indicators, transportation accounts for about 65% of the acidification and eutrophication potential, more than half of the photochemical ozone creation potential, and essentially the entire ozone depletion potential. A conscious selection of raw material suppliers and shipping method is, hence, crucial to make truly sustainable green composites. More in general, it clearly emerges that the supply chain plays a major role in determining the overall sustainability of composite materials, even when they are obtained from green feedstocks such those addressed in the present study.

### 8.3 Environmental impact of bio-pellets at different fibre content

Once the impacts of PLA and microfibers have been separately assessed, the environmental impact of the green composites has been computed by assuming a simple additivity rule and adding the contribution of the manufacturing (phase “c” in Figure 7.2, reported in Table 8.3). The results of this procedure are shown in Figure 8.2, in which the environmental gains/losses of bio-pellets compared to pure PLA pellets are shown for different fibre content.

**Table 8.3** Environmental impact potentials for the manufacturing of 1 kg of bio-pellets (CML-IA and Cumulative Energy Demand impact assessment methods).

Impact category	Manufacturing	Unit
GWP	$2.40 \cdot 10^{-1}$	kg CO <sub>2</sub> eq./kg bio-pellets
PED	NREU $3.92 \cdot 10^0$	MJ eq./kg bio-pellets
	REU $7.40 \cdot 10^{-1}$	MJ eq./kg bio-pellets
AP	$8.90 \cdot 10^{-4}$	kg SO <sub>2</sub> eq./kg bio-pellets
EP	$2.30 \cdot 10^{-4}$	kg PO <sub>4</sub> eq./kg bio-pellets
HTP	$3.32 \cdot 10^{-2}$	kg 1,4-DCB eq./kg bio-pellets
FAETP	$6.22 \cdot 10^{-2}$	kg 1,4-DCB eq./kg bio-pellets
TETP	$3.37 \cdot 10^{-5}$	kg 1,4-DCB eq./kg bio-pellets
MAETP	$2.20 \cdot 10^{-1}$	kg 1,4-DCB eq./kg bio-pellets
POCP	$4.32 \cdot 10^{-5}$	kg ethylene eq./kg bio-pellets
ODP	$3.96 \cdot 10^{-8}$	kg CFC-11 eq./kg bio-pellets

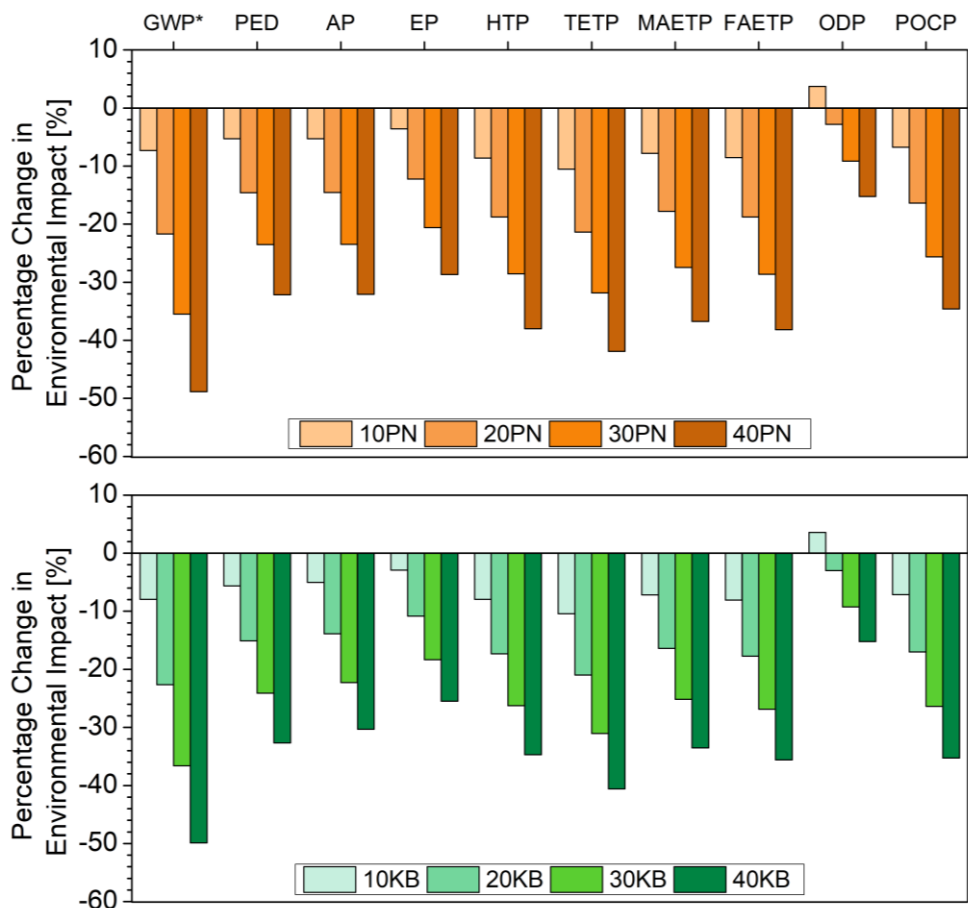


**Figure 8.2** Percentage change in the environmental impacts of  $x$ PN and  $x$ KB bio-pellets with respect to pure PLA pellets.

Notably, all deviations are negative, meaning that green composites are preferable with respect to the pure PLA from the environmental point of view. This result reflects the clear predominance of the impacts of PLA compared to those of the microfibers (Table 8.1 and 8.2). Because of such a disparity, realizing green composites means replacing a fraction of “highly impacting” PLA with an essentially “neutral” phase, i.e., natural fibres having a negligible impact. The only exception is represented by the ODP indicator of the composites containing 10% of natural fibres, for which the addition of the contribution related to the manufacturing step is not counterbalanced by the benefits associated to the presence of the fibres.

Nonetheless, environmental advantages of substituting PLA emerge at higher fibre contents. Similar conclusions were also drawn for coffee jar lids in which PLA is replaced with banana fibres (Rodríguez et al., 2020). More in general, the polymer production step was found to constitute the largest contributor to the impact of biocomposites, and thus the maximum filler content should be increased to gain environmental benefits [200].

The results reported in Figure 4 also highlight that negligible differences can be noticed between PN- and KB-based composites. Overall, the percentage environmental gains ensured by the fibres (whatever they are) are of the same order of magnitude of the percentage of fibres in the composite. As an example, a green composite containing 20% of microfibers is expected to exhibit around a 20% reduction of most of the impact indicators with respect to pure PLA. A positive deviation from this simple rule regards the greenhouse gas emissions, which benefit from the CO<sub>2</sub> credits of the fibres (see Table 8.1). The environmental gains of the green composites are, instead, less pronounced when looking at the PED, AP and EP indicators. This means that PN and KB contribute to some extent to such impact categories. Finally, the rule is respected, i.e., the percentage benefits reflect the percentage amounts of fibres, when considering the toxicity-related indicators HTP, FAETP, TETP and MAET. In this regard, the dominance of the PLA contribution almost nullifies the advantage related to microfibers obtained starting from naturally grown feedstocks (PN) instead of cultivated ones (KB). This conclusion only marginally depends on the energy mix selected for computing the toxicity-related indicators of PLA. Assuming a drastic cut by 50% of the impact of the electric energy indeed results in differences between PN- and KB-based composites of 8% at most. The preferability of naturally grown feedstocks could emerge more clearly in case of optimized production processes. As far as our PN are concerned, the drying process of the pine needles after washing and cleaning proved to be the hot spot of the lab scale treatment.

## **8.4 Functionality-based LCA – Preliminary investigation of the mechanical performance of the green composites**

Green composites often find application as semi-structural components in industrial sectors such as automotive, construction, and packaging [201] [202] [203] [204]. To obtain an effective reinforcing action, cellulose-rich fibres should be preferred, and surface treatments should be performed to enhance the quality of fibre-matrix interactions [205]. None of these

approaches have been pursued here, as we were mainly interested in quantifying the environmental advantages of green composites. Nonetheless, the selected fibres are expected to improve to some extent the performance of the studied materials. This has an indirect consequence on the overall sustainability of the composites since enhanced performances potentially allow for material savings [206]. For this reason, we estimated the mechanical performances of our samples and converted them into weight reductions. The detailed procedure is based on the concept of “material index” and can be found in [207].

Here we consider the design of a rectangular panel of green composite material subjected to bending during its lifecycle. The following expression is obtained for the mass  $m$  of the panel:

$$m = k \frac{\rho}{E^{1/3}} \quad (8.1)$$

In Equation (8.1),  $k$  is a function of panel geometry and bending stiffness,  $\rho$  is the material density, and  $E$  is the flexural modulus. To produce panels with the same geometry and bending stiffness made of different materials,  $k$  must be set as a constant, and the mass of the panels will only depend on the material index  $\rho E^{-1/3}$ . This means that the lower the density and the higher the modulus, the lower the mass of the panel for a given bending stiffness.

The density of the composites can be obtained as the weighted average of the density of polymer and fibres. The flexural modulus was measured through 3-point bending tests on samples in form of rectangular bars ( $50 \times 12 \times 3 \text{ mm}^3$ ) obtained by compression molding of bio-pellets. The analyses were carried out at room temperature with a span length of 30 mm and at a constant crosshead speed of 0.5 mm/min (ASTM D790). Figure 8.3a show the flexural modulus for the two series of green composites as a function of fibre content. The presence of the microfibers determines a monotonic increase in the flexural modulus, the effect being much more pronounced for the KB-based composites. Using Equation (8.1), the percentage weight reductions with respect to a pure PLA panel were easily obtained and are shown in Figure 8.3 for composites at different fibre content.

Although the density of both fibres is higher than that of PLA (1.57 and 1.47 g cm<sup>-3</sup> for KB and PN, respectively, vs. 1.24 g cm<sup>-3</sup> for PLA [208]) all green composites benefit from the enhanced flexural modulus and

eventually ensure the same bending stiffness of a PLA panel at reduced weight. The gain is higher for the KB samples, with a weight reduction of about 8% at 30% of fibres. No further improvements seem achievable above this threshold for this fibre. The maximum weight reduction for PN-based composites is lower, reaching about 3% at 40% of fibres.

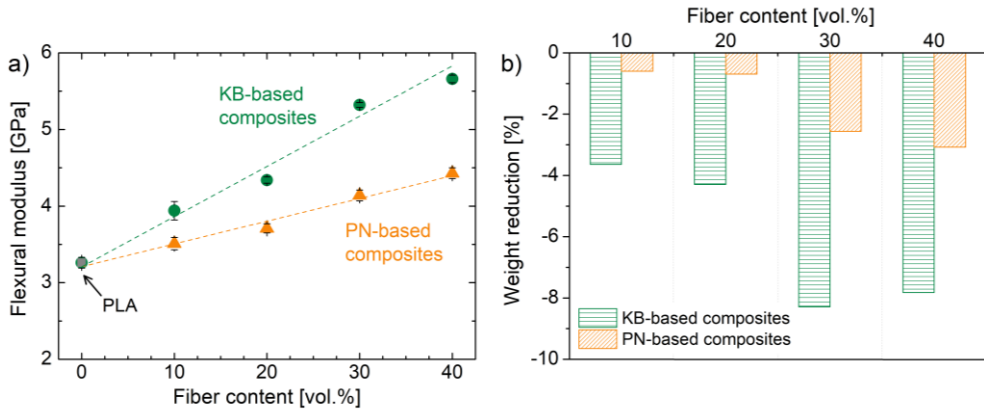
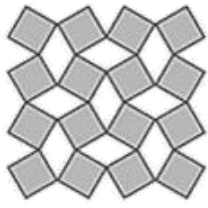


**Figure 8.3** a) Flexural modulus of green composite samples as function of the fibre content. (dashed lines are guides for the eye). b) Percentage weight reduction achievable using green composites at different fibre content to realize a rectangular panel at fixed bending stiffness.

In the framework of a functionality-based LCA, the differences between the environmental indicators of PN- and KB-based composites should be recomputed to account for the need of less material at equal (flexural) performance in the case of KB. This might reduce and, in some cases, nullify the advantages of starting from non-cultivated raw materials such as pine needles. Although this conclusion cannot be generalized to other systems, it clearly emerges the importance of functionality-based LCA approaches, which should always be adopted when dealing with new materials/formulations or when redesigning products or components







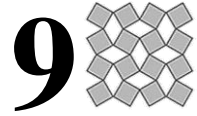
**PART**

**III**

**Design of biodegradable  
polymer-based auxetic  
mechanical metamaterials**







# **Background: geometries, characteristics, and manufacturing of auxetic mechanical metamaterials**

## **9.1 What is an auxetic mechanical metamaterials?**

The behaviour of a material subject to external mechanical stresses depends on Poisson's ratio ( $\nu$ ) which is defined as the negative ratio of the transverse strain to the axial strain in the direction of loading [209]. The materials are usually characterized by a positive Poisson's ratio, that is, they contract transversely under uniaxial extension and expand laterally when compressed in one direction. However, this common knowledge has been challenged by the auxetic mechanical metamaterials which have negative Poisson's ratios, i.e., they become wider when stretched and narrower when squashed [210] [211] [212]. According to the classical elasticity theory, the variation range of  $\nu$  is from -1 to 0.5 for three dimensional (3D) isotropic materials and from -1 to 1 for two dimensional (2D) isotropic systems [213] [214] [215]. A larger variation range can be identified for the anisotropic materials [216]. The variation scopes of  $\nu$  clearly show that the auxetic effects are allowable in linear elastic and thermodynamically correct materials. The unusual mechanical response under deformation has made the auxetic materials subject to numerous research [217] [218] [219]. In detail, extensive studies have been done to understand the origin of the auxetic behaviour and to compare the response of the auxetic materials to conventional materials. It has been found that auxeticity can be described in terms of the particular geometry of the material system and the deformation mechanism when loaded [220]. The negative Poisson's ratio is a scale independent property [221], that is, the auxetic behaviour can be achieved at a macroscopic or microstructural level, or even at the mesoscopic and molecular levels. To date, a variety of auxetic materials and structures have been discovered, fabricated, or synthesized ranging from the macroscopic down to the molecular levels. Over the past decades, different auxetic structures are proposed and identified. Among the most important classes are chiral structures [222] [223] [224], re-entrant structures [225] [226]

[227] and rotating rigid structures [220] [228] [229] (Figure 9.1). The study of these geometrical structures can help researchers to understand how new auxetic structures can be designed as well as how their properties can be optimized and predicted.

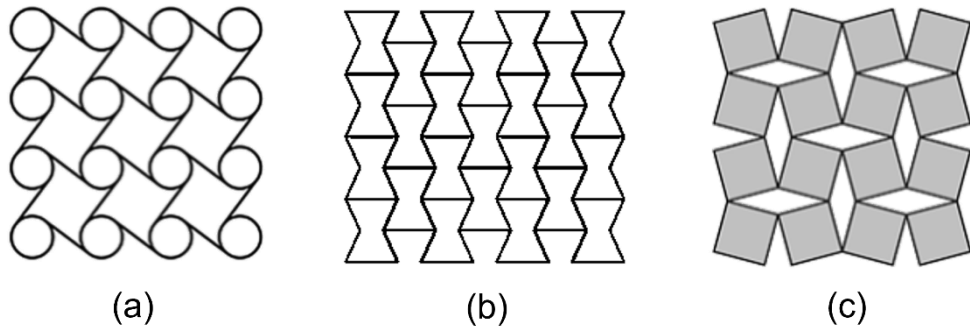


**Figure 9.2** Example of chiral structure (a), re-entrant structure (b) and rotating rigid structure (c).

The chirality concept, introduced by Kelvin [230], indicates a structure not superimposable on its mirror image. The chiral structures are made up of basic chiral units which are obtained by connecting straight ligaments (ribs) to central nodes in different geometric shapes (i.e., circles, rectangles, or others). The combination of different basic chiral units generates the overall structure (Figure 9.1a). The auxetic effects of these structures are achieved through the wrapping or unwrapping of the ligaments around the nodes in response to an applied force [231]. Another typical auxetic structure is the re-entrant structure consisting of periodical connected re-entrant polygonal units (Figure 9.1b). The interior angles of the polygon with values more than  $180^\circ$  are defined as negative angles. By changing the number of polygonal edges and negative angles, several other 2D re-entrant structures evolve. The auxetic effect of the re-entrant structures can be described as the following: when a uniaxial tensile load is applied, the re-entrant edges are subjected to bending and pulling simultaneously, leading to volume expansion in both axial direction and transversal directions [232]. The rotating rigid structures are another type of auxetic structure that are formed by rigid geometric units connected by hinges in their corners (Figure 9.1c). When stretching, the geometries rotate around the hinges, generating expansion in both axial and transversal directions, namely auxetic response. The shape of the rotating unit changes the value of Poisson's ratio.

Compared to conventional positive Poisson's ratio structures, the unusual behaviour of auxetic structures gives the material special mechanical characteristics and deformation modes that makes them superior for use in automotive, aerospace, sports, and marine applications [233] [234] [235] [236].

## 9.2 General properties of negative Poisson's ratio materials

Poisson's ratio of the auxetic structures assumes a negative value when stressed. Considering a re-entrant cell (Figure 9.2), its geometrical parameters can change the sign of Poisson's ratio from negative to positive when auxetic honeycombs bear a Y-direction tensile loading or an X-direction compressive loading. In detail, at high strain, the magnitude of Poisson's ratio decreases when the auxetic honeycomb is compressed in X-direction loading or stretched in Y-direction loading, while it increases when the auxetic honeycomb is stretched in X-direction loading or is compressed in Y-direction loading [209].

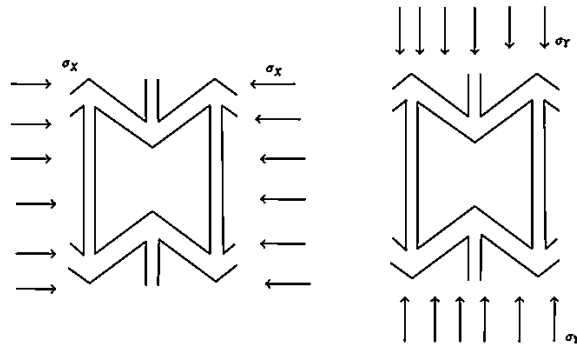


**Figure 9.2** Cell deformation by inclined cell member bending, loaded in X – direction (left), loaded in Y – direction (right).

Auxetic structures have attracted considerable interest not only for their unconventional behaviour under deformation but also because a negative Poisson's ratio gives material improved mechanical performance. According to classical elasticity theory, an auxetic character results in mechanical properties improvement compared to conventional materials such as increased indentation resistance, shear modulus, fracture toughness, energy absorption, and synclastic curvature [237]. These properties make auxetics

superior to conventional materials for many practical applications [228]. The behaviour of a material under impact deformation can be used to explain the improvement of the properties. Considering ad nonauxetic structures, the material immediately below the impact flows away in the lateral direction, leading to a reduction in density, unlike in an auxetic structure, material flows into the vicinity of the impact as a result of lateral contraction accompanying the longitudinal compression due to the impacting object (Figure 9.3). In other words, an auxetic material densifies under the impact, leading to increased indentation resistance compared to conventional materials [238]. In detail, indentation resistance is closely related to material hardness ( $H$ ), and the relationship between hardness and Poisson's ratio ( $\nu$ ) can be expressed as [239]:

$$H \propto \left[ \frac{E}{1 - \nu^2} \right]^r \quad (9.1)$$

From Equation (9.1), the indentation resistance tends to infinity, with the value of  $\nu$  approaching  $-1$ . The characteristic of indentation resistance can be broadly applied in protective devices, such as bulletproof and impact resistance equipment.

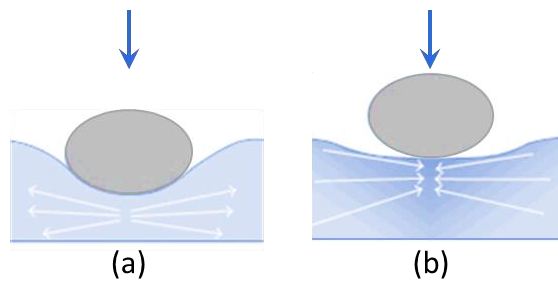


**Figure 9.3** Indentation resistance of nonauxetic (a) and auxetic (b) materials.

Shear strength improvement represents another important property of auxetic structures [240]. In the classical theory of elasticity for 3D isotropic materials, elastic behaviour can be described by two of four mechanical parameters: Young's modulus ( $E$ ), shear modulus ( $G$ ), bulk modulus ( $K$ ), and Poisson's ratio ( $\nu$ ). The relationships are given by:

$$G = \frac{3K(1-2\nu)}{2(1 + \nu)} \quad (9.2)$$

$$G = \frac{E}{2(1 + \nu)} \quad (9.3)$$

From Equation (9.3), the shear modulus increases with the decreasing Poisson's ratio. Thus, decreasing the Poisson's ratio is an effective way to enhance shear resistance. If the Poisson's ratio is close to -1, the shear modulus will tend to infinity, indicating that the material is easily compressed, but almost no shear deformation occurs. Fracture resistance is another property enhanced by auxetic behaviour. Under tensile load, the material expands suppressing the crack propagation [241]. Due to the porosity and counterintuitive deformation mechanism, auxetic structures have outstanding superiority in energy absorption and impact resistance, which can be designed for vibration reduction and isolation equipment [242].

### **9.3 Additive Manufacturing: the optimal manufacturing method for auxetic structures**

The identification of optimal manufacturing methods to realize auxetic structures is a critical point for experimental validation of the otherwise theoretical predictions. In the recent past, additive manufacturing (AM) emerged as a viable means to produce relatively more complex shapes with a variety of materials, including metals and polymers [243] [244] [245]. AM techniques are known to cater to a wide variety of specifics that subtractive manufacturing techniques fail to provide. These include lower wastages, faster fabrication, fabrication of complex and precise geometries, considerable energy savings, consolidated part fabrication, and easier design iterations, among many others. Therefore, additive manufacturing holds the potential to help fabricate and develop auxetic structures with improved properties and multifunctional capabilities. As opposed to conventional processes such as braiding, moulding, sintering, and spinning, AM indeed offers substantial flexibility and versatility to produce these structures.

Fused deposition modeling (FDM) is an additive manufacturing technique of polymers that has attracted attention over the last years due to its potential for reinventing the design process. A thermoplastic material filament is heated at a temperature close to the melting point and deposited through a nozzle on a surface in a layer-by-layer mode [246] [247]. This technique can be used to fabricate geometrically complex parts and prototypes with the benefit to reduce the cycle time and cost compared to

the traditional manufacturing process [248]. This AM technique has been used extensively in realizing polymer and polymer composite parts. However, modern printers have advanced to include the printing of metallic structures as well. Numerous studies have demonstrated the possibility to create structures with auxetic behaviour using the FDM technique [249]. In particular, the improvement of the auxetic behaviour is possible through process parameter optimizations and defects and geometric inconsistencies minimizations [250].

# 10

## Design of rotating rigid structures: flat vs. curved surfaces

### 10.1 Concept and design

The rotating rigid structures based on squares [228], triangles [251], cubes [252], and others are one of the most important classes of auxetic structures due to the relative ease and simplicity through which these systems may be produced. Specific perforation patterns in a conventional or positive Poisson's ratio material [253] allow to obtain rotating rigid structures of different geometry with the potential to exhibit auxetic behaviour. The common characteristic of the perforation patterns resulting in "rotating quadrilaterals" proposed so far is that each large segment of material is surrounded by four cuts placed in such a manner as to achieve a rotational symmetry and thus form a rotating unit. Hence, all these systems are made up of an alternating pattern of perforations with each cut having a certain orientation to the one directly next to it. The material at the region connecting the square units together acts as a 'joint'. These regions absorb the bulk of stress concentrations within the system whilst allowing the rotating units to rotate in a quasi-rigid manner, and therefore, besides the shape of the rotating unit, the effectiveness of the mechanism is also determined by the dimensions of this region. The dimensions and orientation variation of the perforations produces systems with rotating rigid units of different geometry. For example, square units are obtained using equal perforations perpendicularly arranged to one another. Removing the congruence constraint and using two perforations of unequal size, the remaining material takes a rectangular shape. On the other hand, if the perpendicularity constraint is removed and the orientation angle is varied, the rotating units formed have a rhombic shape. Finally, if both geometric constraints are removed, the resultant system is made up of two sets of unevenly sized parallelogram units [254]. The design versatility of the rotating rigid structures can lead to a wide number of auxetic geometries with the potential to exhibit a wide range of mechanical properties.

The mechanical properties of rotating rigid structures were analysed in numerous studies focusing on perforated flat surfaces with different perforation patterns. To assess the potential auxetic behaviour of perforated curved surfaces, rotating rigid structures with flat and curved surfaces were compared in this chapter. The profile of the perforated curved slab is formed by two equal and opposite consecutive circular arcs with an amplitude of  $90^\circ$ , inner radius  $r_2$ , and outer radius  $r_1$  (Figure 10.1a). The complete profile is obtained by repeating the geometry described above symmetrically. The perforated flat slab is characterized by a thickness  $t$  equal to the difference of the two radius,  $t = r_1 - r_2$  (Figure 10.1b). Equal diamond perforations perpendicularly arranged to one another were used as a perforated pattern to obtain rotating rigid square units. The geometric dimensions of these systems may be defined in terms of the perforation dimensions as shown in Figure 10.1c. These include the side of diamond perforations ( $l$ ), the angle between the side and the minor diagonal of the diamond perforations ( $\theta$ ), and the length of the spacing between the corners of two adjacent perforations ( $s$ ). The geometric parameters of the curved slab can be described as a function of the perforation pattern parameters and the thickness  $t$ , according to the following expressions:

$$r_2 = \frac{l \cos \theta + l \sin \theta + s - t}{2} \quad (10.1)$$

$$r_1 = \frac{l \cos \theta + l \sin \theta + s + t}{2} \quad (10.2)$$

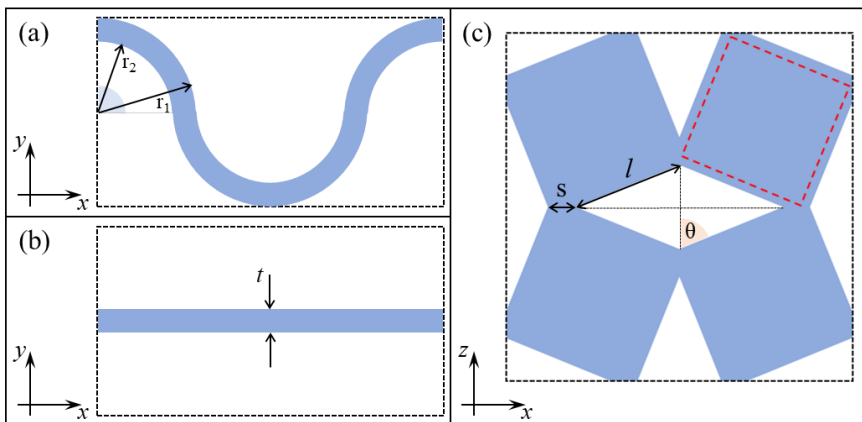


**Figure 10.1** Profile of the (a) curved and (b) flat slab in x- and y-directions. Parameters used to define the diamond perforated systems studied (c).

## 10.2 Methodology

The mechanical properties of the perforated systems described in Section 10.1 were analysed by performing a range of finite-element simulations using the ANSYS 13 software [255]. SOLID187 element under plane-stress conditions was used to mesh the structures. In detail, SOLID187 is a higher order 3D, 10-node element having a quadratic displacement behaviour and three degrees of freedom at each node (translations in the nodal  $x$ ,  $y$ , and  $z$  directions). It is well suited to modeling irregular meshes. The two systems were simulated as  $1 \times 1$  unit cells (Figure 10.1c) using periodic boundary conditions. As one can see from Figure 10.1c, the  $1 \times 1$  unit cell used for the perforated systems studied here is designed in such a manner that the four sides of the cell contain four rotating square units. According to the method described by Mizzi et al. [256], the boundary conditions were set using displacement constraint equations on the nodes at the edges of the unit cell. The Poisson's ratios and Young's moduli of the analysed systems were found by applying a tensile force on the edge nodes in  $x$ - and  $z$ -directions separately and measuring the resultant displacement of these nodes. These constraints and loading conditions ensure that the systems can deform freely without undergoing rigid-body motion whilst retaining their periodicity and unit cell alignment. The mesh size used to study the systems was identified by performing mesh convergence testing. The mesh level and depth were set equal to 3 for the curved system and equal to 2 for the flat system. The material properties of the system were set considering the mechanical behaviour of a 3D-printed PLA sample under tensile stress: Poisson's ratio equal to 0.45 and Young's modulus equal to 1600 MPa. In order to investigate the mechanical properties of the curved and flat systems, a range of perforated diamond patterns with the parameters shown in Table 10.1, whenever physically realisable, were considered and then simulated under the effects of an applied tensile force.

**Table 10.1** Parameters of the perforated diamond pattern.

Parameters	Values
$l$ [mm]	20, 40, 60, 80, 100, 120, 140
$t$ [mm]	5, 10, 15
$s$ [mm]	0.5, 1, 2
$\theta$	$20^\circ$ , $30^\circ$ , $40^\circ$

In detail,  $l$  values must respect the following relation in order to have a positive  $r_2$  value:

$$l > \frac{t-s}{\cos\theta+\sin\theta} \quad (10.3)$$

After this initial set of linear simulations which were used to elucidate the mechanical properties of these systems under small strain conditions, further simulations using nonlinear geometric analysis were performed on the two structures in order to determine whether the properties obtained for the linear simulations are retained over significant strain ranges.

### 10.3 Linear FE analysis

The linear mechanical properties of the analysed systems were evaluated by separately applying a tensile force in  $x$ - and  $z$ -directions. In detail, Young's modulus and Poisson's ratios of the samples at different thicknesses were evaluated by varying the geometric dimensions of the perforation pattern. The application of a tensile load in  $xz$ -plane submits the analysed systems to the deformation shown schematically in Figure 10.2. This deformation mechanism can be described as a “rotating units” mechanism [254].

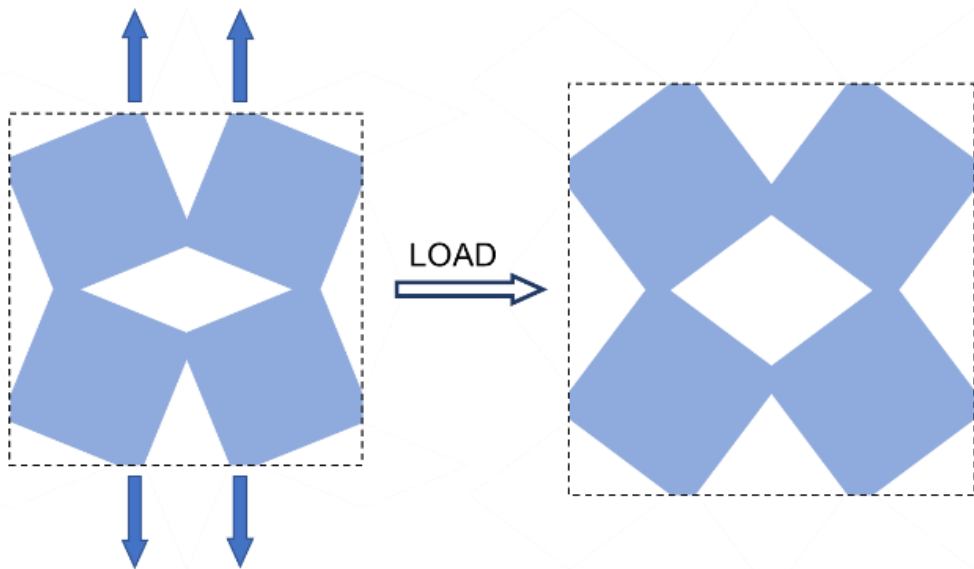


**Figure 10.2** Schematic representation of the deformation mechanism in the  $xz$ -plane of the analysed structures.

The linear simulation results of the systems subjected to tensile force in the  $x$ -direction are summarised in Figure 10.3 for the flat system and Figures 10.4 and 10.5 for the curved system. The linear mechanical properties of the flat system show a significant dependence on the geometric parameters of the perforation pattern (Figure 10.3), while no change was noticed with the structure thickness variation. In detail, Young's modulus,  $E_x$ , decreases with  $l$  and grows by increasing the separation length and the angle of the diamonds. The Poisson's ratio,  $\nu_{xz}$ , is generally constant to -1 and shows relevant variation only for  $\theta=40^\circ$ . In the latter case, the smallest values of  $\nu_{xz}$  are recorded when the  $l$  increases and  $s$  decreases. Lastly,  $\nu_{xy}$  does not change with the geometric parameters and remains constant at 0.

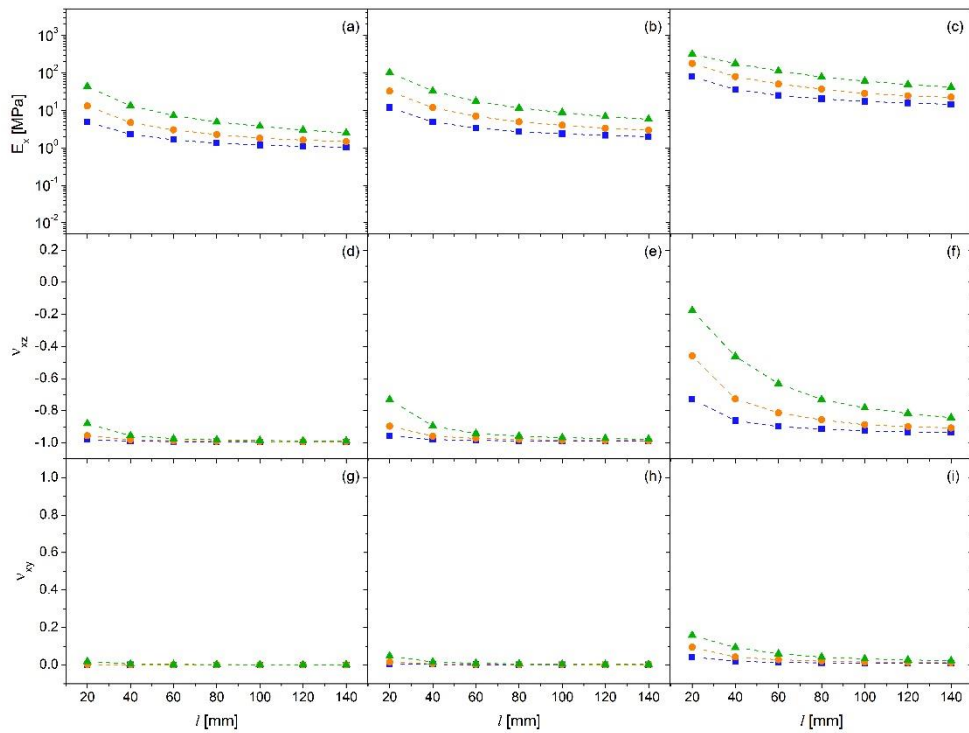


**Figure 10.3** Variation of  $E_x$  and  $\nu_{xz}$  with the side of diamond perforations,  $l$ , for the flat system at  $t=10$  mm. Different separation lengths ( $s=0.5$  mm (■),  $s=1$  mm (●), and  $s=2$  mm (▲)) and angles ( $\theta=20^\circ$  (a, d, g),  $\theta=30^\circ$  (b, e, h), and  $\theta=40^\circ$  (c, f, i)) of the perforation pattern are considered. The lines are guides for the eye.

The linear mechanical properties of the curved system show a relevant dependence on both the geometric parameters of the perforation pattern

(Figure 10.4) and the structure thickness (Figure 10.5). Young's modulus,  $E_x$ , reveals a decreasing trend with  $l$  and a negligible dependence on the  $s$  and  $\theta$  parameters. On the contrary, Poisson's ratios,  $\nu_{xz}$  and  $\nu_{xy}$ , show a growing trend with the diamond perforation side and tend to a constant value for high  $l$  values (i.e., 0 in  $xz$ -plane and 0.8 in  $xy$ -plane). In addition, the separation length increase causes a vertical shift of the Poisson's ratios in systems with  $\theta=20^\circ$  and  $30^\circ$ . A relevant effect of thickness is recorded for the curved system. The change in linear mechanical properties at different values of  $t$  is summarized in Figure 10.5 for  $s=0.5$  and  $\theta=20^\circ$ . The results show that increasing thickness causes an increase in stiffness and a decrease in Poisson's ratios of the structure.

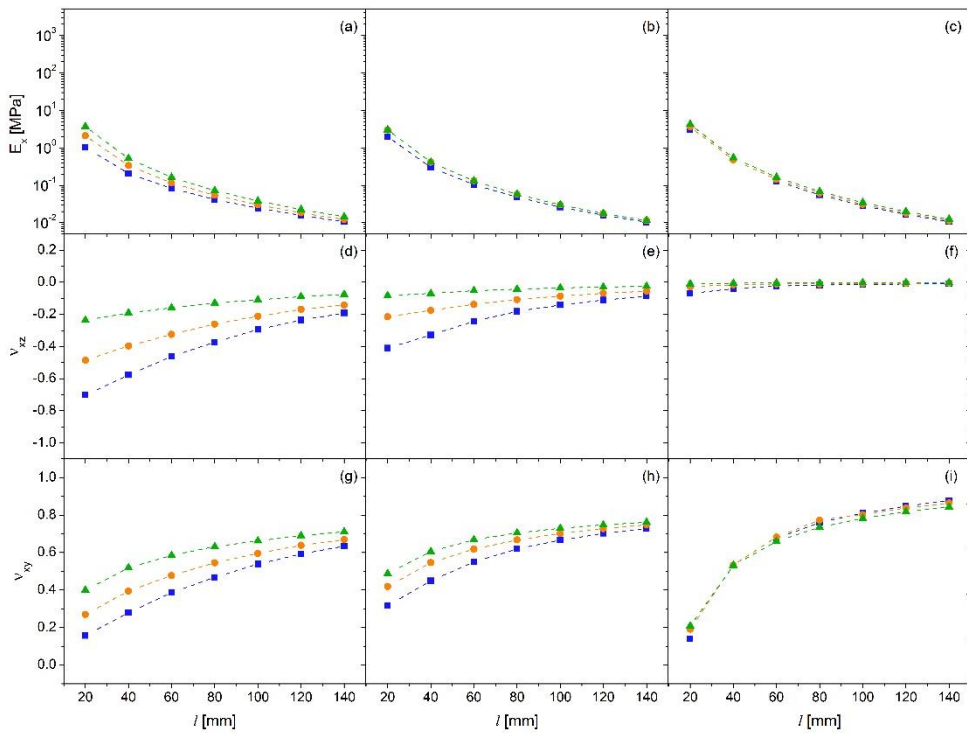


**Figure 10.4** Variation of  $E_x$ ,  $\nu_{xz}$  and  $\nu_{xy}$  with the side of diamond perforations,  $l$ , for the curved system at  $t=10$  mm. Different separation lengths ( $s=0.5$  mm (■),  $s=1$  mm (●), and  $s=2$  mm (▲)) and angles ( $\theta=20^\circ$  (a, d, g),  $\theta=30^\circ$  (b, e, h), and  $\theta=40^\circ$  (c, f, i)) of the perforation pattern are considered. The lines are guides for the eye.

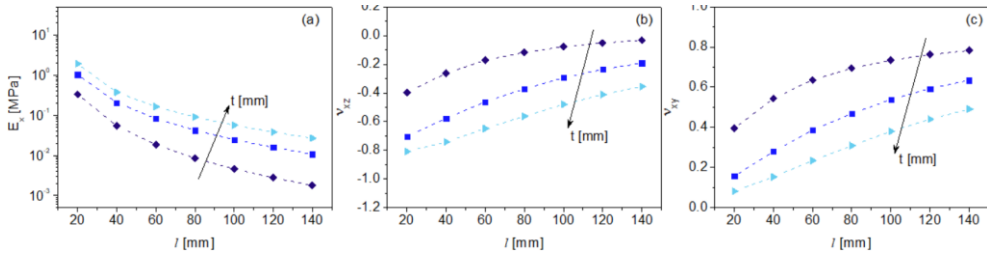


**Figure 10.5** Variation of  $E_x$  (a),  $v_{xz}$  (b) and  $v_{xy}$  (c) with the side of diamond perforations,  $l$ , for the curved system with different separation values:  $t=5$  mm ( $\blacklozenge$ ),  $t=10$  mm ( $\blacksquare$ ) and  $t=15$  mm ( $\blacktriangleright$ ). Angle  $\theta=20^\circ$  and separation length  $s=0.5$  are considered. The lines are guides for the eye.

Relevant differences can be observed by comparing the two systems. Young's modulus  $E_x$  reaches significantly lower values in curved systems than in flat systems. For example,  $E_x$  goes from 4.7 MPa in the flat system to 0.3 MPa in the curved system for geometric parameter values of  $t=5$  mm,  $l=20$  mm,  $s=0.5$ , and  $\theta=20^\circ$ . Instead, both the systems exhibit a negative Poisson's ratio in the  $xz$ -plane, but only the flat structure reaches the minimum value of  $-1$ . As expected, the curvature presence generates a reduction in the stiffness and auxeticity of the analysed structure.

The tensile force application in the  $z$ -direction generates a different mechanical behaviour only for the curved system while equal results in both directions were recorded for the flat system as a consequence of structural symmetry. Figure 10.6 shows the linear mechanical properties of the curved system subjected to tensile force in the  $z$ -direction. Young's modulus,  $E_y$ , decreases with  $l$  and shows a relevant dependence on  $s$  and  $\theta$  whose increase causes an improvement in the structure stiffness. The Poisson ratios,  $v_{zx}$  and  $v_{zy}$ , show an increasing and a decreasing trend respectively with  $l$ . In both cases, negative values of the Poisson's ratio are recorded, which indicate an auxetic behaviour in both  $xy$  and  $xz$ -planes when the structure is loaded along  $y$ -direction.

In conclusion, the linear simulation showed that both systems assume an auxetic behaviour in the  $xz$ -plane, i.e., where the rotating rigid units were built, while along the  $xy$ -plane this behaviour was detected only for the curved structure subjected to tensile force in the  $z$ -direction.

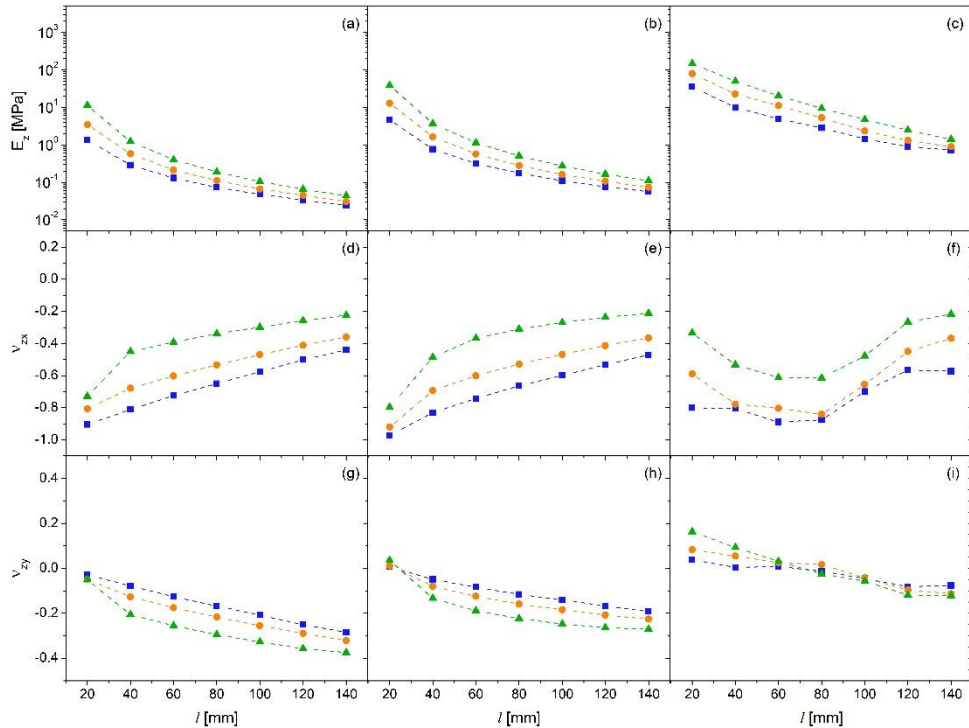


**Figure 10.6** Variation of  $E_z$ ,  $v_{zx}$  and  $v_{zy}$  with the side of diamond perforations,  $l$ , for the curved system at  $t=10$  mm. Different separation lengths ( $s=0.5$  mm (■),  $s=1$  mm (●), and  $s=2$  mm (▲)) and angles ( $\theta=20^\circ$  (a, d, g),  $\theta=30^\circ$  (b, e, h), and  $\theta=40^\circ$  (c, f, i)) of the perforation pattern are considered. The lines are guides for the eye.

## 10.4 Nonlinear FE analysis

The results obtained from the linear simulations indicate that the two systems have the potential to exhibit negative Poisson's ratios, one may argue that these values may not necessarily be retained over a significant strain range. Moreover, rotating unit systems typically have a threshold above which they cannot deform any longer via rotation upon the application of strain. Thus, it is important to obtain an indication of the nonlinear geometric behaviour of these systems over large strains in order to assess the extent to which the auxetic characteristics of the system remain present during deformation. In view of this, additional simulations using nonlinear geometric analysis were performed on the two analysed systems. In detail, the structure thickness and the geometric parameters of the

perforation pattern have been selected considering their possible printability with 3D printing techniques.

In Figure 10.7, the changes in Poisson's ratio with increasing engineering strain are presented for flat and curved systems at  $t=20$  mm,  $s=0.7$  mm,  $t=5$  mm, and  $\theta=20^\circ$ . These results are presented in terms of the instantaneous Poisson's ratio which takes into account the changes in strains in terms of increments rather than relative to the initial dimensions of the system only [8]. As a result of this, any changes in the deformation mechanism and/or sign switching of the Poisson's ratio may be more easily detected from the plot [9] [10].

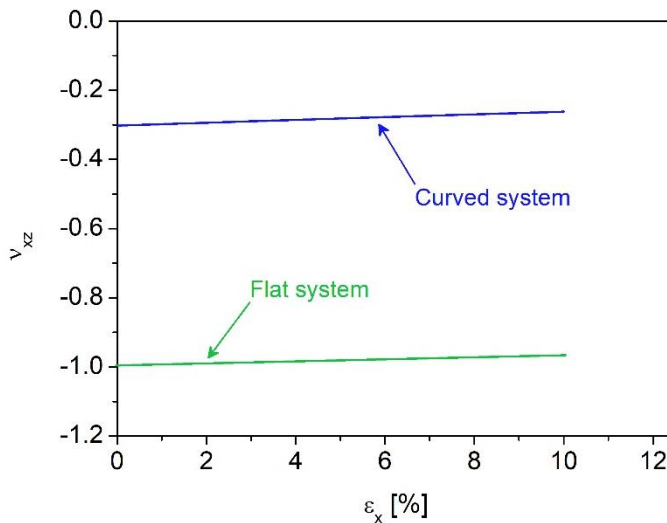


**Figure 10.7** Results of the nonlinear analysis for flat (blue) and curved (green) systems with the parameters  $t=20$  mm,  $s=0.7$  mm,  $t=5$  mm, and  $\theta=20^\circ$ .

As can be seen from Figure 10.7, the nonlinear FE analysis suggests that the two systems have the potential to maintain their auxeticity up to considerable strains. In fact, the flat system retains a Poisson's ratio of ca. -1 while the curved system retains a Poisson's ratio of ca. -0.3 for up to a tensile strain of 10%. Therefore, some combinations of parameters generate systems that exhibit highly auxetic behaviour maintained at high stresses.

## 10.5 Fabrication of an auxetic sample prototype by 3D printing

To validate the results obtained with the nonlinear FE analysis, a prototype sample of the curved system was produced and subjected to experimental investigations. A 3D printing process, Fused Filament Fabrication (FFF), was used to fabricate the experimental specimens. FFF is an additive manufacturing technique through which physical components are fabricated layer-by-layer. In this printing technology, thermoplastic filaments for both model and support are fed into the heated extrusion print head, enabling three-dimensional (3D) dispensing of the resulting polymer melts on a platform, which is lowered step-by-step once each object's layer is completed. Layer by layer, the object is then printed. The printing process is controlled by many parameters, which range from material filament type to several machine settings.

A 3x3 unit cell prototype of the curved auxetic structure at  $t=20$  mm,  $s=0.7$  mm,  $t=5$  mm, and  $\theta=20^\circ$  was designed and manufactured using polylactic acid as material (Figure 10.8). A supporting material was used to ensure a good printing result. The printed sample for mechanical testing was obtained using the Ultimaker S5 printer with the optimized printing parameters reported in Table 10.2.

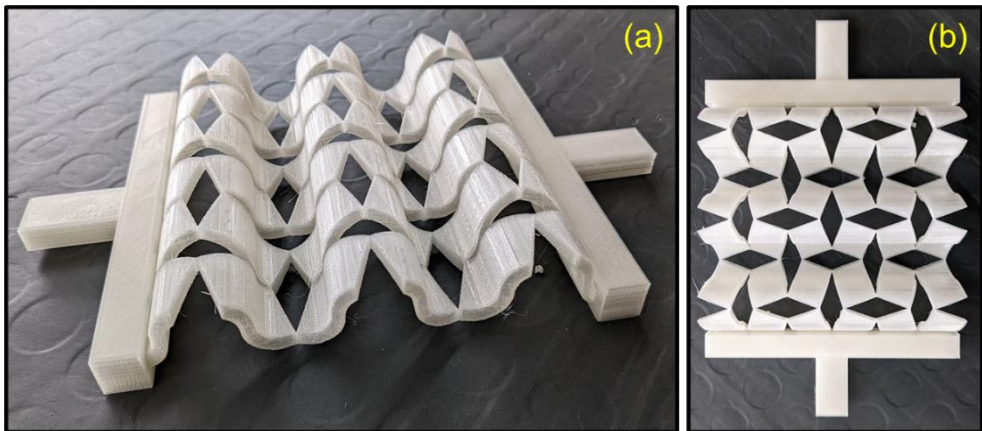


**Figure 10.8** 3x3 unit cell prototype of the curved auxetic structure: (a) 3D view and (b) frontal perspective.

**Table 10.2** Ultimaker S5 printing parameters for the PLA auxetic sample.

Printing parameter	Value	Unit
Nozzle diameter	0.25	mm
Wall thickness	0.8	mm
Wall line count	2	-
Layer thickness	1	mm
Infill	100	%
Raster angles	60	deg
Printing temperature	200	°C
Plate temperature	60	°C
Print speed	70	mm/s
Fan speed	100	%

## 10.6 Experimental mechanical testing of 3D printed auxetic structures

The sample prototype created with 3D printing were experimentally tested under tensile loading to investigate their auxetic response. The sample was characterized using an Instron 5985 universal testing machine (Instron, Milan, Italy) equipped with a 10 kN load cell, in strain control mode at a speed of  $1 \mu\text{m min}^{-1}$ . Figure 10.9 shows the experimental setup. The mechanical test was repeated three times to ensure the repeatability of the recorded measurements.

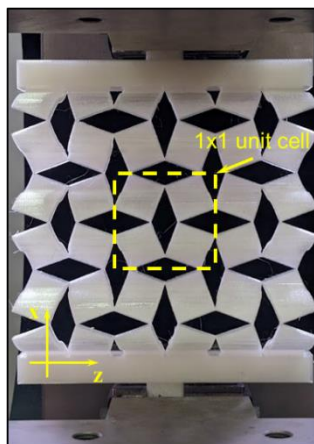


**Figure 10.9** Experimental setup. The 1x1 unit cell analysed is reported in the square.

To validate the nonlinear FE analysis results, Poisson's ratio  $\nu_{xz}$  of the central 1x1 unit cell of the sample prototype (see the yellow square in Figure 10.9) was measured. The successive increments of the displacements during the mechanical test were captured by a digital camera and the images were analysed using an image processing software (ImageJ). Before the test, a set of black markers were painted at the ends of the 1x1 unit cell to facilitate their identification. The strain is defined to be  $\varepsilon = L(t)/L_0$ , where  $L(t)$  is the change in displacement of the 1x1 unit cell ends, and  $L_0$  is the original length of the cell. To evaluate the Poisson's ratio  $\nu_{xz}$ , the strain of the central 1x1 unit cell was calculated in the direction of the load ( $\varepsilon_x$ ) and in the direction perpendicular to the load ( $\varepsilon_z$ ).

The comparison of the experimental test and nonlinear FE analysis results for the curved sample at  $t=20$  mm,  $s=0.7$  mm,  $t=5$  mm, and  $\theta=20^\circ$  are summarized in Figure 10.6. The experimental measurements of transversal strain and Poisson's ratio are in reasonable agreement with the predictions of nonlinear FE analysis.

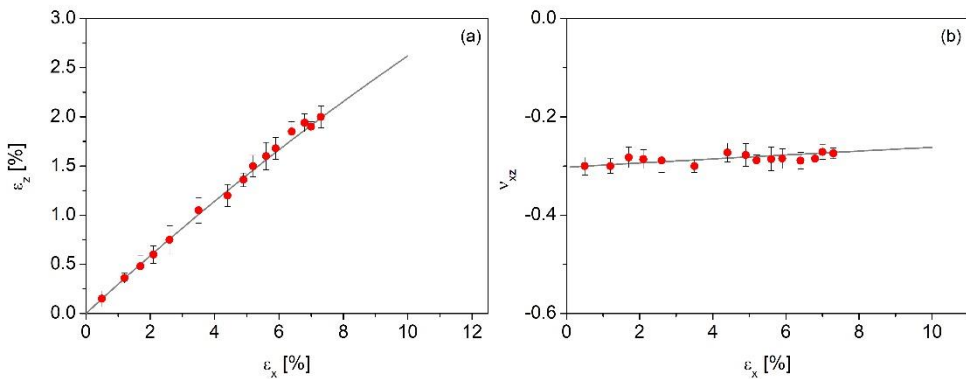
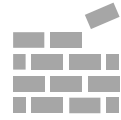


**Figure 10.6** Transversal strain  $\varepsilon_z$  (a) and Poisson's ratio  $\nu_{xz}$  (b) variation as a function of applied strain  $\varepsilon_x$  obtained by the experimental analysis (circles) and nonlinear FE analysis (line).





## Conclusions

Biopolymers have gained an increasing interest during the past decade as a possible solution to reduce the dependence on non-renewable (or not totally renewable) materials. The inherent advantage of this polymer class is that they can be produced from renewable resources and, more important, they can be biodegradable or compostable. The latter point is highly desirable, but the kinetics of the degradation in the natural environment must be fast to ensure actual environmental sustainability. In this context, the first goal of the research activity was the study of the pro-degradative effects of short natural fibers on a host biodegradable polyester matrix, i.e., polylactic acid, to speed up biodegradation while preserving the material eco-friendly nature.

The polylactic acid biodegradation phenomenon involves the hydrolysis of the ester groups in the main chain of the polymer prior to mineralization by microorganisms. Due to their inherent hygroscopic features, natural fibers play a crucial role in this process favoring the access of water molecules from the external environment. Several fiber-related parameters concur in defining the biodegradation kinetics of these green composites such as fiber composition, geometry, and volume fraction. Particular attention was placed on the fiber content since the pro-degradative effect is expected to increase when the percolation threshold ( $\Phi_c$ ) is exceeded, i.e., when the fibers touch each other offering easy access for water and other pro-degradative species to enter from the host environment and reach the inner parts of the composite. In the first part of the study, the percolation threshold of short hemp shive and kenaf bast fibers was assessed in PLA-based composites by means of (i) theoretical calculations grounded on the excluded volume percolation theory, (ii) linear viscoelastic analyses in the melt state, and (iii) dielectric spectroscopy, and the efficacy of the three methods were compared. Excluded volume percolation theory requires accurate knowledge of fiber geometry (size, shape, aspect ratio) and space orientation. Both parameters are difficult to estimate in practical cases. As a result, only a (wide) range of possible values of  $\Phi_c$  was derived by this theoretical approach. Regarding the rheological estimate of  $\Phi_c$ , a previously

derived viscoelastic model for polymer nanocomposites was extended to the studied systems, validating it through the building of a master curve of the elastic modulus of samples above percolation. The latter made it possible to narrow the range in which looking for  $\Phi_c$ , which was finally identified by invoking the percolation theory. The procedure led to  $\Phi_c \sim 10.1$  and  $19.5$  vol.% for the hemp- and kenaf-based composite, respectively. Lastly, the results were confirmed by means of dielectric spectroscopy analyses.

After identifying the percolation threshold, the degradation process of the PLA-based composites loaded with hemp shive and kenaf bast fibres was estimated under different conditions: (i) degradation phenomena in melt state, (ii) hydrolytic degradation in water, and (iii) biodegradation in compost. The degradation phenomena in the melt state were studied through a simple rheometric protocol consisting of repeated frequency scans. This method allowed to monitor the degradation kinetics by observing changes in the rheological functions. The zero-frequency complex viscosity reflects the reduction of the average molecular weight of the polymer. By monitoring the time evolution of this parameter, it was founded that the fibres significantly speed up degradation in the melt state. The pro-degradative effect of the natural fibres can be associated with the presence of water molecules bound to hydroxyl groups of natural fibres which trigger the hydrolytic degradation of PLA. The evaluation of the degradation in the melt state was possible only for the samples below  $\Phi_c$  since the formation of a continuous fibre network deviates the complex viscosity trend from that provided by the Carreau-like equation. The hydrolytic degradation tests performed by water soaking at  $45^\circ\text{C}$  of samples at different natural fibre contents revealed the effect of the percolation threshold on the degradation process of PLA-based green composites. The PLA hydrolytic process is a two-stage mechanism. In the first stage, the water molecules attack ester groups in amorphous regions triggering a crystallinity degree increase. In the second stage, also the crystalline regions undergo hydrolysis, and the crystallinity degree decrease is recorded. A reduction of the matrix crystallinity degree was only observed in samples above the percolation threshold after 50 days of immersion in water. The formation of a hygroscopic fibre network into the polymeric matrix produces an increase in the hydrolytic degradation rate. The results were confirmed by means of dynamic mechanical thermal analyses. The fiber content increase triggers a greater loss of viscoelastic properties during the water soaking with an increase in the variation rate of the rubbery modulus above the percolation threshold. To validate the results obtained, the matrix molecular weight after 50 days in water was evaluated and the pro-degradative effect of the natural fibres was confirmed. The biodegradation process in compost of PLA-based

composites loaded with hemp shives fibres was evaluated to estimate the green composites behaviour in real conditions. The nucleating effect of natural fibres led to an increase in matrix crystallinity degree during the manufacturing process. The higher crystallinity of the green composites caused a slowdown of the biodegradation process after 10 days in compost. After 40 days, the pure PLA and composite systems showed molecular weight distributions not only shifted toward sufficiently low values to release water-soluble fractions into the compost but also to allow final mineralization.

A cradle-to-gate life cycle assessment study of PLA loaded with natural fibres derived from naturally grown pine needles or cultivated kenaf feedstocks was performed to validate the eco-friendly nature of the green composites. The environmental impact of the composites, derived by combining the impacts of polymer and fillers and adding the contribution of the melt mixing process, is far lower than that of neat PLA. The higher the fibre content, the higher the benefits. The reason is that the fibres have a negligible environmental burden compared to the polymer matrix, hence replacing “high-impact” PLA with “low-impact” natural fibres is always preferable. Further environmental benefits come from the enhanced properties with respect to neat PLA. A stiffness-limited design of a panel proves that using green composites instead of neat PLA leads to a material saving up to 8%.

In the last part of the dissertation, the potential of auxetic mechanical metamaterials was explored to generate biodegradable materials with innovative mechanical characteristics. The auxetic behaviour of diamond perforated systems with flat and curved surfaces were investigated using a fine element approach. The results obtained showed that both systems have the potential to exhibit negative values of the Poisson’s ratios which were retained over a significant tensile strain range. In the end, a prototype of the curved system created with 3D printing was experimentally tested under tensile loading to investigate their auxetic response. The experimental measurements of Poisson’s ratio are in reasonable agreement with the predictions of nonlinear FE analysis.









# Appendix

## A.1 Human toxicity and ecotoxicity potentials for PN and KB production

Fertilizers and agricultural facilities such as diesel are among the main contributors to the environmental impact for the human toxicity and ecotoxicity categories for kenaf fibre, while the electric energy use has the highest relative contribution for pine needles in the same indicators.

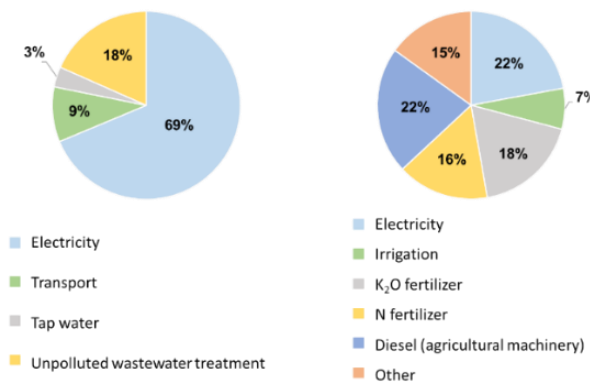


**Figure A.1** Relative contributions to 100-year human toxicity potential (HTP) for pine needles (left) and kenaf fibres (right) production at the gate.

Nitrogen fertilizer accounts for 16% of the Human toxicity indicator (Figure A.1), while K<sub>2</sub>O is responsible for 18%, reaching a total contribution of 34% at least. The effects of the soil pH raising agent (about 1%) have been aggregated under the “Other” label, as well as the other emissions whose value is less than the smallest of the reported main contributors. A similar result can also be observed in the remaining ecotoxicity categories, although the relative weights for each fertilizer can vary depending on the impact factor assigned to the targeted chemical agent

towards the impact category under analysis. As an example, as far as the terrestrial ecotoxicity potential (Figure A.2) is concerned, the  $K_2O$  fertilizer accounts for 40% of the total impact, while  $P_2O_5$  and urea ammonium nitrate account for 26% and 5% respectively.

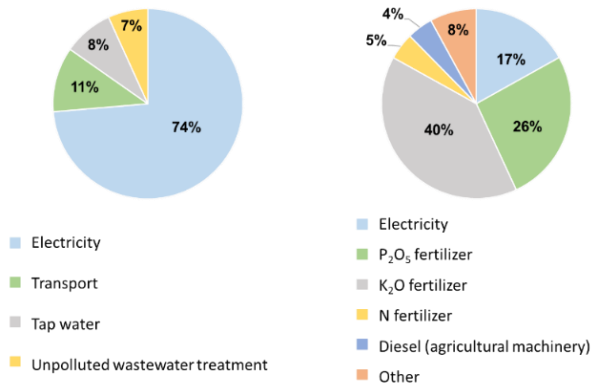


**Figure A.2** Relative contributions to 100-year terrestrial ecotoxicity potential (TETP) for pine needles (left) and kenaf fibres (right) production at the gate.

The impact categories of ecotoxicity have shown to be dependent on the use of agricultural machinery: as for marine aquatic ecotoxicity potential (Figure A.3) and freshwater aquatic ecotoxicity (Figure A.4), its contribution is equal to 8% for each of the indicators.

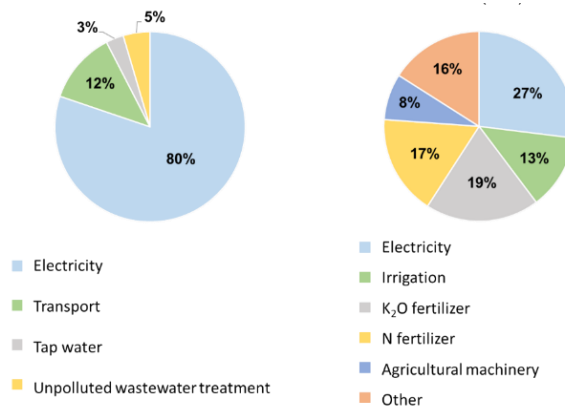


**Figure A.3** Relative contributions to 100-year marine aquatic ecotoxicity (MAETP) for pine needles (left) and kenaf fibres (right) production at the gate.

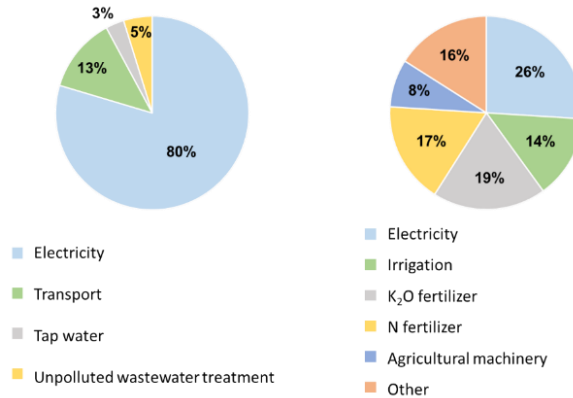


**Figure A.4** Relative contributions to 100-year freshwater aquatic ecotoxicity (FAETP) for pine needles (left) and kenaf fibres (right) production at the gate.

The electricity used for processing kenaf fibre contributes to the human toxicity and eco-toxicity categories for percentages between 17 and 27%, while it is the greatest source of environmental impact for pine needles. Indeed, it represents the 69% of the human toxicity potential (Figure A.1), the 74% of the terrestrial ecotoxicity potential (Figure A.2) and approximately 80% of the marine aquatic ecotoxicity potential (Figure A.3).

Therefore, the toxicity of this alternative natural fibre is highly dependent on the energy efficiency of the process and appears to have better room for improvement over kenaf or any other natural fibre, as it is free from the use of chemicals, irrigation water and other resources used for sowing and cutting the crops.









## *References*

- [1] R. Jones, *Mechanics of composite materials*, Blacksburg, Virginia: CRC press, 1998.
- [2] *ASTM D3878 – 07: Standard Terminology for Composite Materials*, 2013.
- [3] I. Daniel, O. Ishai, *Engineering mechanics of composites materials*, 2nd ed., USA: New York: Oxford university press, 2006.
- [4] F. Campbell, *Structural composite materials*, USA: ASM international, 2010.
- [5] S. Bruckner, G. Allegra, M. Pegoraro, F. La Mantia, *Scienza e tecnologia dei materiali polimerici*, Napoli: EdiSES, 2001.
- [6] D. Rajak, D. Pagar, P. Menezes, E. Linul, «Fiber-Reinforced Polymer Composites: Manufacturing, Properties, and Applications», *Polymers*, 11 (10), 1-37, 2019.
- [7] A. Mohanty, M. Misra, L. Drzal, *Natural Fibers, Biopolymers, and Biocomposites*, CRC press, 2005.
- [8] F. La Mantia e M. Morreale, «Green composites: A brief review», *Composites: Part A*, 42, 579-588, 2011.
- [9] H. Abdul Khalil, A. Bhat, A. Ireana Yusra, «Green composites from sustainable cellulose nanofibrils: A review», *Carbohydrate Polymers*, vol. 87, 963-979, 2012.
- [10] E. Bioplastics, «Accountability is key: environmental communications guide for bioplastics», 2014» 04 06 2022. [Online]. Available: [www.european-bioplastics.org](http://www.european-bioplastics.org).

- [11] E. Zini, M. Scandola, «Green Composites: An Overview», *Polymer composites*, 32 (12), 1905-1915, 2011.
- [12] Z. Azwa, B. Yousif, A. Manalo, W. Karunasena, «A review on the degradability of polymeric composites based on natural fibres», *Materials and Design*, 47, 424-442, 2012.
- [13] O. Faruk, A. Bledzki, H. Fink, M. Sain, «Biocomposites reinforced with natural fibers: 2000–2010» *Progress in Polymer Science*, 37 (11), 1552-1596, 2012.
- [14] D. Ray, *Biocomposites for High-Performance Applications: Current Barriers and Future Needs Towards Industrial Development*, Cambridge: Elsevier Science, 2017.
- [15] A. McNaught, A. Wilkinson, IUPAC. *Compendium of Chemical Terminology*, 2nd ed. (the "Gold Book") a cura di, Chichester: Wiley - Blackwell, 1997.
- [16] «in PD CEN/TR 15351:2006,» *BSI*, p. 23, 2006.
- [17] N. Lucas, C. Bienaime, C. Belloy, M. Queneudec, F. Silvestre, J. E. Nava-Saucedo, «Polymer biodegradation: Mechanisms and estimation techniques – A review», *Chemosphere*, 73 (4), 429-442, 2008.
- [18] K. Leja, G. Lewandowicz, «Polymer Biodegradation and Biodegradable Polymers-a Review», *Polish Journal of Environmental Studies*, 19 (2), 255-266, 2010.
- [19] M. Hakkarainen, «Aliphatic polyesters: abiotic and biotic degradation and degradation products», *Advances in Polymer Science*, 157, 113-138, 2002.
- [20] G. Kister, G. Cassanas, M. Bergounhon, D. Hoarau, M. Vert, «Structural characterization and hydrolytic degradation of solid copolymers of D, L-lactide co- $\epsilon$ -caprolactone by Raman spectroscopy», *Polymer*, 41, 925-932, 2000.
- [21] C. Proikakis, N. Mamouzelous, P. Tarantili, A. Andreopoulos, «Swelling and hydrolytic degradation of poly(D, L-lactic acid) in

- aqueous solution» *Polymer Degradation and Stability*, 91 (3), 614-619, 2006.
- [22] D. Briassoulis, «The effects of tensile stress and the agrochemicals Vapam on the ageing of low density polyethylene (LDPE) agricultural films. Part I. Mechanical behaviour», *Polymer Degradation and Stability*, 86, 489-503, 2005.
- [23] D. Wiles, G. Scott, «Polyolefins with controlled environmental degradability», *Polymer Degradation and Stability*, 91, 1581-1592, 2006.
- [24] K. Pielichowski, J. Njuguna, Thermal degradation of polymeric materials, iSmithers Rapra Publishing, 2005.
- [25] T. Pierre, E. Chiellini, «Biodegradability of synthetic polymers used for medical and pharmaceutical applications: Part 1—principles of hydrolysis mechanisms», *Journal of bioactive and compatible polymers*, 1 (4), 467-497, 1986.
- [26] T. Haider, C. Volker, J. Kramm, K. Landfester, F. Wurm, «Plastics of the Future? The Impact of Biodegradable Polymers on the Environment and on Society», *Angewandte Chemie International Edition*, 58 (1), 50-62, 2019.
- [27] E. Castro-Aguirre, F. Iniguez-Franco, H. Samsudin, X. Fang, R. Auras, «Poly (lactic acid)—Mass production, processing, industrial applications, and end of life», *Advanced Drug Delivery Reviews*, 107, 333-366, 2016.
- [28] M. Karamanlioglu, R. Preziosi, G. Robson, «Abiotic and biotic environmental degradation of the bioplastic polymer poly(lactic acid): A review», *Polymer Degradation and Stability*, 137, 122-130, 2017.
- [29] S. Lyu, J. Schley, B. Loy, D. Lind, C. Hobot, R. Sparer, D. Untereker, «Kinetics and time-temperature equivalence of polymer degradation», *Biomacromolecules*, 8, 2301–2310, 2007.
- [30] R. Auras, L. Lim, S. Selke, H. Tsuji, Poly (lactic acid): synthesis, structures, properties, processing, and applications (Vol. 10),

Hoboken, New Jersey: John Wiley & Sons, 2011.

- [31] G. Gorrasi, R. Pantani, «Effect of PLA grades and morphologies on hydrolytic degradation at composting temperature: Assessment of structural modification and kinetic parameters», *Polymer Degradation and Stability*, 98, 1006-1014, 2013.
- [32] M. Elsayy, K. Kim, J. Park, A. Deep, «Hydrolytic degradation of polylactic acid (PLA) and its composites», *Renewable and Sustainable Energy Reviews*, 79, 1346-1352, 2017.
- [33] T. Kijchavengkul, R. Auras, «Compostability of polymers», *Polymer International*, 57 (6), 793-804, 2008.
- [34] Y. Tokiwa, B. Calabia, «Biodegradability and biodegradation of poly (lactide)», *Applied microbiology and biotechnology*, 72 (2), 244-251, 2006.
- [35] M. Itavaara, S. Karjomaa, J. Selin, «Biodegradation of polylactide in aerobic and anaerobic thermophilic conditions», *Chemosphere*, 46 (6), 879-885, 2002.
- [36] N. Teramoto, K. Urata, K. Ozawa, M. Shibata, «Biodegradation of aliphatic polyester composites reinforced by abaca fiber», *Polymer Degradation and Stability*, 86, 401-409, 2004.
- [37] A. Yussuf, I. Massoumi, A. Hassan, «Comparison of Polylactic Acid/Kenaf and Polylactic Acid/Rise Husk Composites: The Influence of the Natural Fibers on the Mechanical, Thermal and Biodegradability Properties», *Journal of Polymers and the Environment*, 18, 422-429, 2010.
- [38] G. Rajesh, A. Ratna Prasad, A. Gupta, «ScienceDirect Soil Degradation Characteristics of Short Sisal / PLA Composites», *Materials Today: Proceedings*, 18, 1-7, 2019.
- [39] R. Gunti, A. Prasad, A. Gupta, «Mechanical and Degradation Properties of Natural Fiber-Reinforced PLA Composites: Jute, Sisal, and Elephant Grass», *Polymer Composites*, 39 (4), 1125-1136, 2018.

- [40] T. Bayerl, M. Geith, A. Somashekar, D. Bhattacharyya, «Influence of fibre architecture on the biodegradability of FLAX/PLA composites», *International Biodeterioration & Biodegradation*, 96, 18-25, 2014.
- [41] H. Dhakal, Z. Zhang, M. Richardson, «Effect of water absorption on the mechanical properties of hemp fibre reinforced unsaturated polyester composites», *Composites science and technology*, 67 (7-8), 1674-1683, 2007.
- [42] M. Bredu, «Environmental degradation of plastic composites with natural fillers - A Review», *Polymers*, 12 (1), 166, 2020.
- [43] R. Malkapuram, V. Kumar, Y. Negi, «Recent development in natural fiber reinforced polypropylene composites», *Journal of reinforced plastics and composites*, 28 (10), 1169-1189, 2009.
- [44] N. Stevulova, J. Cigasova, A. Estokova, E. Terpakova, A. Geffert, F. Kacik, E. Singovszka, M. Holub, «Properties characterization of chemically modified hemp hurds», *Materials*, 7 (12), 8131-8150, 2014.
- [45] M. Poletto, H. Ornaghi Júnior, A. Zattera, «Thermal Decomposition of Natural Fibers: Kinetics and Degradation Mechanisms», *Reactions and Mechanisms in Thermal Analysis of Advanced Materials*, 515-546, 2015.
- [46] B. Koohestani, A. Darban, P. Mokhtari, E. Yilmaz, E. Darezereshki, «Comparison of different natural fiber treatments: a literature review», *International Journal of Environmental Science and Technology*, 16 (1), 629-642, 2019.
- [47] M. Poletto, A. Zattera, M. Forte, R. Santana, «Thermal decomposition of wood: Influence of wood components and cellulose crystallite size», *Bioresource Technology*, 109, 148-153, 2012.
- [48] C. Zhao, E. Jiang, A. Chen, «Volatile production from pyrolysis of cellulose, hemicellulose and lignin», *Journal of the Energy Institute*, 90 (6), 902-913, 2016.
- [49] K. Oksman, A. Mathew, R. Langstrom, B. Nystrom, K. Joseph, «The

influence of fibre microstructure on fibre breakage and mechanical properties of natural fibre reinforced polypropylene», *Composites science and technology*, 69, 1847-1853, 2009.

- [50] D. Puglia, A. Terenzi, S. Barbosa, J. Kenny, «Polypropylene–natural fibre composites. Analysis of fibre structure modification during compounding and its influence on the final properties», *Composite Interfaces*, 15, 111-129, 2008.
- [51] P. Hornsby, E. Hinrichsen, K. Tarverdi, «Preparation and properties of polypropylene composites reinforced with wheat and flax straw fibers», *Journal of Materials Science*, 32, 1009-1015, 1997.
- [52] A. Terenzi , J. Kenny, S. Barbosa , «Natural fiber suspensions in thermoplastic polymers. I. Analysis of fiber damage during processing», *Journal of Applied Polymer Science*, 103, 2501-2506, 2007.
- [53] F. Godard, M. Vincent, J. Agassant, B. Vergnes, «Rheological behavior and mechanical properties of sawdust/polyethylene composites», *Journal of Applied Polymer Science*, 112, 2559-2566, 2009.
- [54] C. Mobuchon, P. Carreau, M. Heuzey, M. Sepehr, G. Ausias, «Shear and extensional properties of short glass fiber reinforced polypropylene», *Polymer Composite*, 26, 247-264, 2005.
- [55] N. Le Moigne, M. Van Den Oever, T. Budtova, «A statistical analysis of fibre size and shape distribution after compounding in composites reinforced by natural fibres», *Composites Part A: Applied Science and Manufacturing*, 42 (10), 1542-1550, 2011.
- [56] A. Mohanty, S. Vivekanandhan, J. Pin, M. Misra, «Composites from renewable and sustainable resources: Challenges and innovations», *Science*, 362 (6414), 536-542, 2018.
- [57] R. Gunti, A. Ratna Prasad, A. Gupta, «Mechanical and degradation properties of natural fiber-reinforced PLA composites: Jute, sisal, and elephant grass», *Polymer Composites*, 39 (4), 1125-1136, 2018.

- [58] J. Li, J. Kim, «Percolation threshold of conducting polymer composites containing 3D randomly distributed graphite nanoplatelets», *Composites science and technology*, 67 (10), 2114-2120, 2007.
- [59] C. Martin, J. Sandler, M. Shaffer, M. Schwarz, W. Bauhofer, K. Schulte, A. Windle, «Formation of percolating networks in multi-wall carbon-nanotube–epoxy composites», *Composites science and technology*, 64 (15), 2309-2316, 2004.
- [60] A. Battisti, A. Skordos, I. Partridge, «Percolation threshold of carbon nanotubes filled unsaturated polyesters» *Composites Science and technology*, 70 (4), 633-637, 2010.
- [61] I. Bozyel, D. Gokcen, «Determining electrical percolation threshold of randomly distributed conductor materials in polymer composites via pathfinding algorithms» *Composites Science and Technology*, 109404, 2022.
- [62] C. Nan, Y. Shen, J. Ma, «Physical properties of composites near percolation», *Annual Review of Materials Research*, 40, 131-151, 2010.
- [63] D. Stauffer, A. Aharony, Introduction to percolation theory, London: Taylor and Franis, 1992.
- [64] Z. Tang, D. Wang, Y. Li, P. Huang, S. Fu, «Modeling the synergistic electrical percolation effect of carbon nanotube/graphene/polymer composites» *Composites Science and Technology*, 109496, 2022.
- [65] M. Foygel, R. Morris, D. Anez, S. French, V. Sobolev, «Theoretical and computational studies of carbon nanotube composites and suspensions: Electrical and thermal conductivity», *Physical Review B*, 71, (10), 104201, 2005.
- [66] M. Grujicic, G. Cao, W. Roy, «A computational analysis of the percolation threshold and the electrical conductivity of carbon nanotubes filled polymeric materials», *Journal of materials science*, 39 (14), 4441-4449, 2004.

- [67] I. Balberg, C. Anderson, S. Alexander, N. Wagner, «Excluded volume and its relation to the onset of percolation», *Physical review B*, 30 (7), 3933, 1984.
- [68] T. Natsuki, M. Endo, T. Takahashi, «Percolation study of orientated short-fiber composites by a continuum model», *Physica A: Statistical Mechanics and its Applications*, 352 (2-4), 498-508, 2005.
- [69] A. Celzard, E. McRae, C. Deleuze, M. Dufort, G. Furdin, J. Mareche, «Critical concentration in percolating systems containing a high-aspect-ratio filler», *Physical Review B*, 53 (10), 6209, 1996.
- [70] V. Irzhak, «Percolation Threshold in Polymer Nanocomposites», *Colloid Journal*, 83 (1), 64-69, 2021.
- [71] I. Ferero-Sandoval, F. Cervantes-Alvarez, J. Ramirez-Rincon, J. Macias, N. Pech-May, J. Ordonez-Miranda, J. Alvarado-Gil, «Percolation threshold of the thermal, electrical and optical properties of carbonyl-iron microcomposites», *Applied Composite Materials*, 28 (2), 447-463, 2021.
- [72] G. Filippone, M. Salzano de Luna, «A unifying approach for the linear viscoelasticity of polymer nanocomposites», *Macromolecules*, 45 (21), 8853-8860, 2012.
- [73] G. Filippone, M. Salzano de Luna, D. Acierno, P. Russo, «Elasticity and structure of weak graphite nanoplatelet (GNP) networks in polymer matrices through viscoelastic analyses», *Polymer*, 53 (13), 2699-2704, 2012.
- [74] G. Filippone, A. Causa, M. Salzano de Luna, L. Sanguigno, D. Acierno, «Assembly of plate-like nanoparticles in immiscible polymer blends—effect of the presence of a preferred liquid–liquid interface», *Soft Matter*, 10 (18), 3183-3191, 2014.
- [75] R. Altobelli, M. Salzano de Luna, G. Filippone, «Interfacial crowding of nanoplatelets in co-continuous polymer blends: Assembly, elasticity and structure of the interfacial nanoparticle network», *Soft Matter*, 13 (37), 6465-6473, 2017.

- [76] A. Fraga, E. Frulloni, O. De la Osa, J. Kenny, A. Vazquez, «Relationship between water absorption and dielectric behaviour of natural fibre composite materials», *Polymer testing*, 25 (2), 181-187, 2006.
- [77] E. Jayamani, S. Hamdan, M. Rahman, M. Bakri, «Comparative study of dielectric properties of hybrid natural fiber composites», *Procedia Engineering*, 97, 536-544, 2014.
- [78] W. Wang, M. Sain, P. Cooper, «Study of moisture absorption in natural fiber plastic composites», *Composites science and technology*, 66 (3-4), 379-386, 2006.
- [79] H. Scher, R. Zallen, «Critical density in percolation processes», *The Journal of Chemical Physics*, 53 (9), 3759-3761, 1970.
- [80] I. Balberg, «Recent developments in continuum percolation», *Philosophical Magazine B*, 56 (6), 991-1003, 1987.
- [81] I. Balberg, «Universal percolation-threshold limits in the continuum», *Physical review B*, 31(6), 4053, 1985.
- [82] A. Dani, A. Ogale, «Electrical percolation behavior of short-fiber composites: Experimental characterization and modeling», *Composites Science and Technology*, 56 (8), 911-920, 1996.
- [83] V. Mazzanti, M. Salzano de Luna, R. Pariante, F. Mollica, G. Filippone, «Natural fiber-induced degradation in PLA-hemp biocomposites in the molten state», *Composites Part A: Applied Science and Manufacturing*, 137, 105990, 2020.
- [84] M. Mours, H. Winter, «Time-resolved rheometry», *Rheologica Acta*, 33 (5), 385-397, 1994.
- [85] G. Filippone, S. Carroccio, R. Mendichi, L. Gioiella, N. Dintcheva, C. Gambarotti, «Time-resolved rheology as a tool to monitor the progress of polymer degradation in the melt state—Part I: Thermal and thermo-oxidative degradation of polyamide 11», *Polymer*, 72, 134-141, 2015.

- [86] G. Filippone, S. Carroccio, G. Curcuruto, E. Passaglia, C. Gambarotti, N. Dintcheva, «Time-resolved rheology as a tool to monitor the progress of polymer degradation in the melt state–Part II: Thermal and thermo-oxidative degradation of polyamide 11/organo-clay nanocomposites», *Polymer*, 73, 102-110, 2015.
- [87] W. Gleissle. B. Hochstein, «Validity of the Cox–Merz rule for concentrated suspensions», *Journal of rheology*, 47 (4), 897-910, 2003.
- [88] G. Filippone, G. Romeo, D. Acierno, «Viscoelasticity and structure of polystyrene/fumed silica nanocomposites: filler network and hydrodynamic contributions», *Langmuir*, 26 (4), 2714-2720, 2010.
- [89] D. Acierno, G. Filippone, G. Romeo, P. Russo, «Rheological aspects of PP-TiO<sub>2</sub> micro and nanocomposites: a preliminary investigation» in *In Macromolecular Symposia*, Weinheim: WILEY-VCH Verlag, 2007.
- [90] J. Jancar, J. Douglas, F. Starr, S. Kumar, P. Cassagnau, A. Lesser, S. Sternstein, M. Buehler, «Current issues in research on structure–property relationships in polymer nanocomposites», *Polymer*, 51, (15), 3321-3343, 2010.
- [91] R. Vijay, R. Jain, K. Sharma, «Dielectric spectroscopy of grape juice at microwave frequencies», *International Agrophysics*, 29 (2), 2015.
- [92] K. Deshmukh, S. Sankaran, B. Ahamed, K. Sadasivuni, K. Pasha, D. Ponnamma, P. Rama Sreekanth, K. Chidambaram, «Dielectric spectroscopy», *Spectroscopic methods for nanomaterials characterization*, 237-299, 2017.
- [93] Y. Li, M. Cordovez, V. Karbhari, «Dielectric and mechanical characterization of processing and moisture uptake effects in E-glass/epoxy composites», *Composites Part B: Engineering*, 34 (4), 383-390, 2003.
- [94] R. Pethrick, D. Hayward, «Real time dielectric relaxation studies of dynamic polymeric systems», *Progress in Polymer Science*, 27 (9), 1983-2017, 2002.

- [95] M. Deroiné, A. Le Duigou, Y. Corre, P. Le Gac, P. Devies, G. César, S. Bruzaud, «Accelerated ageing of polylactide in aqueous environments: Comparative study between distilled water and seawater», *Polymer degradation and stability*, 108, 319-329, 2014.
- [96] P. Neogi, *Diffusion in polymers*, New York: Marcel Dekker, 1996.
- [97] J. Balart, N. Montanes, V. Fombuena, T. Boronat, L. Sànchez-Nacher, «Disintegration in compost conditions and water uptake of green composites from poly (lactic acid) and hazelnut shell flour», *Journal of Polymers and the Environment*, 26 (2), 701-715, 2018.
- [98] O. Gil-Castel, J. Badia, T. Kittikorn, E. Stromberg, A. Martinez-Felipe, M. Ek, S. Karlsson, A. Ribes-Greus, «Hydrothermal ageing of polylactide/sisal biocomposites. Studies of water absorption behaviour and Physico-Chemical performance», *Polymer degradation and stability*, 108, 212-222, 2014.
- [99] S. Ramamoorthy, Q. Di, K. Adekunle, M. Skrifvars, «Effect of water absorption on mechanical properties of soybean oil thermosets reinforced with natural fibers», *Journal of Reinforced Plastics and Composites*, 31 (18), 1191-1200, 2012.
- [100] A. Le Duigou, A. Bourmaud, P. Davies, C. Baley, «Long term immersion in natural seawater of Flax/PLA biocomposite», *Ocean Engineering*, 90, 140-148, 2014.
- [101] M. Nilsoon, G. Frenning, J. Grasjo, G. Alderborn, M. Stromme, «Conductivity percolation in loosely compacted microcrystalline cellulose: An in situ study by dielectric spectroscopy during densification», *The Journal of Physical Chemistry B*, 110 (41), 20502-20506, 2006.
- [102] S. Barrau, P. Demont, A. Peigney, C. Laurent, C. Lacabanne, «DC and AC conductivity of carbon nanotubes– polyepoxy composites», *Macromolecules*, 36 (14), 5187-5194, 2003.
- [103] G. Psarras, E. Manolakaki, G. Tsangaris, «Dielectric dispersion and ac conductivity in—Iron particles loaded—polymer composites», *Composites Part A: Applied Science and Manufacturing*, 34 (12),

1187-1198, 2003.

- [104] A. Kota, B. Cipriano, M. Duesterberg, A. Gershon, D. Powell, S. Raghavan, H. Bruck, «Electrical and rheological percolation in polystyrene/MWCNT nanocomposites», *Macromolecules*, 40 (20), 7400-7406, 2007.
- [105] R. Chandra, R. Rustgi, «Biodegradable polymers», *Progress in Polymer Science*, 23 (7), 1273-1335, 1998.
- [106] F. Vilaplana, E. Stromberg, S. Karlsson, «Environmental and resource aspects of sustainable biocomposites», *Polymer Degradation and Stability*, 95 (11), 2147-2161, 2010.
- [107] L. Lim, R. Auras, M. Rubino, «Processing technologies for poly (lactic acid)», *Progress in Polymer Science*, 33 (8), 820-852, 2008.
- [108] G. Gorrasi, R. Anastasio, L. Bassi, R. Pantani, «Barrier properties of PLA to water vapour: Effect of temperature and morphology», *Macromolecular Research*, 21 (10), 1110-1117, 2013.
- [109] S. Pilla, S. Gong, E. O'Neill, L. Yang, R. Rowell, «Polylactide-recycled wood fiber composites», *Journal of Applied Polymer Science*, 111 (1), 37-47, 2009.
- [110] J. Badia, E. Stromberg, S. Karlsson, A. Ribes-Greus, «The role of crystalline, mobile amorphous and rigid amorphous fractions in the performance of recycled poly (ethylene terephthalate)(PET)», *Polymer Degradation and Stability*, 97 (1), 98-10, 2012.
- [111] E. Fukada, «Piezoelectricity of biopolymers», *Biorheology*, 32 (6), 593-609, 1995.
- [112] E. Munch, J. Pelletier, B. Sixou, G. Vigier, «Characterization of the drastic increase in molecular mobility of a deformed amorphous polymer», *Physical Review Letters*, 97, 1-4, 2006.
- [113] L. Santonja-Blasco, R. Moriana, J. Badia, A. Ribes-Greus, «Thermal analysis applied to the characterization of degradation in soil of polylactide: I. Calorimetric and viscoelastic analyses», *Polymer*

*Degradation and Stability*, 95 (11), 2185-2121, 2010.

- [114] J. Menczel, R. Prime, P. Gallagher, «Differential scanning calorimetry», in *Thermal analysis of polymers: Fundamentals and applications*, USA, John Wiley: NJ, 2009, 241-317.
- [115] J. Mofokeng, A. Luyt, T. Tabi, J. Kovacs, «Comparison of injection moulded, natural fibre-reinforced composites with PP and PLA as matrices», *Journal of Thermoplastic Composite Materials*, 25 (8), 927-948, 2012.
- [116] V. Speranza, A. De Meo, R. Pantani, «Thermal and hydrolytic degradation kinetics of PLA in the molten state», *Polymer Degradation and Stability*, 100, 37-41, 2014.
- [117] H. Xu, C. Liu, C. Chen, B. Hsiao, G. Zhong, Z. Li, «Easy alignment and effective nucleation activity of ramie fibers in injection-molded poly (lactic acid) biocomposites», *Biopolymers*, 97 (10), 825-839, 2012.
- [118] Y. Wang, B. Tong, S. Hou, M. Li, C. Shen, «Transcrystallization behavior at the poly (lactic acid)/sisal fibre biocomposite interface», *Composites Part A: Applied Science and Manufacturing*, 42 (1), 66-74, 2011.
- [119] N. Zafeiropoulos, C. Baillie, F. Matthews, «A study of transcrystallinity and its effect on the interface in flax fibre reinforced composite materials», *Composites Part A: Applied Science and Manufacturing*, 32 (3-4), 525-543, 2001.
- [120] M. Cristea, D. Ionita, M. Iftime, «Dynamic mechanical analysis investigations of PLA-based renewable materials: How are they useful?», *Materials*, 13 (22), 5302, 2020.
- [121] W. Ferreira, C. Andrade, «The role of graphene on thermally induced shape memory properties of poly (lactic acid) extruded composites», *Journal of Thermal Analysis and Calorimetry*, 143 (4), 3107-3115, 2021.
- [122] R. Ashok, C. Srinivasa, B. Basavaraju, «Dynamic mechanical

- properties of natural fiber composites—a review», *Advanced Composites and Hybrid Materials*, 2 (4), 586-607, 2019.
- [123] F. Espinach, S. Boufi, M. Delgado-Aguilar, F. Julian, P. Mutje, J. Mendez, «Composites from poly (lactic acid) and bleached chemical fibres: Thermal properties», *Composites Part B: Engineering*, 134, 169-176, 2018.
- [124] F. Yu, T. Liu, X. Zhao, X. Yu, A. Lu, J. Wang, «Effects of talc on the mechanical and thermal properties of polylactide», *Journal of Applied Polymer Science*, 125 (S2), 99-109, 2012.
- [125] J. Badia, E. Stromberg, S. Karlsson, A. Ribes-Greus, «Material valorisation of amorphous polylactide. Influence of thermo-mechanical degradation on the morphology, segmental dynamics, thermal and mechanical performance», *Polymer Degradation and Stability*, 97 (4), 670-678, 2012.
- [126] P. Daly, D. Bruce, D. Melik, G. Harrison, «Thermal degradation kinetics of poly (3-hydroxybutyrate-co-3-hydroxyhexanoate)», *Journal of Applied Polymer Science*, 98 (1), 66-74, 2005.
- [127] K. Seo, J. Cloyd, «Kinetics of hydrolysis and thermal degradation of polyester melts», *Journal of Applied Polymer Science*, 42 (3), 845-850, 1991.
- [128] M. Partini, O. Argenio, I. Coccorullo, R. Pantani, «Degradation kinetics and rheology of biodegradable polymers», *Journal of Thermal Analysis and Calorimetry*, 98 (3), 645-653, 2009.
- [129] H. Barnes, «A review of the rheology of filled viscoelastic systems», *Rheology reviews*, 1-36, 2003.
- [130] N. Morin-Crini, S. Loiacono, S. Placet, G. Torri, C. Bredu, M. Kostic, C. Cosentino, G. Chanet, B. Martel, E. Lichtfouse, G. Crini, «Hemp-based adsorbents for sequestration of metals: a review», *Environmental Chemistry Letters*, 17 (1), 393-408, 2019.
- [131] O. Wachsen, K. Reichert, R. Kruger, H. Much, G. Schulz, «Thermal decomposition of biodegradable polyesters—III. Studies on the mechanisms of thermal degradation of oligo-l-lactide using SEC,

- LACCC and MALDI-TOF-MS», *Polymer Degradation and Stability*, 55 (2), 225-231, 1997.
- [132] R. Al-Itry, K. Lamnawar, A. Maazouz, «Improvement of thermal stability, rheological and mechanical properties of PLA, PBAT and their blends by reactive extrusion with functionalized epoxy», *Polymer Degradation and Stability*, 97 (10), 1898-1914, 2012.
- [133] A. Vieira, A. Marques, R. Guedes, V. Tita, «4D numerical analysis of scaffolds: a new approach», in *Computational Methods in Applied Sciences*, Dordrecht, Springer, 2014, 69-95.
- [134] J. Pickett, D. Coyle, «Hydrolysis kinetics of condensation polymers under humidity aging conditions», *Polymer Degradation and Stability*, 98 (7), 1311-1320, 2013.
- [135] A. Vieira, J. Vieira, J. Ferra, F. Magalhaes, R. Guedes, A. Marques, «Mechanical study of PLA–PCL fibers during in vitro degradation», *Journal of the Mechanical Behavior of Biomedical Materials*, 4 (3), 451-460, 2011.
- [136] A. Gleadall, J. Pan, M. Kruff, M. Kellomaki, «Degradation mechanisms of bioresorbable polyesters. Part 1. Effects of random scission, end scission and autocatalysis», *Acta biomaterialia*, 10 (5), 2223-2232, 2014.
- [137] M. Reddy, S. Vivekanandhan, M. Misra, S. Bhatia, A. Mohanty, «Biobased plastics and bionanocomposites: Current status and future opportunities», *Progress in Polymer Science*, 38 (10-11), 1653-1689, 2013.
- [138] I. Vroman, L. Tighzert, «Biodegradable polymers», *Materials*, 2 (2), 307-334, 2009.
- [139] X. Zong, Z. Wang, B. Hsiao, B. Chu, J. Zhou, D. Jamiolkowski, et al., «Structure and morphology changes in absorbable poly(glycolide) and poly(glycolide-co-lactide) during in vitro degradation», *Macromolecules*, 32, 8107-8114, 1999.
- [140] D. Arifin, L. Lee, C. Wang, «Mathematical modeling and simulation

of drug release from microspheres: Implications to drug delivery systems», *Advanced Drug Delivery Reviews*, 58 (12-13), 1274-1325, 2006.

- [141] S. Lyu, R. Sparer, D. Untereker, «Analytical solutions to mathematical models of the surface and bulk erosion of solid polymers», *Journal of Polymer Science Part B: Polymer Physics*, 43 (4), 383-397, 2005.
- [142] I. Grizzi, H. Garreau, S. Li, M. Vert, «Hydrolytic degradation of devices based on poly (DL-lactic acid) size-dependence», *Biomaterials*, 16 (4), 305-311, 1995.
- [143] Y. Mohammadi, E. Jabbari, «Monte carlo simulation of degradation of porous Poly (lactide) scaffolds, 1: effect of porosity on pH», *Macromolecular Theory and Simulations*, 15 (9), 643-653, 2006.
- [144] C. Lam, M. Savalani, S. Teoh, D. Hutmacher, «Dynamics of in vitro polymer degradation of polycaprolactone-based scaffolds: accelerated versus simulated physiological conditions», *Biomedical Materials*, 3 (3), 034108, 2008.
- [145] X. Zhang, M. Espiritu, A. Bilyk, L. Kurniawan, «Morphological behaviour of poly (lactic acid) during hydrolytic degradation», *Polymer Degradation and Stability*, 93 (10), 1964-1970, 2008.
- [146] R. Pantani, A. Sorrentino, «Influence of crystallinity on the biodegradation rate of injection-moulded poly (lactic acid) samples in controlled composting conditions», *Polymer Degradation and Stability*, 98 (5), 1089-1096, 2013.
- [147] E. Fischer, H. Sterzel, G. Wegner, «Investigation of the structure of solution grown crystals of lactide copolymers by means of chemical reactions», *Kolloid-Zeitschrift und Zeitschrift für Polymere*, 251 (11), 980-990, 1973.
- [148] M. Deroiné, A. Le Doigou, Y. Corre, P. Le Gac, P. Davies, G. Cesar, S. Bruzard, «Seawater accelerated ageing of poly (3-hydroxybutyrate-co-3-hydroxyvalerate)», *Polymer Degradation and Stability*, 105, 237-247, 2014.

- [149] I. Kyrikou, D. Briassoulis, «Biodegradation of agricultural plastic films: a critical review», *Journal of Polymers and the Environment*, 15 (2), 125-150, 2007.
- [150] K. Fukushima, D. Tabuani, M. Dottori, I. Armentano, J. Kenny, G. Camino, «Effect of temperature and nanoparticle type on hydrolytic degradation of poly (lactic acid) nanocomposites», *Polymer Degradation and Stability*, 96 (2), 2120-2129, 2011.
- [151] M. Paul, C. Delcourt, M. Alezandre, P. Degée, F. Monteverde, P. Dubois, «Polylactide/montmorillonite nanocomposites: study of the hydrolytic degradation», *Polymer Degradation and Stability*, 87 (3), 535-542, 2005.
- [152] M. Sedničková, S. Pekařová, P. Kucharczyk, J. Bočkaj, I. Janigová, A. Kleinová, D. Johec-Mošková, L. Omaníková, D. Perďochová, M. Koutný, V. Sedlařík, P. Alexy, I. Chodák, «Changes of physical properties of PLA-based blends during early stage of biodegradation in compost», *International Journal of Biological Macromolecules*, 113, 434-442, 2018.
- [153] S. Pilla, S. Gong, E. O'Neill, R. Rowell, A. Krzysik, «Polylactide-pine wood flour composites», *Polymer Engineering & Science*, 48 (3), 578-587, 2008.
- [154] A. Mathew, K. Oksman, M. Sain, «The effect of morphology and chemical characteristics of cellulose reinforcements on the crystallinity of polylactic acid», *Journal of Applied Polymer Science*, 101 (1), 300-310, 2006.
- [155] J. Balart, V. Fombuena, O. Fenollar, T. Boronat, L. Sánchez-Nacher, «Processing and characterization of high environmental efficiency composites based on PLA and hazelnut shell flour (HSF) with biobased plasticizers derived from epoxidized linseed oil (ELO)», *Composites Part B: Engineering*, 86, 168-177, 2016.
- [156] P. Stloukal, S. Pekarova, A. Kalendova, H. Mattausch, S. Laske, C. Holzer, L. Chitu, S. Bodner, G. Maier, M. Slouf, M. Koutnya, «Kinetics and mechanism of the biodegradation of PLA/clay nanocomposites during thermophilic phase of composting process»,

*Waste management*, 42, 31-40, 2015.

- [157] G. Siparsky, K. Voorhees, F. Miao, «Hydrolysis of polylactic acid (PLA) and polycaprolactone (PCL) in aqueous acetonitrile solutions: autocatalysis», *Journal of Environmental Polymer Degradation*, 6 (1), 31-41, 1998.
- [158] J. Kolstad, E. Vink, B. De Wilde, L. Debeer, «Assessment of anaerobic degradation of Ingeo™ polylactides under accelerated landfill conditions», *Polymer Degradation and Stability*, 97 (7), 1131-1141, 2012.
- [159] A. Tukker, «Life cycle assessment as a tool in environmental impact assessment», *Environmental Impact Assessment Review*, 20 (4), 435-456, 2000.
- [160] G. Rebitzer, T. Ekvall, R. Frischknecht, D. Hunkeler, G. Norris, T. Rydberg, W. Schmidt, S. Suh, B. Weidema, D. Pennington, «Life cycle assessment: Part 1: Framework, goal and scope definition, inventory analysis, and applications», *Environment International*, 30 (5), 701-720, 2004.
- [161] M. Curran, «Life cycle assessment», *Kirk-Othmer Encyclopedia of Chemical Technology*, 1-28, 2000.
- [162] M. Mansor, M. Mastura, S. Sapuan, A. Zainudin, «The environmental impact of natural fiber composites through life cycle assessment analysis», in *In Durability and life prediction in biocomposites, fibre-reinforced composites and hybrid composites*, Woodhead Publishing, 2019, 257-285.
- [163] M. Mansor, M. Salit, E. Zainudin, N. Aziz, H. Ariff, «Life cycle assessment of natural fiber polymer composites», in *In Agricultural biomass based potential materials*, Springer, Cham., 2015, 121-141.
- [164] M. Ramesh, C. Deepa, L. Kumar, M. Sanjay, S. Seingchin, «Life-cycle and environmental impact assessments on processing of plant fibres and its bio-composites: A critical review», in *Journal of Industrial Textiles*, 2020.

- [165] D. Pennington, J. Potting, G. Finnveden, E. Lindeijer, O. Jolliet, T. Rydberg, G. Rebitzer, «Life cycle assessment Part 2: Current impact assessment practice», in *Environment International*, 30 (5), 2004, 721-739.
- [166] A. Mohanty, S. Vivekanandhan, J. Pin, M. Misra, «Composites from renewable and sustainable resources: Challenges and innovations. Science» *Science*, 362 (6414), 536-542, 2018.
- [167] R. Ilyas, S. Sapuan, «Biopolymers and biocomposites: chemistry and technology», *Current Analytical Chemistry*, 16 (5), 500-503, 2020.
- [168] J. Correa, J. Montalvo-Navarrete, M. Hidalgo-Salazar, «Carbon footprint considerations for biocomposite materials for sustainable products: A review», *Journal of Cleaner Production*, 208, 785-794, 2019.
- [169] A. Bourmaud, D. Akesson, J. Beaugrand, A. Le Duigou, M. Skrifvars, C. Baley, «Recycling of L-Poly-(lactide)-Poly-(butylene-succinate)-flax biocomposite», *Polymer Degradation and Stability*, 128, 77-88, 2016.
- [170] A. Ead, R. Appel, N. Alex, C. Ayranci, J. Carey, «Life cycle analysis for green composites: A review of literature including considerations for local and global agricultural use», *Journal of Engineered Fibers and Fabrics*, 16, 1-20, 2021.
- [171] M. Yates, C. Barlow, «Life cycle assessments of biodegradable, commercial biopolymers—A critical review», *Resources, Conservation and Recycling*, 78, 54-66, 2013.
- [172] A. La Rosa, G. Cozzo, A. Latteri, A. Recca, A. Bjorklund, E. Parrinello, G. Cicala, «Life cycle assessment of a novel hybrid glass-hemp/thermoset composite», *Journal of Cleaner Production*, 44, 69-76, 2013.
- [173] A. Nair, P. Sivasubramanian, P. Balakrishnan, K. Ajith Kumar e M. Sreekala, «Environmental effects, biodegradation, and life cycle analysis of fully biodegradable “green” composites» *Polymer Composites*, 515-568, 2013.

- [174] F. Brentrup, J. Kusters, J. Lammel, P. Barraclough, H. Kuhlmann, «Environmental impact assessment of agricultural production systems using the life cycle assessment (LCA) methodology II. The application to N fertilizer use in winter wheat production systems», *European Journal of Agronomy*, 20 (3), 265-279, 2004.
- [175] L. Zampori, G. Dotelli, V. Vernelli, «Life cycle assessment of hemp cultivation and use of hemp-based thermal insulator materials in buildings», *Environmental Science & Technology*, 47 (13), 7413-7420, 2013.
- [176] M. Yates, C. Barlow, «Life cycle assessments of biodegradable, commercial biopolymers—A critical review», *Resources, Conservation and Recycling*, 78, 54-66, 2013.
- [177] R. Shogren, D. Wood, W. Orts, G. Glenn, «Plant-based materials and transitioning to a circular economy», *Sustainable Production and Consumption*, 19, 194-215, 2019.
- [178] S. Joshi, L. Dzal, A. Mohanty, S. Arora, «Are natural fiber composites environmentally superior to glass fiber reinforced composites?», *Composites Part A: Applied Science and Manufacturing*, 35 (3), 371-376, 2004.
- [179] M. Todor, C. Bulei, I. Kiss, V. Alexa, «Recycling of textile wastes into textile composites based on natural fibres: the valorisation potential», *In IOP Conference Series: Materials Science and Engineering*, 477 (1), 012004, 2019.
- [180] «Universiteit Leiden – CML-IA Characterisation Factors,» 2016. [Online]. Available: <https://www.universiteitleiden.nl/en/research/research-output/science/cml-ia-characterisation-factors>. [1 February 2022].
- [181] R. Arvidsson, M. Svanstrom, «A framework for energy use indicators and their reporting in life cycle assessment», *Integrated Environmental Assessment and Management*, 12 (3), 429-436, 2016.
- [182] J. Vogtlander, N. Va der Velden, P. Van der Lugt, «Carbon sequestration in LCA, a proposal for a new approach based on the global carbon cycle; cases on wood and on bamboo», *International*

*Journal of Life Cycle Assessment*, 19 (1), 13-23, 2014.

- [183] S. Lueddeckens, P. Saling, E. Guenther, «Temporal issues in life cycle assessment—a systematic review», *International Journal of Life Cycle Assessment*, 25, 1385-1401, 2020.
- [184] B. Hermann, L. Debeer, B. De Wilde, K. Blok, M. Patel, «To compost or not to compost: Carbon and energy footprints of biodegradable materials' waste treatment», *Polymer Degradation and Stability*, 96 (6), 1159-1171, 2011.
- [185] G. Wernet, C. Bauer, B. Steubing, J. Reinhard, E. Moreno-Ruiz, B. Weidema, «The ecoinvent database version 3 (part I): overview and methodology», *International Journal of Life Cycle Assessment*, 21 (9), 1218-1230, 2016.
- [186] F. Ardente, M. Beccali, M. Cellura, M. Mistretta, «Building energy performance: a LCA case study of kenaf-fibres insulation board», *Energy and Buildings*, 40 (1), 1-10, 2008.
- [187] «Kenaf Eco Fibers Italia - Comparative table between some characteristics of hemp and kenaf,» [Online]. Available: <https://www.kenaf-fiber.com/en/infotec-tabella1.html>. [22 February 2022].
- [188] G. Berhongaray, O. El Kasmioui, R. Ceulemans, «Comparative analysis of harvesting machines on an operational high-density short rotation woody crop (SRWC) culture: one-process versus two-process harvest operation», *Biomass Bioenergy*, 58, 333-342, 2013.
- [189] E. Vink, S. Davies, «Life cycle inventory and impact assessment data for 2014 Ingeo™ polylactide production», *Industrial Biotechnology*, 11 (3), 167-180, 2015.
- [190] «NatureWorks LLC – Ingeo Partners,» [Online]. Available: <https://www.natureworkslc.com/Where-to-Buy/Partners>. [19 January 2022].
- [191] «Resinex – Distribution of plastics & elastomers» [Online]. Available: <https://www.resinex.it/en/contacts.html> [15 January 2022].

- [192] «U.S. Department of Transportation, Federal Railroad Administration – Freight Rail Overview» [Online]. Available: <https://railroads.dot.gov/rail-network-development/freight-rail-overview>. [19 January 2022].
- [193] «European Union Agency for Railways – Rail Freight in the European Union» [Online]. Available: [https://www.era.europa.eu/sites/default/files/library/docs/le-aflets/rail\\_freight\\_in\\_the\\_european\\_union\\_en.pdf](https://www.era.europa.eu/sites/default/files/library/docs/le-aflets/rail_freight_in_the_european_union_en.pdf). [15 January 2022].
- [194] G. Rejeshkumar, S. Seshadri, G. Devnani, M. Sanjay, S. Siengchin, J. Maran. A. Anuf, «Environment friendly, renewable and sustainable poly lactic acid (PLA) based natural fiber reinforced composites—A comprehensive review», *Journal of Cleaner Production*, 127483, 2021.
- [195] P. Pawelzik, M. Carus, J. Hotchkiss, R. Narayan, S. Selke, M. Wellisch, M. Patel, «Critical aspects in the life cycle assessment (LCA) of bio-based materials—Reviewing methodologies and deriving recommendations», *Resources, Conservation and Recycling*, 73, 211-228, 2013.
- [196] N. Noh, T. Yoon, R. Kim, N. Bolton, C. Kim, Y. Son, «Carbon and nitrogen accumulation and decomposition from coarse woody debris in a naturally regenerated Korean red pine (*Pinus densiflora* S. et Z.) forest», *Forests*, 8 (6), 214, 2017.
- [197] P. Ritson, S. Sochacki, «Measurement and prediction of biomass and carbon content of *Pinus pinaster* trees in farm forestry plantations, south-western Australia», *Forest Ecology and Management*, 175 (1-3), 103-117, 2003.
- [198] K. Kamarundin, N. Zaini, N. Khairuddin, «CO<sub>2</sub> removal using amine-functionalized kenaf in pressure swing adsorption system», *Journal of Environmental Chemical Engineering*, 6 (1), 549-559, 2018.
- [199] A. Viretto, N. Gontard, H. Angellier-Coussy, «Urban parks and gardens green waste: A valuable resource for the production of fillers for biocomposites applications», *Waste Management*, 120, 538-548,

2021.

- [200] G. David, G. Croxatto Vega, J. Sohn, A. Nilsson, A. Helias, N. Gontard, H. Angellier-Coussy, «Using life cycle assessment to quantify the environmental benefit of upcycling vine shoots as fillers in biocomposite packaging materials», *The International Journal of Life Cycle Assessment*, 26 (4), 738-752, 2021.
- [201] E. Sanchez-Safont, A. Aldureid, J. Lagaron, J. Gamez-Perez, L. Cabedo, «Biocomposites of different lignocellulosic wastes for sustainable food packaging applications», *Composites Part B: Engineering*, 145, 215-225, 2018.
- [202] G. Koronis, A. Silva, M. Fontul, «Green composites: A review of adequate materials for automotive applications», *Composites Part B: Engineering*, 44 (1), 120-127, 2013.
- [203] A. Santoni, P. Bonfiglio, F. Mollica, P. Fausti, F. Pompoli, V. Mazzanti, «Vibro-acoustic optimisation of Wood Plastic Composite systems», *Construction and Building Materials*, 174, 730-740, 2018.
- [204] S. Shi, L. Cai, Y. Weng, D. Wang, Y. Sun, «Comparative life-cycle assessment of water supply pipes made from bamboo vs. polyvinyl chloride», *Journal of Cleaner Production*, 240, 118172, 2019.
- [205] V. Mazzanti, R. Pariante, A. Bonanno, O. De Ballesteros, F. Mollica, G. Filippone, «Reinforcing mechanisms of natural fibers in green composites: Role of fibers morphology in a PLA/hemp model system», *Composites Science and Technology*, 180, 51-59, 2019.
- [206] S. Carroccio, P. Scarfato, E. Bruno, P. Aprea, N. Dintcheva, G. Filippone, «Impact of nanoparticles on the environmental sustainability of polymer nanocomposites based on bioplastics or recycled plastics—A review of life-cycle assessment studies», *Journal of Cleaner Production*, 130322, 2021.
- [207] M. Ashby, «Multi-objective optimization in material design and selection», *Acta Materialia*, 48 (1), 359-369, 2000.
- [208] N. LLC, «Technical Data Sheet Ingeo Biopolymer 2003D, 4032D

and 4060D, Minnetonka Blvd., Minnetonka, MN 55345», 2019.

- [209] H. Wan, H. Ohtaki, S. Kotosaka, G. Hu, «A study of negative Poisson's ratios in auxetic honeycombs based on a large deflection model», *European Journal of Mechanics-A/Solids*, 23 (1), 95-106, 2004.
- [210] K. Evans, A. Alderson, «Auxetic materials: functional materials and structures from lateral thinking!», *Advanced materials*, 12 (9), 617-628, 2000.
- [211] K. Evans, K. Alderson, «Auxetic materials: the positive side of being negative», *Engineering Science & Education Journal*, 9 (4), 148-154, 2000.
- [212] L. Yanping, H. Hong, «A review on auxetic structures and polymeric materials», *Scientific Research and Essays*, 5 (10), 1052-1063, 2010.
- [213] B. Lempriere, «Poisson's ratio in orthotropic materials», *Aiaa Journal*, 6 (11), 2226-2227, 1968.
- [214] K. Wojciechowski, «Remarks on "Poisson ratio beyond the limits of the elasticity theory"», *Journal of the Physical Society of Japan*, 72 (7), 1819-1820, 2003.
- [215] M. Taylor, L. Francesconi, M. Gerendas, A. Shanian, C. Carson, K. Bertoldi, «Low porosity metallic periodic structures with negative Poisson's ratio», *Advanced Materials*, 26 (15), 2365-2370, 2014.
- [216] R. Baughman, J. Shacklette, A. Zakhidov, S. Stafstrom, «Negative Poisson's ratios as a common feature of cubic metals», *Nature*, 392 (6674), 362-365, 1998.
- [217] A. Greer, R. Lakes, T. Rouxel, «Poisson's ratio and modern materials», *Nature materials*, 10 (11), 823-837, 2011.
- [218] K. Saxena, R. Das, E. Calius, «Three decades of auxetics research—materials with negative Poisson's ratio: a review», *Advanced Engineering Materials*, 18 (11), 1847-1870, 2016.

- [219] X. Ren, R. Das, P. Tran, T. Ngo, Y. Xie, «Auxetic metamaterials and structures: a review» *Smart Materials and Structures*, 27 (2), 023001, 2018.
- [220] J. Grima, A. Alderson, K. Evans, «Auxetic behaviour from rotating rigid units», *Physica Status Solidi (B)*, 242 (3), 561-575, 2005.
- [221] J. Grima, P. Farrugia, R. Gatt, D. Attard, «On the auxetic properties of rotating rhombi and parallelograms: A preliminary investigation», *Physica Status Solidi (B)*, 245 (3), 521-529, 2008.
- [222] W. Wu, W. Hu, G. Qian, H. Liao, X. Xu, F. Berto, «Mechanical design and multifunctional applications of chiral mechanical metamaterials: A review», *Materials & Design*, 180, 107950, 2019.
- [223] A. Alderson, K. Alderson, D. Attard, K. Evans, R. Gatt, J. Grima, W. Miller, N. Ravirala, C. Smith, K. Zied, «Elastic constants of 3-, 4-and 6-connected chiral and anti-chiral honeycombs subject to uniaxial in-plane loading», *Composites Science and Technology*, 70 (7), 1042-1048, 2010.
- [224] D. Mousanezhad, B. Haghpanah, R. Ghosh, A. Hanouda, H. Nayeb-Hashemi, A. Vaziri, «Elastic properties of chiral, anti-chiral, and hierarchical honeycombs: A simple energy-based approach», *Theoretical and Applied Mechanics Letters*, 6 (2), 81-96, 2016.
- [225] J. Grima, R. Gatt, A. Alderson, K. Evans, «On the potential of connected stars as auxetic systems», *Molecular Simulation*, 31 (13), 925-935, 2005.
- [226] J. Huang, Q. Zhang, F. Scarpa, Y. Liu, J. Leng, «In-plane elasticity of a novel auxetic honeycomb design», *Composites Part B: Engineering*, 110, 72-82, 2017.
- [227] I. Gibson, M. Ashby, «The mechanics of three-dimensional cellular materials», *Proceedings of the royal society of London. A. Mathematical and physical sciences*, 382 (1782), 43-59, 1982.
- [228] J. Grima, K. Evans, «Auxetic behavior from rotating squares», *Journal of Materials Science Letters*, 19, 1563-1565, 2000.

- [229] J. Grima, V. Zammit, R. Gatt, A. Alderson, K. Evans, «Auxetic behaviour from rotating semi-rigid units», *Physica Status Solidi (B)*, 244 (3), 866-882, 2007.
- [230] W. Kelvin, *The molecular tactics of a crystal*, Clarendon Press, 1894.
- [231] L. Hu, Z. Lou, Z. Zhang, M. Liam, L. Huang, «Mechanical property of re-entrant anti-trichiral honeycombs under large deformation», *Composites Part B: Engineering*, 163, 107-120, 2019.
- [232] V. Carneiro, J. Meireles, H. Puga, «Auxetic materials—A review», *Materials Science-Poland*, 31 (4), 561-571, 2013.
- [233] Z. Wang, C. Luan, G. Liao, J. Liu, X. Yao, J. Fu, «Progress in auxetic mechanical metamaterials: structures, characteristics, manufacturing methods, and applications», *Advanced Engineering Materials*, 22 (10), 2000312, 2020.
- [234] I. Durgun, «Durgun, I. (2015). Sheet metal forming using FDM rapid prototype tool», *Rapid Prototyping Journal*, 21 (4), 412-422, 2015.
- [235] M. Meier, K. Tan, M. Lim, L. Chung, «Unlocking innovation in the sport industry through additive manufacturing», *Business Process Management Journal*, 25 (3), 456-475, 2018.
- [236] R. Garcia-Garcia, M. Gonzalez-Palacios, «Method for the geometric modeling and rapid prototyping of involute bevel gears», *The International Journal of Advanced Manufacturing Technology*, 98 (1), 645-656, 2018.
- [237] W. Yang, Z. Li, W. Shi, B. Xie, M. Yang, «Review on auxetic materials», *Journal of Materials Science*, 39 (10), 3269-3279, 2004.
- [238] M. Mir, M. Ali, J. Sami, U. Ansari, «Review of mechanics and applications of auxetic structures», *Advances in Materials Science and Engineering*, 2014, 1-17, 2014.
- [239] J. Goodier, «Theory of Elasticity, 3rd ed.», New York, USA, McGraw-Hill, 1970, 567.

- [240] Q. Liu, «Literature review: materials with negative Poisson's ratios and potential applications to aerospace and defence», 2006.
- [241] J. Choi, R. Lakes, «Non-linear properties of polymer cellular materials with a negative Poisson's ratio», *Journal of Materials Science*, 27 (17), 4678-4684, 1992.
- [242] Y. Wang, R. Lakes, «Analytical parametric analysis of the contact problem of human buttocks and negative Poisson's ratio foam cushions», *International Journal of Solids and Structures*, 39 (18), 4825-4838, 2002.
- [243] I. Gibson, D. Rosen, B. Stucker, M. Khorasani, D. Rosen, B. Stucker, M. Khorasani, Additive manufacturing technologies (Vol. 17), Cham, Switzerland: Springer, 2021.
- [244] D. Bourell, J. Kruth, M. Leu, G. Levy, D. Rosen, A. Beese, A. Clare, «Materials for additive manufacturing», *CIRP annals*, 66 (2), 659-681, 2017.
- [245] M. Attaran, «The rise of 3-D printing: The advantages of additive manufacturing over traditional manufacturing», *Business Horizons*, 60 (5), 677-688, 2017.
- [246] T. Rahim, A. Abdullah, H. Md Akil, «Recent developments in fused deposition modeling-based 3D printing of polymers and their composites», *Polymer Reviews*, 59 (4), 589-624, 2019.
- [247] S. Kalita, S. Bose, H. Hosick, A. Bandyopadhyay, «Development of controlled porosity polymer-ceramic composite scaffolds via fused deposition modeling», *Materials Science and Engineering*, 23 (5), 611-620, 2003.
- [248] O. Mohamed, S. Masood, J. Bhowmik, «Optimization of fused deposition modeling process parameters: a review of current research and future prospects», *Advances in Manufacturing*, 3 (1), 42-53, 2015.
- [249] A. Joseph, V. Mahesh, D. Harursampath, «On the application of additive manufacturing methods for auxetic structures: A review»,

*Advances in Manufacturing*, 9 (3), 342-368, 2021.

- [250] T. Li, Y. Chen, X. Hu, Y. Li, L. Wang, «Exploiting negative Poisson's ratio to design 3D-printed composites with enhanced mechanical properties», *Materials & Design*, 142, 247-258, 2018.
- [251] J. Grima, K. Evans, «Auxetic behavior from rotating triangles», *Journal of Materials Science*, 41 (10), 3193-3196, 2006.
- [252] D. Attard, J. Grima, «A three-dimensional rotating rigid units network exhibiting negative Poisson's ratios», *Physica Status Solidi (B)*, 249 (7), 1330-1338, 2012.
- [253] J. Grima, R. Gatt, «Perforated sheets exhibiting negative Poisson's ratios», *Advanced Engineering Materials*, 12 (6), 460-464, 2010.
- [254] L. Mizzi, D. Attard, K. Evans, R. Gatt, J. Grima, «Auxetic mechanical metamaterials with diamond and elliptically shaped perforations», *Acta Mechanica*, 232 (2), 779-791, 2021.
- [255] J. Grima, A. Alderson, K. Evans, «Auxetic behaviour from rotating rigid units», *Physica Status Solidi (B)*, 242 (3), 561-575, 2005.
- [256] L. Mizzi, D. Attard, R. Gatt, K. Dudek, B. Ellul, J. Grima, «Implementation of periodic boundary conditions for loading of mechanical metamaterials and other complex geometric microstructures using finite element analysis», *Engineering with Computers*, 37 (3), 1765-1779, 2021.
- [257] L. Mizzi, J. Grima, R. Gatt, D. Attard, «Analysis of the deformation behavior and mechanical properties of slit-perforated auxetic metamaterials», *Physica Status Solidi (b)*, 256 (1), 1800153, 2019.
- [258] C. Smith, R. Wootton, K. Evans, «Interpretation of experimental data for Poisson's ratio of highly nonlinear materials», *Experimental Mechanics*, 39 (4), 356-362, 1999.
- [259] J. Grima, S. Winczewski, L. Mizzi, M. Grech, R. Cauchi, R. Gatt, D. Attard, K. Wojciechowski, J. Rybicki, «Tailoring graphene to achieve negative Poisson's ratio properties», *Advanced Materials*, 27 (8),

1455-1459, 2015.

- [260] E. Castro-Aguirre, F. Iniguez-Franco, H. Samsudin, X. Fang, R. Auras, «Poly (lactic acid)—Mass production, processing, industrial applications, and end of life», *Advanced Drug Delivery Reviews*, 107, 333-366, 2016.
- [261] J. Grima, A. Alderson, K. Evans, «Auxetic behaviour from rotating rigid units», *Physica Status Solidi (B)*, 242 (3), 561-575, 2005.